# Warm Dense Matter
and
# Thomson Scattering
at
# FLASH

Dissertation

zur Erlangung des Doktorgrades
des Fachbereichs Physik
der Universität Hamburg

vorgelegt von

Roland Rainer Fäustlin

aus Augsburg

Hamburg
2010

| | |
|---|---|
| Gutachter der Dissertation | Prof. Dr. Wilfried Wurth<br>Prof. Dr. Henry Chapman |
| Gutachter der Disputation | Prof. Dr. Wilfried Wurth<br>Dr. Thomas Tschentscher |
| Datum der Disputation | 7. April 2010 |
| Vorsitzender des Prüfungsausschusses | Dr. Klaus Petermann |

**Abstract**

X-ray free electron lasers are powerful tools to investigate moderately to strongly correlated solid density low temperature plasmas, named warm dense matter. These plasmas are of most interest for astrophysics and laser plasma interaction, particularly inertial confinement fusion. This work utilizes the ultrashort soft x-ray pulse duration and high brilliance of the free electron laser in Hamburg, FLASH, to generate warm dense matter and to study its ultrafast processes. The techniques applied are absorption measurement, emission spectroscopy and Thomson scattering. Radiative hydrodynamics and Thomson scattering simulations are used to investigate the impact of temperature and density gradients in the sample and to fit the experimental data. The measurements result in a comprehensive picture of soft x-ray matter interaction related to warm dense matter and yield insight into ultrafast equilibration and relaxation mechanisms, in particular impact ionization and radiative recombination.

**Keywords:**
warm dense matter, free electron laser, Thomson scattering, spectroscopy

**Abstract**

Freie Elektronenlaser im Röntgenbereich sind mächtige Werkzeuge zur Untersuchung mäßig bis stark korrelierter niedrig-Temperatur Plasmen mit Festkörperdichte, sogenannter warmer dichter Materie. Diese Plasmen sind von größtem Interesse für Bereiche der Astrophysik sowie der Laser-Plasma-Wechselwirkung und insbesondere der Trägheitsfusion. Diese Arbeit nutzt die ultrakurzen Röntgenpulse und die hohe Brillanz des freie Elektronenlasers in Hamburg, FLASH, um warme dichte Materie zu generieren und die darin stattfindenden ultraschnellen Vorgänge zu untersuchen. Die verwendeten Methoden sind Absorptionsmessung, Emissionsspektroskopie und Thomson Streuung. Radiative Hydrodynamiksimulationen und Thomson Streuprogramme werden angewandt, um den Einfluß von Temperatur- und Dichtegradienten in der Probe auf das Streuspektrum zu untersuchen und um die experimentellen Daten anzufitten. Durch die Messungen entsteht ein umfassendes Bild der Interaktion zwischen der weichen Röntgenstrahlung und warmer dichter Materie. Im Detail geben sie Einblicke in die ultraschnellen Gleichgewichts- und Entspannungsmechanismen, speziell der Stoßionisierung und radiativer Rekombination.

**Schlagwörter:**
warme dichte Materie, freie Elektronenlaser, Thomson Streuung, Spektroskopie

Für meine Eltern

Uta und Rainer

# Publications

The main scientific results of this work were also published in peer reviewed journals. The publications form chapters in this thesis and are enumerated in the following table:

| | |
|---|---|
| Chapter 2.4<br>Reference [1]<br>Internet link | **Thomson scattering in dense plasmas with density and temperature gradients**, C. Fortmann, R. Thiele, R.R. Fäustlin, Th. Bornath, B. Holst, W.D. Kraeft, V. Schwarz, S. Toleikis, Th. Tschentscher, and R. Redmer, High Energy Density Physics **5**(3), p. 208-211, 2009. |
| Chapter 3.2<br>Reference [2]<br>Internet link | **Soft x-ray scattering using FEL radiation for probing near-solid density plasmas at few electron volt temperatures**, S. Toleikis, R.R. Fäustlin, L. Cao, T. Döppner, S. Düsterer, E. Förster, C. Fortmann, S.H. Glenzer, S. Göde, G. Gregori, R. Irsig, T. Laarmann, H.J. Lee, B. Li, J. Mithen, K.H. Meiwes-Broer, A. Przystawik, P. Radcliffe, R. Redmer, F. Tavella, R. Thiele, J. Tiggesbäumker, N.X. Truong, I. Uschmann, U. Zastrau, and Th. Tschentscher, High Energy Density Physics **6**(1), p. 15-20, 2010. |
| Chapter 3.4<br>Reference [3]<br>Internet link | **A compact soft x-ray spectrograph combining high efficiency and resolution**, R.R. Fäustlin, U. Zastrau, S. Toleikis, I. Uschmann, E. Förster, and Th. Tschentscher, Journal of Instrumentation **5**(02), p. P02004, 2010. |

Chapter 4.1
Reference [4]
Internet link

**Turning solid aluminium transparent by intense soft x-ray photoionization**, B. Nagler, U. Zastrau, R.R. Fäustlin, S.M. Vinko, T. Whitcher, A.J. Nelson, R. Sobierajski, J. Krzywinski, J. Chalupsky, E. Abreu, S. Bajt, T. Bornath, T. Burian, H. Chapman, J. Cihelka, T. Döppner, S. Düsterer, T. Dzelzainis, M. Fajardo, E. Förster, C. Fortmann, E. Galtier, S.H. Glenzer, S. Göde, G. Gregori, V. Hajkova, P. Heimann, L. Juha, M. Jurek, F.Y. Khattak, A.R. Khorsand, D. Klinger, M. Kozlova, T. Laarmann, H.J. Lee, R.W. Lee, K.H. Meiwes-Broer, P. Mercere, W.J. Murphy, A. Przystawik, R. Redmer, H. Reinholz, D. Riley, G. Röpke, F. Rosmej, K. Saksl, R. Schott, R. Thiele, J. Tiggesbäumker, S. Toleikis, Th. Tschentscher, I. Uschmann, H.J. Vollmer, and J.S. Wark, Nature Physics **5**(9), p. 693-696, 2009.

Chapter 4.2
Reference [5]
Internet link

**Bremsstrahlung and line spectroscopy of warm dense aluminum plasma heated by xuv free-electron-laser radiation**, U. Zastrau, C. Fortmann, R.R. Fäustlin, L.F. Cao, T. Döppner, S. Düsterer, S.H. Glenzer, G. Gregori, T. Laarmann, H.J. Lee, A. Przystawik, P. Radcliffe, H. Reinholz, G. Röpke, R. Thiele, J. Tiggesbaumker, N.X. Truong, S. Toleikis, I. Uschmann, A. Wierling, Th. Tschentscher, E. Förster, and R. Redmer, Physical Review E **78**(6), p. 066406, 2008.

Chapter 4.3
Reference [6]

**Observation of ultrafast non-equilibrium collective dynamics in warm dense hydrogen plasma**, R.R. Fäustlin, Th. Bornath, T. Döppner, S. Düsterer, E. Förster, C. Fortmann, S.H. Glenzer, S. Göde, G. Gregori, R. Irsig, T. Laarmann, H.J. Lee, B. Li, K.-H. Meiwes-Broer, J. Mithen, B. Nagler, A. Przystawik, H. Redlin, R. Redmer, H. Reinholz, G. Röpke, F. Tavella, R. Thiele, J. Tiggesbäumker, S. Toleikis, I. Uschmann, S.M. Vinko, T. Whitcher, U. Zastrau, B. Ziaja, and Th. Tschentscher, Physical Review Letters, accepted, 2010.

Furthermore, I have participated in the following projects related to this thesis. They cover aspects of soft x-ray matter interaction, scattering and necessary instrumentation:

- **Ultrafast Phenomena XVI: Proceedings of the 16th international conference: Soft x-ray Thomson scattering in warm dense matter at FLASH**, R.R. Fäustlin, S. Toleikis, Th. Bornath, L. Cao, T. Döppner, S. Düsterer, E. Förster, C. Fortmann, S.H. Glenzer, S. Göde, G. Gregori, A. Höll, R. Irsig, T. Laarmann, H.J. Lee, K.H. Meiwes-Broer, A. Przystawik, P. Radcliffe, R. Redmer, H. Reinholz, G. Röpke, R. Thiele, J. Tiggesbäumker, N.X. Truong, I. Uschmann, U. Zastrau, and Th. Tschentscher, Springer-Verlag Berlin Heidelberg New York, 2009, internet link.

- **Soft x-ray free electron laser microfocus for exploring matter under extreme conditions**, A.J. Nelson, S. Toleikis, H. Chapman, S. Bajt, J. Krzywinski, J. Chalupsky, L. Juha, J. Cihelka, V. Hajkova, L. Vysin, T. Burian, M. Kozlova, R.R. Fäustlin, B. Nagler, S.M. Vinko, T. Whitcher, T. Dzelzainis, O. Renner, K. Saksl, A.R. Khorsand, P.A. Heimann, R. Sobierajski, D. Klinger, M. Jurek, J. Pelka, B. Iwan, J. Andreasson, N. Timneanu, M. Fajardo, J.S. Wark, D. Riley, Th. Tschentscher, J. Hajdu, and R.W. Lee, Optics Express **17**(20), p. 18271-18278, 2009, internet link.

- **Plasma emission spectroscopy of solids irradiated by intense xuv pulses from a free electron laser**, T.W.J. Dzelzainis, J. Chalupsky, M. Fajardo, R.R. Fäustlin, P.A. Heimann, V. Hajkova, L. Juha, M. Jurek, F.Y. Khattak, M. Kozlova, J. Krzywinski, R.W. Lee, B. Nagler, A.J. Nelson, F. B. Rosmej, R. Sobierajski, S. Toleikis, Th. Tschentscher, S.M. Vinko, J.S. Wark, T. Whitcher, and D. Riley, High Energy Density Physics **6**(1), p. 109-112, 2010, internet link.

- **Soft x-ray laser driven ion acceleration and ablation in solids: niobium, vanadium and their deuterides**, J. Andreasson, B. Iwan, A. Andrejczuk, C. Caleman, M. Bergh, E. Abreu, R. Sobierajski, R.R. Fäustlin, G. Pálsson, B. Hjörvarsson, A.J. Nelson, S. Toleikis, H.N. Chapman, S. Bajt, J. Krzywinski, J. Chalupsky, L. Juha, P.A. Heimann, Th. Tschentscher, R.W. Lee, J. Hajdu, and N. Timneanu, Physical Review Letters, submitted, 2009.

- **Proceedings of SPIE: Soft x-ray Thomson scattering in warm dense hydrogen at FLASH**, R. R. Fäustlin, S. Toleikis, Th. Bor-

nath, T. Döppner, S. Düsterer, E. Förster, C. Fortmann, S. H. Glenzer, S. Göde, G. Gregori, R. Irsig, T. Laarmann, H. J. Lee, B. Li, K.-H. Meiwes-Broer, J. Mithen, A. Przystawik, H. Redlin, R. Redmer, H. Reinholz, G. Röpke, F. Tavella, R. Thiele, J. Tiggesbäumker, I. Uschmann, U. Zastrau, and Th. Tschentscher, 2009, internet link.

- **Measurement of the dynamic response of compressed hydrogen by inelastic x-ray scattering**, K. Falk, A.P. Jephcoat, B.J.B. Crowley, R.R. Fäustlin, C. Fortmann, F.Y. Khattak, A.K. Kleppe, D. Riley, S. Toleikis, J. Wark, H. Wilhelm, and G. Gregori, Journal of Physics: Conference Series, accepted, 2009.

- **Single pulse resonant magnetic scattering using a soft x-ray free-electron laser**, C. Gutt, S. Streit-Nierobisch, L.-M. Stadler, B. Pfau, C.M. Günther, R. Könnecke, R. Frömter, H. Stillrich, D. Stickler, H.P. Oepen, R.R. Fäustlin, R. Treusch, J. Feldhaus, E. Weckert, I.A. Vartanyants, M. Grunze, A. Rosenhahn, T. Wilhein, S. Eisebitt, and G. Grübel, Physical Review B, accepted, 2010.

- **Soft x-ray Thomson scattering at FLASH**, S. Toleikis, T. Döppner, R.R. Fäustlin, A. Przystawik, T. Bornath, S. Düsterer, E. Förster, C. Fortmann, S.H. Glenzer, S. Göde, G. Gregori, R. Irsig, T. Laarmann, H.J. Lee, B. Li, K.-H. Meiwes-Broer, J. Mithen, B. Nagler, P. Radcliffe, H. Redlin, R. Redmer, H. Reinholz, G. Röpke, F. Tavella, R. Thiele, J. Tiggesbäumker, I. Uschmann, S.M. Vinko, T. Whitcher, U. Zastrau and Th. Tschentscher, Journal of Physics B, in preparation, 2010.

- **Thomson scattering on inhomogeneous targets**, R. Thiele, Th. Bornath, W.-D. Kraeft, P. Sperling, R. Redmer, C. Fortmann, R.R. Fäustlin, S. Toleikis, Th. Tschentscher, M. Chen, and A. Pukhov, in preparation, 2010.

- **Ultrafast optical switching induced by high intensity XUV irradiation and plasma generation**, N. Stojanovic, et al., in preparation, 2010.

# Contents

**Abstract / Zusammenfassung** **v**

**Publications** **ix**

**Contents** **xiii**

**List of Figures** **xv**

**1 Introduction** **1**
1.1 Motivation . . . . . 1
1.2 Basic Plasma and Warm Dense Matter Properties . . . . . 4

**2 Theory and Simulations** **10**
2.1 Soft X-Ray Matter Interaction . . . . . 10
2.1.1 Photon Energy Deposition and Target Ionization . . . 10
2.1.2 Thermal Equilibration . . . . . 12
2.1.3 Plasma Cooling . . . . . 16
2.1.4 Low Intensity ps Approximation . . . . . 20
2.2 Helios - Radiative Hydrodynamics Code . . . . . 21
2.3 Soft X-Ray Thomson Scattering . . . . . 26
2.3.1 Overview . . . . . 26
2.3.2 The Dynamic Structure Factor . . . . . 29
2.4 Thomson scattering in dense plasmas with density and temperature gradients (paper) . . . . . 37

**3 Experiments and Equipment** **44**
3.1 The FLASH Facility . . . . . 44
3.2 Soft X-ray scattering using FEL radiation for probing near-solid density plasmas at few electron volt temperatures (paper) 48
3.2.1 Introduction . . . . . 48
3.2.2 Description of experimental techniques . . . . . 49
3.2.3 Experimental setup . . . . . 51

3.2.4 Results and discussion . . . . . 57
3.2.5 Conclusions . . . . . 60
3.3 Cryogenic Hydrogen Jet . . . . . 62
3.4 A Compact Soft X-Ray Spectrograph Combining High Efficiency and Resolution (paper) . . . . . 64
3.4.1 Introduction . . . . . 64
3.4.2 Design . . . . . 65
3.4.3 Measurements and Calibration . . . . . 68
3.4.4 Integration into FLASH experiments . . . . . 74
3.4.5 Conclusion . . . . . 75
3.5 Reference Spectrograph . . . . . 76
3.6 Temporal Overlap via Plasma Critical Surface Imaging . . . . 76
3.7 Time of Flight and Classifying Target Irradiation . . . . . 79

**4 Data Analysis and Interpretation 82**
4.1 Turning solid aluminium transparent by intense soft X-ray photoionization (paper) . . . . . 84
4.2 Bremsstrahlung and Line Spectroscopy of Warm Dense Aluminum Plasma heated by XUV Free-Electron Laser Radiation (paper) . . . . . 92
4.3 Observation of ultrafast non-equilibrium collective dynamics in warm dense hydrogen (paper) . . . . . 103

**5 Conclusion 111**

**6 Outlook 113**

**A Interactive Content 115**

**Comment on my Contribution 119**

**Acknowledgements 120**

**Curriculum Vitae 121**

**Bibliography 123**

**Index 142**

# List of Figures

1.1 Overview of various naturally occurring plasmas (red) as well as manmade plasmas and applications (shades of orange) with their approximate density and temperature, including inertial confinement (ICF) as well as plasmas generated by x-ray free electron lasers (XFEL) and the soft x-ray free electron laser in Hamburg (FLASH). The temperature is depicted in Kelvin and in eV ($k_B T$), while the density is shown in terms of free electrons per volume and as the related plasma frequency $\omega_{pe}$ (equation 1.7). The scales are compared to the electron rest energy $m_e c^2$ via the Boltzmann constant $k_B$, and via the Fermi energy. Lines of constant $\Gamma$ and $\Theta$ separate ideal, coupled and degenerate plasmas (see text). Based on [7, 8]. . . . . 5

1.2 Free electron temperatures and densities reached by irradiating solid aluminium and liquid hydrogen by soft x-ray radiation from FLASH (chapter 3.1, page 44) compared to coupling (red), degeneracy (blue) and scattering parameter (green, chapter 2.3, page 26). . . . . 7

1.3 Critical free electron density over wavelength (red, dashed) in comparison to hydrogen and aluminum solid density and regimes of some current and future light sources. Free electron laser sources like the European XFEL and FLASH are capable of probing higher than solid density plasmas. . . . . 9

2.1 Total photon cross section in aluminium $\sigma_{tot}$ and the different contributions: $\tau$, atomic photo-effect; $\sigma_{coh}$, coherent scattering, Rayleigh scattering, atom neither ionized nor excited; $\sigma_{incoh}$, incoherent scattering, Compton scattering off an electron; $\kappa_n$, pair production, nuclear field; $\kappa_e$, pair production, electron field; $\sigma_{ph}$, photonuclear absorption. The photon energy for the experiments of this work is indicated blue (91.8 eV). Based on [9]. . . . . 11

2.2 Overview of the main plasma heating, equilibration and relaxation processes during and after irradiation of a solid target with soft x-rays. The time scale indicates the related life times graphically. The atomic transitions are depicted exemplary for aluminium. . . . . 13

2.3 Average time between impact ionizations with an atomic hydrogen density of $4.2 \times 10^{22}\,\mathrm{cm}^{-3}$ (liquid density) and for the BEB [10] and Smirnov cross sections [11, 12]. . . . . 15

2.4 Radiative Recombination schematic showing the aluminium electronic structure (top panel) with an electron from the conduction band filling an L-shell hole. The bottom panel shows the emission spectrum resulting from an ensemble of such transitions. . . . . 19

2.5 Calculated temperature change in a magnetic multilayer $\sim$1 ps after irradiation by the FEL pulse onto the $Si_3N_4$ membrane. 21

2.6 Logarithmic plot of the cell boundaries, marked by lines in a simulation of aluminium irradiated by 92 eV photons with an intensity of $10.2\,\mathrm{J\,cm}^{-2}$ and a pulse duration of 30 fs. Initially, the target extends from 0 to 5 $\mu$m. . . . . 23

2.7 Comparison of Helios simulations in planar and spherical geometry with a 10 eV freely expanding hydrogen plasma at initially liquid density ($0.071\,\mathrm{g\,cm}^{-3}$). For planar geometry only the part expanding to positive coordinates is shown and the sample has an initial thickness of 20 $\mu$m. The spherical sample has an initial radius of 10 $\mu$m. . . . . 25

2.8 Thomson scattering geometry with linearly polarized probe light with incident ($k_0$), scattered ($k_1$) and differential ($k$) wave vectors (left), and sketch illustrating the microscopic length scale in the plasma, where $v$ is the electron velocity, $\lambda_D$ the Debye length, and $\lambda_*$ the probed length scale (right). See text for description. . . . . 27

2.9 Simulated collective ($\alpha > 1$) Thomson scattering spectrum illustrating the measurement of free electron temperature and density via detailed balance and plasmon dispersion, as well as the ion acoustic modes (ionic plasmons) which are typically not resolved in WDM experiments (from [13]). . . . . 28

2.10 Sketch of the frequency integrated DSF $S(k)$ for a dense plasma and frequency dependent DSF for various k-regimes (inserts). Based on [14]. . . . . 35

2.11 Ab-initio simulation of the inverse absorption length for cryogenic hydrogen at solid density as a function of the photon energy. The arrow indicates the FLASH energy (92 eV). . . . 40

2.12 Density (a) and temperature (b) profile from HELIOS simulation of liquid hydrogen droplet irradiated by XUV-FEL pulses, $\lambda_0 = 13.5\,\mathrm{nm}$, pulse length 30 fs, pulse energy $50\,\mu\mathrm{J}$ (bold curves). The dashed curves indicate the corresponding mean density and temperature. . . . . 41

2.13 Thin curves: Scattered intensity spectra at constant density and temperature corresponding to the HELIOS profiles (Fig. 2.12). Bold curve: Density and temperature averaged scattering spectrum. Scattering angle $\vartheta = 90°$. . . . . 41

2.14 Density and temperature averaged scattering spectrum (bold curve) compared to a calculation using the effective density and temperature (dashed curve) obtained from the plasmon peak positions and detailed balance analysis from the profile averaged spectrum. Scattering angle $\vartheta = 90°$. . . . . 42

3.1 Peak brilliance of current and future light sources over photon energy (based on [15, 16]). . . . . 45

3.2 Raytrace of the Thomson scattering and bulk solid target irradiation experimental setup from computer aided design drawings. Interactive CAD drawings of this setup are in the appendix (figure A.1). . . . . 46

3.3 Experimental setup for high intensity solid target irradiation and transmission measurement, here depicted without vacuum chamber. . . . . 47

3.4 Single-pulse spectra indicating the pulse-to-pulse fluctuation of the spectral distribution of incident SASE FEL pulses. The bold line corresponds to the spectral distribution averaged over 8 pulses and indicating the incident bandwidth of $\sim$2 eV corresponding to $\sim$2 % relative bandwidth. . . . . 52

3.5 Phase space representation for electron density $n_e$ and temperature $T_e$, probing photon energy $\hbar\omega = 92\,\mathrm{eV}$ and scattering angle $\Theta = 90°$. Lines for $\alpha = 0.5$; 1; 2 and $\Gamma = 1$ have been calculated according to the relations in the text and in equation (1). Filled areas indicate the expected parameter regimes for hydrogen and Al plasmas investigated. Densities of cold hydrogen and aluminum are indicated. . . . . 55

3.6 Scattering signal from a single FEL pulse of 60 mJ energy at the sample obtained at the CCD of the HiTraX spectrometer [3] after background subtraction. 500 counts in the maximum correspond to a very high S/N ratio that is well beyond 50. . 55
3.7 Soft X-ray Thomson scattering spectra near 92 eV from hydrogen integrated over 9000 FEL pulses. Scattering spectra for the cases that the 800 nm infrared laser hit the liquid hydrogen 3 ps prior (dots, broken line) and 3 ps after (crosses, dotted line) the FEL pulse are shown. Differentence spectra (error symbols, line) have been obtained from normalized scatter data after background subtraction. The corresponding FEL spectra and their difference are shown as dash-dotted lines. . . . . 58
3.8 The upper curve shows an unfiltered soft X-ray spectrum obtained from bulk aluminum following impact of 92 eV FEL radiation and the lower curve the spectrum for 1.6 eV infrared laser radiation using a 200 nm Zr filter. The intensities were $4 \times 10^{14}$ Wcm$^{-2}$ and $4 \times 10^{15}$ Wcm$^{-2}$, respectively. . . . . 59
3.9 Description of the hydrogen source components with (a) and without (b) heat shield. . . . . 62
3.10 Modulated hydrogen jet ejected from the cryogenic nozzle into the vacuum chamber. One can see how a droplet collides with another droplet which has been reflected by the chamber walls and is substantially slower than the stroboscopic illumination. See also the appendix for a video of the source (figure A.3). . 63
3.11 Geometry of the optics utilized in the spectrograph. Dimensions are in mm or degrees. . . . . 66
3.12 Three dimensional raytrace of the computer aided spectrograph design (a) indicating various components of the instrument in (right) and outside (right) of the manipulator. (b) Photograph of the spectrograph interior. . . . . 67
3.13 Measurement of the distance between different diffraction orders of the grating at various monochromator wavelength settings of the DORIS-III BW3 beam line. Data points from the $2^{nd}$ order have been entered with twice their wavelength to allow a common dispersion fit with the $1^{st}$ order. . . . . 69
3.14 Comparison of soft X-ray emission spectra from bulk aluminium irradiated by $4 \times 10^{14}$ W cm$^{-2}$ with a photon energy of 91.8 eV (13.5 nm, without filter, top blue line) and $4 \times 10^{15}$ W cm$^{-2}$ with a photon energy of 1.6 eV (800 nm, using a 200 nm zirconium-filter, bottom red line). From [2]. . . 71

3.15 Sharpness $\lambda/\Delta\lambda$ of different optical laser (red diamonds) and FEL (blue circles) generated aluminium plasma lines. The wavelength dependent resolution of the spectrograph can be estimated from sharpness of the FEL generated plasma line emission. . . . . 72

3.16 Efficiency or reflectivity of the spectrograph components according to the vendor specifications and the total efficiency of the optical elements (left), and the ratio of counts to isotropically emitted source photons (right) for different analog to digital converter (ADC) settings (see text). . . . . 74

3.17 Image of the slightly defocused 800 nm spot transmitted through the glass target when it impacts the glass before (a) and after (b) the focused FEL beam. In the latter case (b), the shadow of the plasma critical surface can be seen. . . . . 77

3.18 FEL irradiation generates a plasma on a glass target. The plasma critical surface can be imaged in transmission by backlighting with 800 nm, thus, finding temporal overlap of the two pulses. . . . . 78

3.19 Typical TOF signal recorded via the MCP showing a light peak and an electron peak which can be identified through the Helmholtz coils that compensate for the Earth's magnetic field, see text. . . . . 80

3.20 Integral TOF light peak signal over the GMD signal representing the FEL pulse energy, both in arbitrary units, for different pulses in a pulse train (a-d), many pulse repetitions (blue dots), and with fits for $I_{max}$ (red lines), see text. . . . . 81

4.1 A schematic diagram of the experimental setup. The energy of the incoming beam is measured by the Gas Monitor Detector (GMD). The beam is focused with an Off-Axis multilayer coated Mo/Si Parabola (OAP) onto the sample. The transmitted energy is measured by a silicon photodiode. . . . . 85

4.2 Al transmission as a function of fluence. The circles are the experimental data points with a $1\sigma$ error bar, the solid line is the theoretical prediction (see text). The dashed curve is the predicted electron temperature in eV (right Y-axis) in the valence band after the FEL pulse has passed, but before the L-shell holes are filled and the Auger recombination heats the band further. . . . . 87

4.3 Experimental soft x-ray emission spectrum (solid lines) of solid Aluminium for fluences of 0.6 J cm$^{-2}$, 0.3 J cm$^{-2}$ and 0.04 J cm$^{-2}$. Spectra are fitted (dashed lines) using (4.1) where we also include electron collision and Auger level broadening [17], resulting in temperatures of respectively 1.2 eV, 0.5 eV and 0.1 eV. Spectra are offset for clarity. . . . . 89

4.4 Experimental setup. a) The XUV pulses from the FEL undulators are focused by an elliptical beamline mirror on the bulk aluminum target, creating a 30 $\mu$m focus. b) The target is hit under 45° and plasma is created. A high-resolution XUV spectrometer observes the plasma emission under 45° to the surface normal. . . . . 94

4.5 Histogram of the energy spread of 13.5 nm XUV pulses generated by Self-Amplified Spontaneous Emission (SASE). Only pulses contributing to the measured spectrum of the performed experiment are shown. The top ordinate shows the corresponding irradiation intensities on target. . . . . 94

4.6 Experimental XUV photon spectrum per solid angle $\Delta\Omega$=4 $\times$ $10^{-4}$sr and wavelength interval $\Delta\lambda$=0.025 nm (symbols with error bars) and bremsstrahlung calculations for different electron temperatures. The spectrum is corrected for the spectrometer throughput and the detection efficiency. . . . . 96

4.7 Calculation of the relative Al ion species abundance from COMPTRA04 as a function of the electron temperature. Solid line is for Al density $\rho_{\mathrm{sol}} = 2.7\,\mathrm{g/cm^3}$, dashed line $0.5\,\rho_{\mathrm{sol}} = 1.35\,\mathrm{g/cm^3}$. . . . . 98

4.8 HELIOS simulation results for the electron density (left) and electron temperature (right) as a function of time and radius. 100

4.9 Experimental setup showing the liquid hydrogen jet in the focus of the FEL beam with typical time averaged spectrum, and the spectrograph at 90 ° scattering angle with the lineout region of the CCD, corresponding to the focussed part of the source image, marked by white bars. . . . . 105

4.10 Experimental spectrum (red circles) and the best fit of a calculated spectrum with $n_e = 2.8 \times 10^{20}\,\mathrm{cm^{-3}}$ and $T_e = 13\,\mathrm{eV}$ (solid blue line). Comparison to fits with variation in density (left graph), $5.6\times10^{20}\,\mathrm{cm^{-3}}$ (dashed green) and $1.4\times10^{20}\,\mathrm{cm^{-3}}$ (dash-dotted brown), and in temperature (right graph), 20 eV (dash-dotted brown) and 5 eV (dashed green), are shown. . . 106

4.11 Cluster simulation (a) with the FEL temporal profile (dotted blue) and the evolution of the ionization degree (solid green) as well as the electron temperature $T_e'$ (dashed red) using the Lieberman and Lichtenberg impact ionization. The electron kinetic energy distribution (b) 20 fs before (dotted green), at (dashed blue), and 20 fs after (dash-dotted red) the FEL pulse peak. A Maxwell-Boltzmann distribution fit at 0 fs (solid black) and the photoelectron (78.2 eV) and ionization (13.6 eV) energies are shown for comparison. . . . . 108
4.12 Measurements (colored circles) compared to the simulated evolution of the target's free electron density and temperature using different impact ionization cross sections and FEL pulse energies: Lieberman and Lichtenberg (solid red, 15 $\mu$J) and the BEB model (15 $\mu$J dashed blue, 60 $\mu$J dotted green). The FEL full width half maximum duration is indicated in gray scale. . . . . 109

A.1 Interactive CAD drawing of the experimental chamber used for Thomson scattering and bulk solid target irradiation. See also chapter 3.1. Cycle through different views by clicking here. . . . . 116
A.2 Interactive CAD drawing of the HiTRaX spectrograph. See chapter 3.4 for a detailed description. Cycle through different views by clicking here. . . . . 117
A.3 The increasing amplitude of the piezo actuator oscillation induces a controlled Rayleigh breakup of the hydrogen jet into droplets. The video is stroboscopically illuminated to observe the fast (∼60 m/s) droplets. Droplets bouncing off the vacuum chamber walls can be seen as streaks since they are much slower than the kHz illumination. See also section 3.3 . . . . 117
A.4 The electron kinetic energy distribution (red) assumes a Maxwell-Boltzmann distribution with the same average electron energy (blue) before the FEL pulse peaks. The simulation uses a Boltzmann solver [18, 19] to obtain the electron kinetic energy distribution during FEL irradiation of a hydrogen cluster with $10^5$ atoms. The FEL pulse has a Gaussian pulse shape with a full width half max duration of 40 fs, peaking at 40 fs simulation time, and an intensity of 85 TW cm$^{-2}$ (15 $\mu$J on target) at 13.5 nm. The BEB impact ionization cross sections are used here. See also chapters 2.1, 4.3, and figure 4.11. . . . 118

# Chapter 1

# Introduction

## 1.1 Motivation

Warm Dense Matter (WDM) is a challenge to modern physics and its investigation offers excellent means to understand strongly correlated multiparticle systems and their fast dynamics. It is a plasma state with a typical free electron temperature of some eV (some $10^4$ K) and free electron densities near and beyond solid density. In contrast to this, the so called ideal plasma has higher temperatures, lower densities and shows no particle correlations. Therefore, WDM is an intermediate state between condensed matter and the ideal plasma [20, 21]. The understanding of the condensed matter and the ideal plasma, two extremes in terms of particle correlations, has made significant progress. However, the intermediate regime, i.e. WDM, combines the moderate to strong particle correlation with a high thermal energy. It is, therefore, a great challenge to many-particle physics [7, 22]. In particular, the knowledge of WDM properties and their dependence on temperature, density and pressure is of paramount importance to various fields of physics.

The topics that make the investigation of WDM worthwhile undertaking range from astro- over laser-matter and energy physics to industry grade applications. In astrophysics WDM is present under stable conditions in the interiors of giant planets, such as Jupiter, Saturn, Uranus, Neptune and more than 300 exoplanets, but also in brown dwarfs [23]. The depth dependent composition of the planets strongly depends on the WDM properties of mainly hydrogen and helium and especially their equation of state [24–27]. WDM also plays a major role as a transient state in the gravitational collapse of interstellar gas to form stars. The rate of such star formation depends on the properties of the plasma during the collapse. Current efforts to model the process cannot explain the observed rate of star formation [28].

During laser matter interaction, WDM is generated as a transient state between the solid target and the ideal plasma which is formed by the laser ablated blowoff. This process occurs on a daily basis not only in the laboratory, but also in industry applications like material processing and treatment (e.g. [29]) or even medical applications, e.g. ablative laser eye correction [30]. A greater understanding of WDM could increase the efficiency and capability of these processes. A special case of laser matter interaction is inertial confinement fusion where a mm size deuterium and/or tritium capsule is shock compressed and heated to ignite fusion. During the compression and heating phase the WDM regime is crossed and instabilities in the target shape, mainly Rayleigh-Taylor, can occur [31–33]. The fusion reaction vitally depends on the prevention of the instabilities which can only be modeled and predicted correctly if the plasma properties are well understood.

Furthermore, WDM shares common principles with other coupled systems such as semiconductors, high temperature superconductors and ultracold trapped atoms. All of these applications require the understanding of strongly interacting particle and their many-body correlations. Hence, the increased understanding of one system, e.g. WDM, can be transferred to other systems of correlated particles possibly leading to high impact application in sectors such as energy, telecommunications and microchips [21].

Since theoretical models are ambiguous, experimental observations are vital for the understanding of WDM (e.g. [34]). However, the generation of WDM in homogeneous quantities larger than $\mu m^3$ and its observation under controlled laboratory conditions is a tough task. For example, common optical short-pulse laser heating of matter is strongly non-linear leading to rapid temporal and spatial variations, steep spatial gradients down to the nm scale, and a broad spectrum of plasma physical processes. A promising way to generate larger quantities of WDM is by ion heating, which can reach pulse durations down to 20 ns. Heavy ion accelerator facilities such as the Gesellschaft für Schwerionenforschung (GSI) in Darmstadt are constructing new facilities which will also be used for this approach (FAIR [35–37]). More pioneering techniques in the generation and investigation of WDM are laser based and include shocks, x-ray and heating by energetic ion or electron deposition [38–47].

In addition, WDM relaxes on ps to ns time scales into ideal plasma or condensed matter states. Therefore, fast diagnostic techniques are required and often only temporally integrated measurements can be conducted. One of the most powerful plasma diagnostics is Thomson scattering (TS), as it enables the measurement of plasma temperature, density and degree of ionization by recording the scattering spectrum of an electromagnetic wave. This probing light must be in the x-ray regime to penetrate WDM and so

TS was transferred from the optical [48] into the x-ray regime. Also, the currently used laser based plasma x-ray sources advance into the relevant ps time scales. Thus, Thomson scattering has by now become a well developed technique in the WDM regime [22, 34, 49–52].

With the advent of the first high brightness soft x-ray free electron laser in Hamburg (FLASH), we are able to take TS to the ultrafast fs timescale [13, 53]. This allows us to diagnose non-equilibrium plasmas and their equilibration mechanisms, in particular Coulomb collisions, which are the fundamental particle interactions in plasmas. The high brightness of FEL sources allows measurements with unprecedented accuracy, as we will see in chapter 4.3 (page 103). We also use simulations of the soft x-ray sample interaction to investigate the impact of temperature and density gradients on the scattering spectrum (chapter 2.4, page 37). We find that the gradients produced by the soft x-rays do not significantly affect the TS measurement. FLASH enables us to generate WDM more homogeneously than optical lasers would, since the soft x-ray photons have large penetration depths in light elements (e.g. $10\,\mu$m for liquid hydrogen). The penetration depth can be further increased by exposing the sample to particularly high intensity radiation, so called saturable absorption. We measure this effect via the transmission of the sample and find that it is a viable way of generating very homogeneous WDM (chapter 4.1, page 84). Furthermore, we record time integrated plasma emission spectra which contain features from bremsstrahlung, line emission and radiative recombination. Each of those features allows us to measure the plasma temperature. With simulations we can determine the time scale for each process outlining the evolution of the plasma temperature (chapter 4.2, page 92).

Moreover, FLASH is an ideal test bed for current and upcoming x-ray free electron lasers and their capabilities related to WDM research. The Linac Coherent Light Source (LCLS, in user operation since 2009), the SPring-8 Compact SASE Source (SCSS, planned for 2010), and the European X-ray FEL (planned for 2014) are the most prominent of these sources. They are capable of producing ultrafast x-ray pulses at wavelengths in the Angström range. These pulses will penetrate even matter from heavier elements deeply in order to generate homogenous plasmas and to probe those via TS with still higher accuracy. The resolution of these sources will even allow a direct measurement of the ion and electron temperature at the same time [54], so that a more detailed analysis of the particle interaction is possible.

This work concentrates on pioneering WDM research on x-ray free electron lasers. Thus, an important aspect is giving a greater audience access to the knowledge acquired through this work via peer reviewed publications. A list of these publications can be found on page ix and the ones most im-

portant for this thesis form chapters within it. Those chapters are marked as "(paper)" in the table of contents and with annotations in the respective chapters. The publications in this thesis relate to the simulation of soft x-ray matter heating and the impact of gradients on the TS spectrum ([1] chapter 2.4, page 37), the construction of a high resolution and throughput spectrograph ([3] chapter 3.4, page 64), the generation of WDM via saturable absorption, the related transmission and spectroscopic radiative recombination temperature measurement ([4] chapter 4.2, page 84), the spectroscopic temperature measurement via bremsstrahlung and line emission in combination with simulations ([5] chapter 4.2, page 92), and the temperature and density measurement via TS of homogenously heated hydrogen ([6] chapter 4.3, page 103).

Prior to the presentation of these papers and the analysis of experiments, an overview of the current knowledge and methods is given. This comprises basic plasma properties (chapter 1.2, page 4), soft x-ray matter heating (chapter 2.1, page 10), hydrodynamic simulations (chapter 2.2, page 21), Thomson scattering (chapter 2.3, page 26), and the employed experimental setup (chapter 3, page 44).

## 1.2 Basic Plasma and Warm Dense Matter Properties

This section introduces some basic quantities to describe plasmas and in particular the WDM state investigated here. Plasma is ionized matter of any element composition. There is no clear distinction at which degree of ionization one speaks of a plasma. In the context of this work every sample that contains free electrons will be considered a plasma. Furthermore, electrons which are mobile throughout the plasma extent are regarded as free. The fundamental plasma properties include the element composition, its free electron density $n_e$ and free electron temperature $T_e$. One often refers to these quantities simply as plasma density and temperature, as mostly the free electrons contribute to the plasma typical properties. However, the temperature of other plasma components (ions, atoms, bound electrons) can be significantly different from those of the free electrons, as is mostly the case for ultrafast time scales (e.g. ultrafast laser heated plasma). Here, we will consider plasmas with electronic, ionic and neutral (atomic) components which consist of only one element and are charge neutral, i.e. $Z_f n_i = n_e$ where $Z_f$ is the average number of free electrons per nucleus and $n_i$ the combined atomic and ionic density.

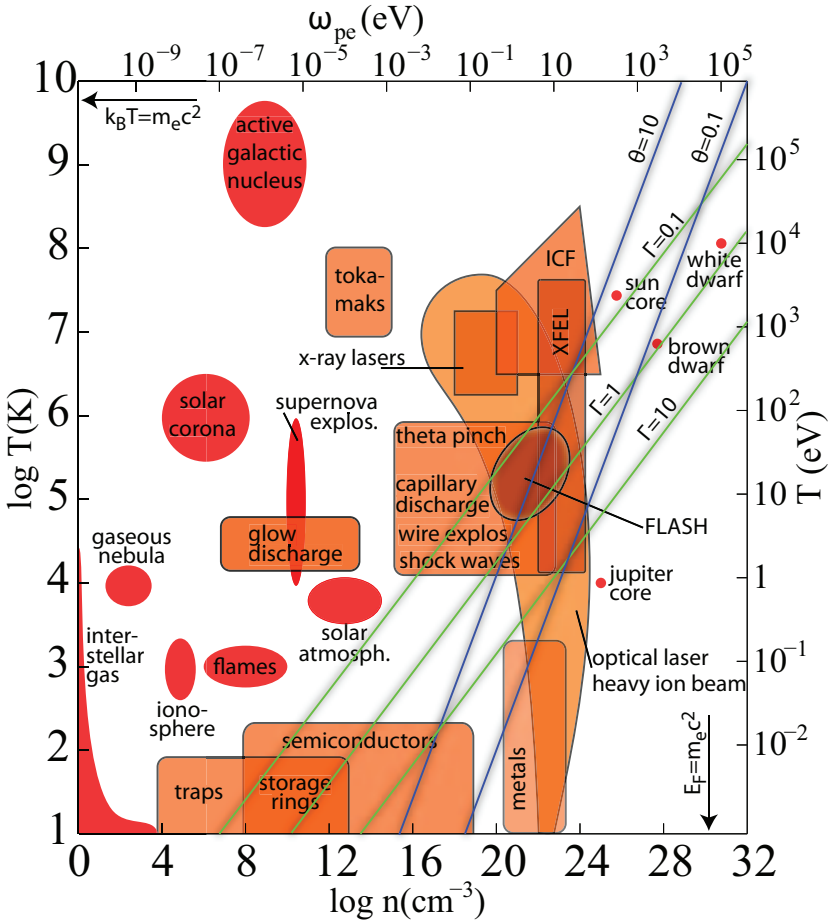


Figure 1.1: Overview of various naturally occurring plasmas (red) as well as manmade plasmas and applications (shades of orange) with their approximate density and temperature, including inertial confinement (ICF) as well as plasmas generated by x-ray free electron lasers (XFEL) and the soft x-ray free electron laser in Hamburg (FLASH). The temperature is depicted in Kelvin and in eV ($k_BT$), while the density is shown in terms of free electrons per volume and as the related plasma frequency $\omega_{pe}$ (equation 1.7). The scales are compared to the electron rest energy $m_ec^2$ via the Boltzmann constant $k_B$, and via the Fermi energy. Lines of constant $\Gamma$ and $\Theta$ separate ideal, coupled and degenerate plasmas (see text). Based on [7, 8].

Plasmas in nature and the laboratory span a great parameter space in $n_e$ and $T_e$ (figure 1.1) - from cold dilute interstellar over hot dense inertial confinement fusion plasmas to stellar cores [7, 8, 55]. One can further classify plasmas by the correlation of its particles. This is done by comparing the thermal energy $E_{th}$ to the Coulomb potential $V_c$ and the Fermi energy $E_f$ in the plasma [7, 8, 22], where

$$E_{th} = k_B T_e = \left(\frac{T_e}{\mathrm{eV}}\right) \mathrm{eV} = 8.617 \times 10^{-5} \left(\frac{\mathrm{T_e}}{\mathrm{K}}\right) \mathrm{eV}, \tag{1.1}$$

$$V_{Cb} = \frac{e^2}{4\pi\varepsilon_0 a} = 2.321 \times 10^{-9} \left(\frac{n_e}{\mathrm{m}^{-3}}\right)^{1/3} \mathrm{eV}, \tag{1.2}$$

$$E_F = \frac{\hbar^2 k_F^2}{2m_e} = 3.646 \times 10^{-19} \left(\frac{n_e}{\mathrm{m}^{-3}}\right)^{2/3} \mathrm{eV}, \tag{1.3}$$

with the Wigner-Seitz-radius $a = (4\pi n_e/3)^{-1/3}$, the Fermi wave number $k_F = (3\pi^2 n_e)^{1/3}$, the Boltzmann constant $k_B$, the electron rest mass $m_e$, the electron charge $e$, and the vacuum permittivity $\varepsilon$.

One parameter to compare these energies is the coupling parameter

$$\Gamma = \frac{V_{Cb}}{E_{th}} = 2.321 \times 10^{-9} \left(\frac{n_e}{\mathrm{m}^{-3}}\right)^{1/3} \left(\frac{\mathrm{eV}}{T_e}\right). \tag{1.4}$$

If $\Gamma \ll 1$, the energy of the particles in the Coulomb potential will be negligible in comparison to their random kinetic energy, i.e. their thermal energy. Thus, the particle locations will be randomly distributed throughout the spatial extent of the plasma. The plasma then behaves much like a gas and one speaks of an ideal plasma. In contrast to this, as $\Gamma$ approaches unity and for $\Gamma > 1$, the Coulomb potential of the particles is no longer negligible. Thus, the particles will arrange their average locations to minimize the potential energy. With increasing $\Gamma$ more particles will have the same distance to their neighbors, like in a liquid, up to the point where the particles form a lattice, much like an ionic crystal. For $\Gamma \geq$ one speaks of a coupled plasma. Thus, $\Gamma$ is a good indicator for the correlation of the particles and their related macroscopic behavior. The colder and denser a plasma is, the stronger it is coupled and the higher is $\Gamma$.

The relevance of quantum mechanical effects in the plasma can be estimated via the degeneracy parameter

$$\Theta = \frac{k_B T_e}{E_F} = 2.742 \times 10^{18} \left(\frac{n_e}{\mathrm{m}^{-3}}\right)^{-2/3} \left(\frac{T_e}{\mathrm{eV}}\right). \tag{1.5}$$

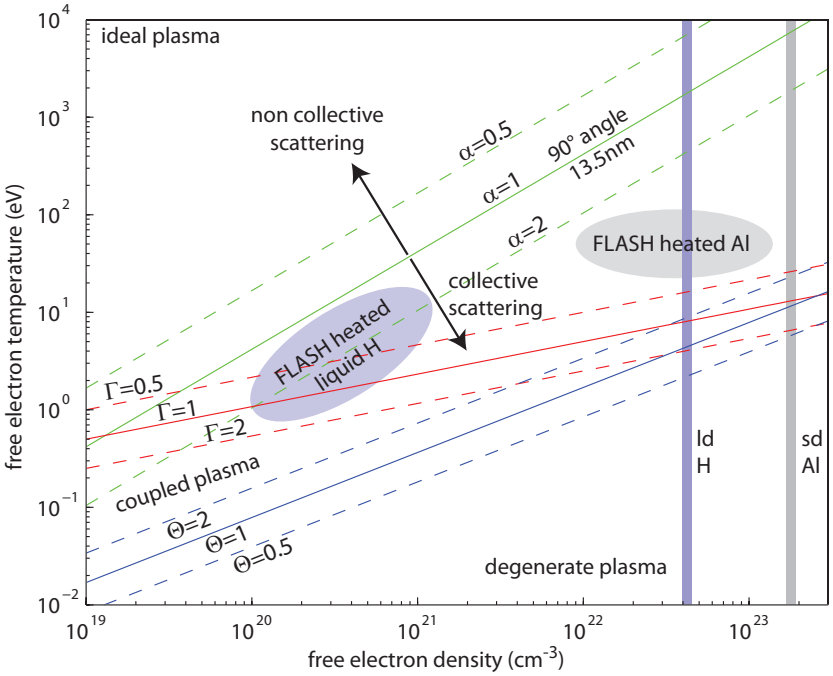


Figure 1.2: Free electron temperatures and densities reached by irradiating solid aluminium and liquid hydrogen by soft x-ray radiation from FLASH (chapter 3.1, page 44) compared to coupling (red), degeneracy (blue) and scattering parameter (green, chapter 2.3, page 26).

If $\Theta \gg 1$, the thermal energy is much larger than the Fermi energy in the plasma and the electron kinetic energy distribution is well described with a Maxwell-Boltzmann distribution. As $\Theta$ approaches unity the Pauli exclusion principle becomes important and the electrons follow a Fermi distribution. At $\Theta < 1$ one speaks of a degenerate plasma.

In this context, WDM is a coupled and possibly degenerate plasma. The strong particle coupling makes the theoretical description of the plasma more difficult than in the ideal plasma. It is also challenging to describe WDM with solid state physics, as the energy density in the plasma allows many additional processes to occur. Thus, experiments are needed to differentiate different models that exist in this regime [22, 56]. This work concentrates on ultrafast processes in WDM. The coupling and degeneracy parameters are depicted for a wide range of plasmas in figure 1.1 and for the plasmas relevant to this work in figure 1.2.

The distance over which the charged plasma particles interact is determined by the screening or Debye length $\lambda_D$ of the plasma. It is derived

analytically for a test charge in an ideal plasma [55, 57, 58]:

$$\lambda_D = \sqrt{\frac{\varepsilon_0 k_B T_e}{e^2 n_e}} = 7.434 \times 10^3 \sqrt{\frac{T_e}{\mathrm{eV}}} \sqrt{\frac{\mathrm{m}^{-3}}{n_e}}\,\mathrm{m} \tag{1.6}$$

Another important aspect for the investigation of plasmas are its optical properties. A key parameter for this interaction is the frequency with which the electrons oscillate in the plasma. This electronic plasma frequency $\omega_{pe}$ can be derived assuming collective free electron oscillations around their rest positions in the static ionic background. Here, in terms of an analytic expression [55, 57, 58] and in practical units of energy $E_{pe}$ in eV:

$$\omega_{pe} = \sqrt{\frac{e^2 n_e}{\varepsilon_0 m_e}}, \tag{1.7}$$

$$\left(\frac{E_{pe}}{\mathrm{eV}}\right) = 3.713 \times 10^{-14} \sqrt{\frac{n_e}{\mathrm{m}^{-3}}}. \tag{1.8}$$

Light with an angular frequency $\omega_{ph}$ lower than the plasma frequency cannot penetrate the plasma beyond the skin depth $\sim c/\omega_{pe}$ (speed of light $c$) and is reflected. Such a plasma with $\omega_{ph} < \omega_{pe}$ is called over-dense while for $\omega_{ph} > \omega_{pe}$ the plasma is under-dense. The plasma density for which $\omega_{ph} = \omega_{pe}$ is called critical density. Homogeneous plasma heating and plasma probing with light is only possible in under-dense plasmas. This limits the capability of optical and infrared lasers to generate dense plasmas homogeneously or to probe them. For WDM one typically has to use at least photon energies in the soft x-ray range. Figure 1.3 shows $\omega_{pe}$ over $n_e$ as well as different light sources capable of probing the plasma.

A more detailed description of the soft x-ray matter interaction and related plasma generation will be given in the next section. An overview of the most important plasma processes from fs to ns timescales is presented after that, starting page 12.

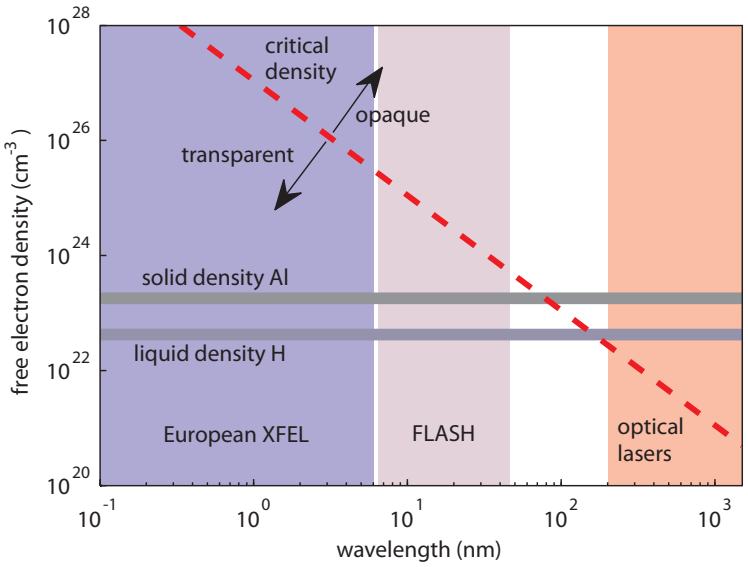


Figure 1.3: Critical free electron density over wavelength (red, dashed) in comparison to hydrogen and aluminum solid density and regimes of some current and future light sources. Free electron laser sources like the European XFEL and FLASH are capable of probing higher than solid density plasmas.

# Chapter 2

# Theory and Simulations

## 2.1 Soft X-Ray Matter Interaction

This work concentrates on the generation and probing of WDM plasmas using soft x-rays. Thus, the interaction of the radiation with matter is an important aspect. The following chapters give an overview of the absorption of soft x-rays in matter (chapter 2.1.1) and the subsequent processes that lead to a distribution of the deposited energy (chapter 2.1.2) and the sample relaxation (chapters 2.1.3, 2.2).

### 2.1.1 Photon Energy Deposition and Target Ionization

The type of interaction photons undergo with matter strongly depends on their energy. Figure 2.1 shows the dominant interaction of low intensity light with aluminium from high energetic $\gamma$-radiation down to the ultra violet [9, 59, 60]. Above $\sim 10^7$ eV photon energy pair production dominates. At lower photon energies Compton scattering becomes the major interaction and below $\sim 10^5$ eV x-rays and soft x-rays mainly react via photoionization.

When the energy of a single photon $E_{ph}$ is insufficient to overcome the first ionization energy $E_I$, the target material can still be ionized via non-linear effects relying on the radiation's high intensity. These effects are with increasing intensity multi-photon, tunnel, and above threshold ionization [61]. High intensity radiation can also lead to the alteration of cross sections (fig. 2.1) in the $E_{ph} > E_I$ regime when dominantly interacting electronic states are excited within a first fraction of the light pulse and cannot contribute to the absorption for the remaining pulse. This is also referred to as saturable absorption or target bleaching. It has been observed within this work at 92 eV photon energy and an intensity above $1\,\mathrm{PW\,cm^{-2}}$ [4] (chapter 4.1) leading to more homogeneous target heating. X-ray and soft x-ray experiments are

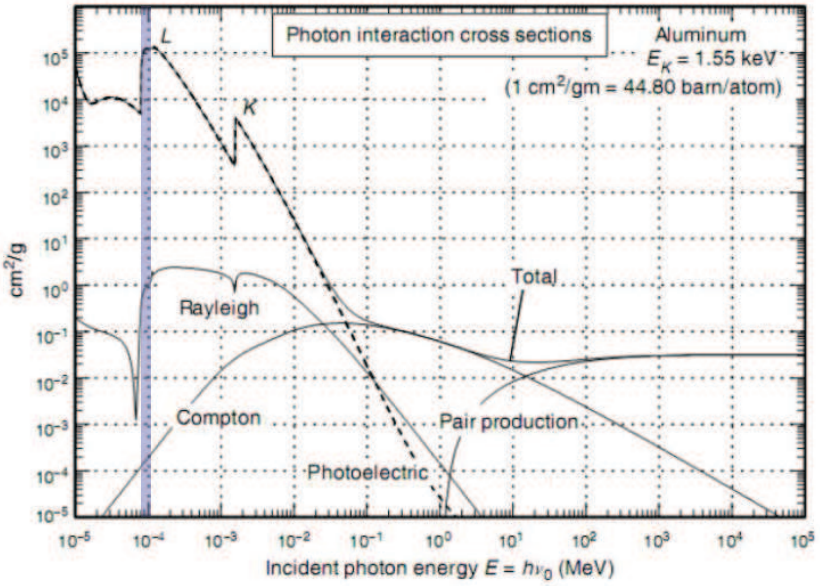


Figure 2.1: Total photon cross section in aluminium $\sigma_{tot}$ and the different contributions: $\tau$, atomic photo-effect; $\sigma_{coh}$, coherent scattering, Rayleigh scattering, atom neither ionized nor excited; $\sigma_{incoh}$, incoherent scattering, Compton scattering off an electron; $\kappa_n$, pair production, nuclear field; $\kappa_e$, pair production, electron field; $\sigma_{ph}$, photonuclear absorption. The photon energy for the experiments of this work is indicated blue (91.8 eV). Based on [9].

often situated well below this intensity so that the penetration depth does not depend on the irradiation intensity.

If the material is an electronic conductor or once it has been partially ionized, more photon energy can be deposited via a variety of plasma heating mechanisms, of which the most common are inverse bremsstrahlung, stimulated Brillouin and stimulated Raman scattering [57, 62]. These plasma processes play a major role when plasmas are created with optical lasers, often 800 nm Titan-Saphire based. They are less relevant for high photon energies where, as e.g. inverse bremsstrahlung absorption scales as $E_{ph}^{-2}$ [57, 62]. In the case of soft x-rays, the absorption mechanisms are usually limited to mainly photoionization and partially inverse bremsstrahlung.

During the irradiation and photoionization with x-rays the target material becomes a plasma. Its degree of ionization will depend on the properties of the material and the light. The photon energy is deposited in the electronic system only and the freed photoelectrons are initially not in thermal equilibrium with atoms, ions and other free electrons in the plasma. Initially the photoelectrons do not form a Maxwell-Boltzmann distribution, but form a narrow peak at a kinetic energy $E_{ph} - E_I$ depending on the ionization energy $E_I$ of the ionized atomic level. The following chapter presents the most important processes in the cascade which leads to the equilibration of photoelectrons with the other plasma species. Over time, all species assume a Maxwell-Boltzmann distribution with the same temperature. The most relevant equilibration processes are particle collisions, including impact ionization, and Auger decay (chapter 2.1.2). Meanwhile, the plasma cools via bremsstrahlung emission and radiative recombination (chapter 2.1.3). Spectral line emission (chapter 2.1.3) further cools the plasma after ps to ns when hydrodynamic expansion sets in (chapter 2.2). Figure 2.2 gives a rough estimate on the time scales for individual processes in a dense aluminium plasma or a similarly excited sample. This figure is a compilation of the knowledge presented in chapters 2.1.2 through 2.2. It also contains results of this work on impact ionization (chapter 4.3), Auger decay, radiative recombination (chapter 4.1), bremsstrahlung and line emission (chapter 4.2). The estimates of the figure also apply to the hydrogen sample in this work, with the exception of Auger decay.

### 2.1.2 Thermal Equilibration

This section discusses the main processes that lead to a redistribution of thermal energy between the plasma species and an equilibration of their temperature.

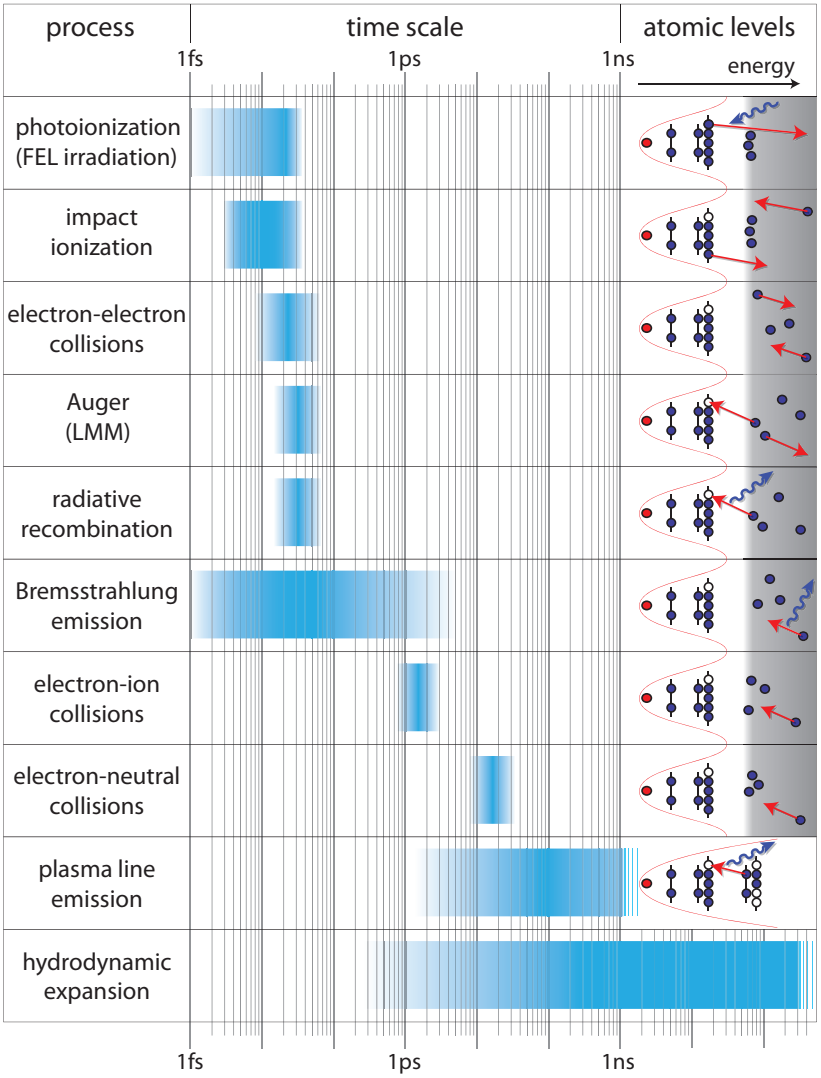


Figure 2.2: Overview of the main plasma heating, equilibration and relaxation processes during and after irradiation of a solid target with soft x-rays. The time scale indicates the related life times graphically. The atomic transitions are depicted exemplary for aluminium.

### Particle Collisions

The most relevant collisions in plasmas are electron-electron, electron-ion and electron-neutral. The collisions lead to an energy transfer between the particles and thus equilibrate the plasma species. The rate of temperature change for species $\alpha$ is given by [58]

$$\frac{dT_\alpha}{dt} = \nu_\varepsilon^{\alpha/\beta} \left(T_\beta - T_\alpha\right), \tag{2.1}$$

with the transfer rate

$$\left(\frac{\nu_\varepsilon^{\alpha/\beta}}{s^{-1}}\right) = 1.4 \times 10^{-7} \left(\frac{n_\beta}{cm^{-3}}\right) Z_\alpha^2 Z_{f,\beta}^2 \sqrt{\frac{m_\alpha m_\beta}{u^2}} \left(\frac{m_\alpha T_\alpha + m_\beta T_\beta}{eVu}\right)^{3/2} \Lambda_{\alpha\beta}, \tag{2.2}$$

where $T$ denotes the temperature, $m$ the mass in proton masses (u), $Z_f$ the charge state, and $n$ the density of the species $\alpha$ and $\beta$ marked by indices. The Coulomb logarithm $\Lambda$ is the ratio of maximum and minimum distance (impact parameter) between two particles undergoing a small angle Coulomb collision [57]. Practical units for $\Lambda$ and various species are given in [58].

The collision frequency of a charged species with neutral atoms is given by [58]

$$\left(\frac{\nu_{\alpha 0}}{s^{-1}}\right) = 5 \times 10^{-15} \left(\frac{n_0}{cm^{-3}}\right) \sqrt{\frac{T_\alpha}{eV}} \sqrt{\frac{u}{T_\alpha}}, \tag{2.3}$$

with the neutral density $n_0$. Note that usually many collisions are necessary to reach thermal equilibrium. Therefore, equation 2.3 gives a lower limit for the thermalization time ($\tau_{th} > 1/\nu_{\alpha 0}$).

### Impact Ionization

Impact ionization can be seen as a special case of a collision where a free electron collides with a bound one transferring at least the binding energy so that both electrons are free afterwards. A classical model based on a resting bound electron has been developed by J.J. Thomson in 1912 [63]. Smirnov extends this model to take the orbital electron motion and its radial distribution into account [11, 12], yielding an impact ionization cross section

$$\sigma_{iz} = \frac{\pi}{4}\left(\frac{e}{4\pi\varepsilon_0}\right)^2 \frac{1}{E_e} \left(\frac{5}{3E_{iz}} - \frac{1}{E_e} - \frac{2E_{iz}}{3E_e^2}\right), \tag{2.4}$$

where $e$ is the electron charge, $\varepsilon_0$ the vacuum permittivity, and $E_{iz}$, $E_e$ with $E_{iz} < E_e$ are the binding and free electron kinetic energies, respectively.

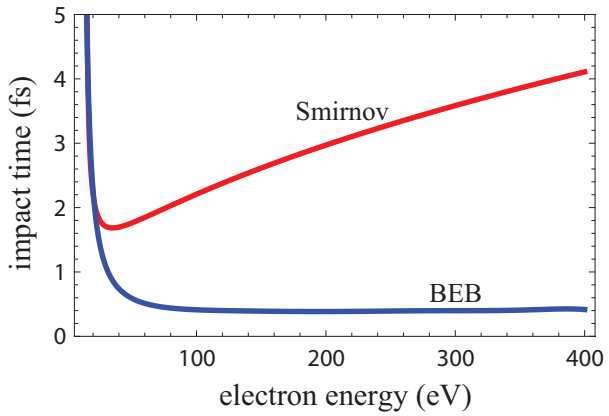


Figure 2.3: Average time between impact ionizations with an atomic hydrogen density of $4.2 \times 10^{22}\,\mathrm{cm}^{-3}$ (liquid density) and for the BEB [10] and Smirnov cross sections [11, 12].

The Binary Encounter Bethe (BEB) model [10] additionally takes the atomic or ionic dipole moments into account. It is commonly used and tabulated values for various elements and electron energies are available from the National Institute of Standards and Technology [64]. Its predictions compare well to measurements of not pre-ionized targets (e.g. [65]). Figure 2.3 compares impact ionization times from equation 2.4 and BEB for Hydrogen and electron kinetic energies up to 400 eV. The two models differ more than a factor of six in this regime.

As one of the main results of this work we find that measurements with dense hydrogen plasmas compare significantly better with equation 2.4 than with BEB. The related experiments are described in the publication of chapter 4.3 [6]. Apparently, the detailed atomic structure becomes negligible in the presence of a dense plasma environment. However, it is not fully understood why Smirnov's impact ionization model is in better agreement with the dense plasma experiment. Further investigation is required and the outlook (chapter 6) gives an overview of possibly responsible mechanisms.

### Auger Decay

In the plasmas discussed here, core shell holes are generated via photoionization with soft x-rays, which have sufficient energy to ionize the L-shell electrons of light metals. The holes are then repopulated via Auger decay and radiative recombination.

The Auger life time for an L-shell hole in e.g. aluminium is estimated to be ∼40 fs [66]. From our measurement of saturable absorption ([4], chapter 4.1) we know that the Auger life time of the L-shell hole must be longer than the FEL pulse duration of ∼40 fs. The LMM-Auger process generates a conduction band electron with approximately 70 eV kinetic energy which can

further heat the system of free electrons via collisions (chapter 2.1.2). The Auger process and its impact on the plasma evolution can be estimated using Monte-Carlo simulations [67].

#### Three-Body Recombination

A free electron with more energy than the atomic ionization energy can be captured by an ion into a high lying atomic state while transferring its excess energy to another free electron. This is called three-body recombination (TBR) [68]. It is the inverse process to impact ionization. As such, the TBR cross section $\sigma_{TBR}$ and relevant time scales can be obtained from the impact ionization cross section $\sigma_{iz}$ using the microscopic reversibility relation [69]

$$\sigma_{TBR}\left(E_e\right) = \frac{g_2}{g_1}\frac{E_e + E_{iz}}{E_e}\sigma_{iz}\left(E_e + E_{iz}\right), \tag{2.5}$$

where $g_1$ and $g_2$ are the statistical weights of the initial and end states, respectively. The impact ionization cross section $E_{iz}$ is described in section 2.1.2 and depends on the ionization $E_{iz}$ and electron energy $E_e$.

The experimental conditions considered in chapter 4.3 [6] are a hydrogen plasma with 1% ionization, and an electron density and temperature of $3 \times 10^{20}\,\mathrm{cm}^{-3}$ and 13 eV, respectively. This gives an average time between TBRs is in the range of 300 fs. Thus, TBR does not play a major role during the FEL pulse duration. It becomes important at higher degrees of ionization and ps timescales [19]. Simulations with a Boltzmann solver evaluating the kinetic equations for the free electron distribution include TBR [18, 19] and were used to analyze the experiments (chapter 4.3 [6]).

An approximation for TBR under local thermal equilibrium conditions is also given in reference [58].

### 2.1.3 Plasma Cooling

This section discusses the main processes that lead to a reduction of thermal energy in the plasma. The processes are all radiative, as we assume a vacuum environment and no loss of particles. The processes take place over fs to ns time scales, thus, they partially occur in parallel to the equilibration mechanisms described in the previous section (page 12).

#### Bremsstrahlung Emission

The intensity distribution of bremsstrahlung emission $dI_{br}/d\lambda$ by a plasma with a Maxwell-Boltzmann electron kinetic energy distribution is described by Kramer's law [70]. In practical units it is

$$\left(\frac{dI_{br}(\lambda)/d\lambda}{W/nm}\right) = 1.90 \times 10^{-23} Z_f \exp\left(-1239.8\left(\frac{eV}{T_e}\right)\left(\frac{nm}{\lambda}\right)\right) \times \left(\frac{nm}{\lambda}\right)^2 \left(\frac{n_e}{cm^{-3}}\right)^2 \left(\frac{eV}{T_e}\right)^{1/2} V, \tag{2.6}$$

with the average degree of ionization $Z_f$, the wavelength $\lambda$, the free electron density and temperature $n_e$ and $T_e$, and the emitting sample volume $V$. In the case of soft x-ray excited sample and negligible hydrodynamic expansion, $V = A \times l$, where $A$ is the irradiated area and $l$ the penetration depth of the soft x-rays.

In the experiment the bremsstrahlung emission can be recorded spectrally and used to determine the electron temperature via the spectral shape of the emission (figure 4.6 in chapter 4.2 on page 96, [5]). The free electron density $n_e$ can also be measured if the spectrograph is photon calibrated and the quantities $V$ and $Z_f$ are known. The degree of ionization can be estimated by identifying specific emission lines (section 2.1.3).

Due to the quadratic $n_e$ dependance the main bremsstrahlung emission occurs while the sample is still dense and hydrodynamic expansion has not yet set in. The timescale for this depends on the sample size. We simulate the temporal evolution of a an aluminium target irradiated by 92 eV photons with a penetration depth of ∼40 nm (figure 4.8 in chapter 4.2 on page 100, [5]). From that we find that the sample free electron density stays mostly constant for the first ∼200 fs. About 2 ps after irradiation the bremsstrahlung emission drops to half of its maximum as the density falls to $2^{-1/2}$ of its peak due to hydrodynamic expansion. Thus, the bremsstrahlung emission will mainly occur within ps after excitation.

### Radiative Recombination

Radiative recombination is an electronic free-bound transition. In aluminium the radiative recombination life time of an L-shell hole is about 10 ps [66]. The process competes with Auger decay for the repopulation of bound levels. As Auger decay has much shorter life times for the plasmas considered here (∼40 fs), only some per mill of the bound holes will be filled via radiative recombination [66]. Also, once the bound holes are repopulated no radiative recombination can occur. In this way, the Auger life time limits the time scale at which radiative recombination can occur. Thus, figure 2.2 shows the radiative recombination lifetime including the Auger influence.

The emitted fluorescence radiation from the free-bound transitions can be recorded spectrally and is located around the element specific absorption

edge. The spectral shape depends on the population of the participating shells as well as the transition probabilities, which include the dipole selection rules. An exact description of the resulting spectra is a topic of current investigation [71]. However, a simplified model already allows us to qualitatively describe the spectra recorded within our experimental resolution on aluminium (chapter 4.1, [4]). We assume that only 3s to 2p transitions contribute and that all those are equally probable. Figure 2.4 illustrates the process with this assumption. The high energy wing of the fluorescence feature is a Fermi-distribution

$$f(E_{ph}, T_e) = (1 + exp((E_{ph} - E_{Ledge})/T_e))^{-1}, \tag{2.7}$$

with the temperature $T_e$ of the conduction band electrons and the L-edge energy $E_{L-edge}$ (72.5 eV in aluminium [72]). The low energy wing is determined by the density of states in the conduction band. In aluminium the density of states is in good agreement with that of a free electron gas $g(E) \approx \sqrt{E}$, with the Fermi-energy $E_f$ (11.7 eV in aluminium [73]). The spectral distribution is therefore

$$I_{rr}(E_{ph}) \propto E_{ph}^3 f(E_{ph}, T_e) g(E_{ph} - (E_{L-edge} - E_f)), \tag{2.8}$$

where the $E_{ph}^3$ factor originates from the radiation energy density.

We record radiative recombination spectrally to diagnose the free electron temperature of an aluminium plasma via the density of occupied electronic states [4] (chapter 4.1). We narrow the time window of this temperature measurement down to ∼40 fs, as this is the estimated life time of the competing Auger process [66].

### Plasma Line Emission

Radiative bound-bound transitions will occur predominantly when the dense plasma continuum of states breaks up into sharp ionic or atomic levels. For the excitation intensities available at FELs, this occurs when the plasma density drops significantly due to hydrodynamic expansion. Thus, the line emission will originate mostly from the ablated plasma blowoff. Simulations indicate that the expansion will take place on a timescale of ps to ns after excitation (chapters 2.2 and 4.2). At this time the electron and ion temperature have thermally equilibrated via Coulomb collisions (chapter 2.1.2). Thus, the emission intensity ratio $I_1/I_2$ of two bound-bound transitions follows a Boltzmann distribution [5, 74] (chapter 4.2)

$$\frac{I_1}{I_2} = \frac{\omega_1^3}{\omega_2^3} \frac{f_1}{f_2} \mathrm{e}^{-\hbar(\omega_1 - \omega_2)/k_\mathrm{B} T_\mathrm{e}}, \tag{2.9}$$

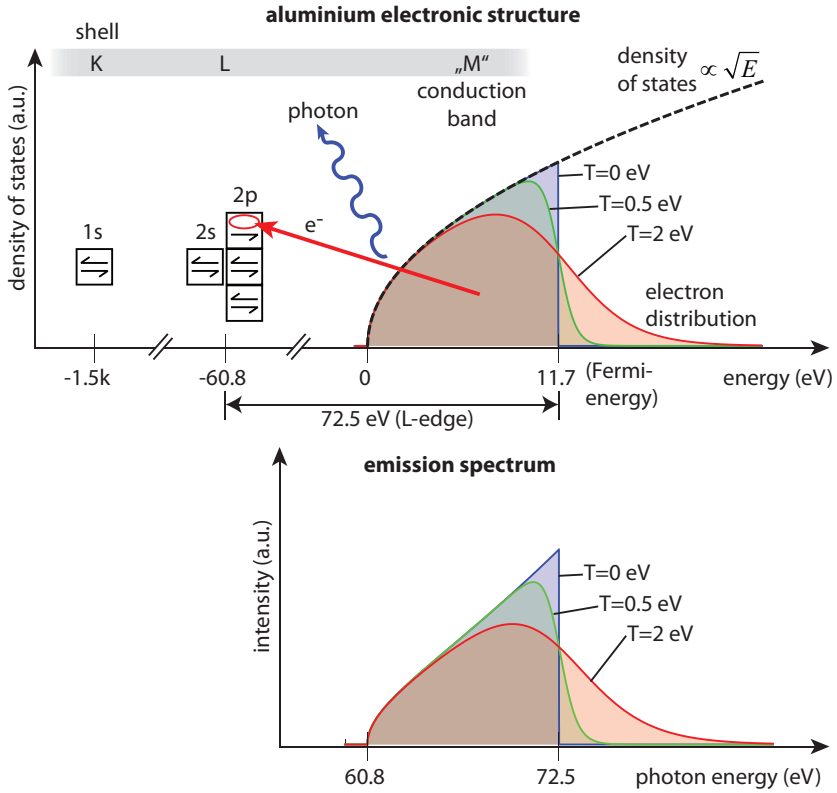


Figure 2.4: Radiative Recombination schematic showing the aluminium electronic structure (top panel) with an electron from the conduction band filling an L-shell hole. The bottom panel shows the emission spectrum resulting from an ensemble of such transitions.

where $\omega$ is the photon angular frequency and $f$ the oscillator strength of the emission line labeled by indices. The temperature of the sample is $T_e$ with the Boltzmann constant $k_B$.

The emission lines can be recorded spectrally and identified from tables. The oscillator strength is also tabulated for many emission lines (e.g. [64, 75]), so that the sample temperature can be measured via equation 2.9. In this work the technique was applied to aluminium plasmas [5] (chapter 4.2).

### 2.1.4 Low Intensity ps Approximation

In the limit of low irradiation intensity, where the target does not undergo significant changes (e.g. thermal ionization, phase transition, change of heat capacity), the target temperature can be estimated using macroscopic quantities. On the time scale of ps the electrons and ions will be thermally equilibrated by collisions (chapter 2.1.2). Due to the low intensity no significant hydrodynamic motion occurs within a ps (chapter 2.2). Also, the temperature increase of the sample will be small, so that radiative losses and heat transport can be neglected during this time. Under these conditions, the Beer-Lambert law can be used to calculate the target depth dependent energy deposition

$$E_{depo}(x) = \frac{E_0}{lA} e^{-x/l}, \tag{2.10}$$

using tabulated penetration depths $l$ [72], the energy in the radiation pulse $E_0$, and the irradiated area $A$. With knowledge of the target mass density $\rho$ and its specific heat capacity $c_V$ we can calculate the temperature change

$$\Delta T(x) = \frac{E_{depo}(x)}{\rho c_V}. \tag{2.11}$$

An example of such a calculation is shown in figure 2.5 for a magnetic multilayer consisting of a membrane with alternating cobalt and platinum layers. This target was irradiated with an energy density of $4\,\mathrm{mJ\ cm^{-2}}$ at a photon energy of 59 eV resulting in an energy deposition below $2\,\mathrm{kJ\,cm^{-3}}$. This is sufficiently low in comparison to the first thermal ionization energy ($68\,\mathrm{kJ\,cm^{-3}}$) and specific melting energy ($4.4\,\mathrm{kJ\,cm^{-3}}$) of cobalt [76], so that the lattice does not undergo significant changes. With this calculation the deterioration threshold for the magnetic properties of the multilayer can be estimated [77].

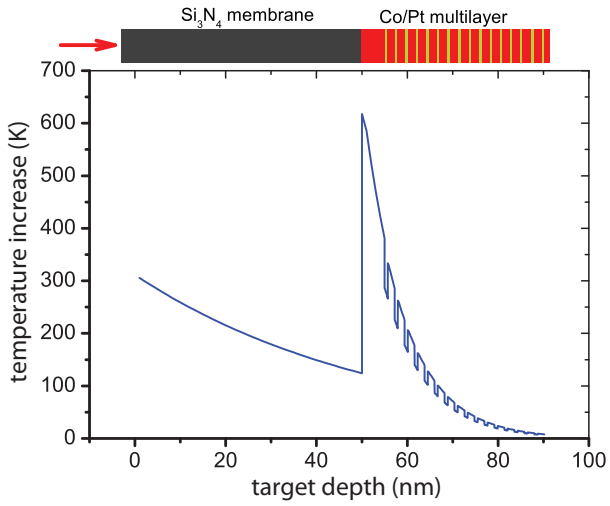


Figure 2.5: Calculated temperature change in a magnetic multilayer ∼1 ps after irradiation by the FEL pulse onto the $Si_3N_4$ membrane.

## 2.2 Helios - Radiative Hydrodynamics Code

At timescales from ps to ns hydrodynamic motion driven by the risen pressure in the ionized hot target can become important. Helios [78] is a commercial simulation code from Prism Computational Sciences™ Inc., that spans the timescales from energy deposition with simplified models to Lagrangian hydrodynamic expansion. It is a 1D radiation-hydrodynamics code. In this work Helios is used to model FEL and optical laser matter interaction. Detailed account of the implemented energy deposition, conservation and transport equations is given in [78]. This section gives an overview of the models used in HELIOS. The last part gives an account of the limitations and applications of these models to WDM laser interaction.

### Energy deposition

Helios was originally designed to model high power long-pulse (ps to ns) visible and infrared laser matter interaction. In this regime the target is ionized within a first fraction of the pulse. The remaining majority of the pulse heats the target via inverse bremsstrahlung. Other heating mechanisms are not modeled. Therefore, the target state after irradiation hardly depends on the initial ionization mechanism. Helios takes this into account by assuming a preionized target and neglecting ionization mechanisms. This is further justified in the case of metal targets where the naturally present conduction band electrons can undergo inverse bremsstrahlung. The initial degree of

ionization, i.e. the percentage of electrons that are free, can be user defined. For aluminium targets I set it to 20 %, independently of the laser wavelength. For hydrogen I set it to 20 % when simulating optical laser interaction and to zero when FEL irradiation is considered. In the latter case, the main absorption mechanism is photoionization (chapter 2.1.1), which is modeled by a custom Helios extension. It additionally models the FEL energy deposition via tabulated opacities which are similar to the Henke tables [72, 79]. If the laser impinges on the critical surface it is reflected. Non-linear effects in the absorption process, such as stimulated Brillouin and stimulated Raman scattering [57] are not modeled. The energy deposited via photoionization or inverse bremsstrahlung raises $T_e$ and an equilibration with the ions is modeled via collisional energy transfer (chapter 2.1.2).

### Hydrodynamics

The simulation assumes a Maxwell-Boltzmann energy distribution of the electronic and ionic system at all times, with independent temperatures $T_e$ and $T_i$, respectively. Values for pressure and degree of ionization are looked up in SESAME-like tables [80] using the temperature and density at the particular time and space location.

The 1D hydrodynamic motion is modeled with a Lagrangian grid of cells, i.e. each cell has a constant mass content and its boundaries co-move with the liquid. The motion of cell boundaries is determined by the pressures in the neighboring cells. The cells can be put together in planar geometry as stacked slabs along the target depth, in cylindrical geometry as concentric cylinders, and as concentric spheres in spherical geometry. Figure 2.6 gives an example of cell boundary motion. The mass in each cell can be user defined to find the best compromise between calculation time and accuracy. The time steps in the simulation are automatically refined within user defined limits, so that e.g. the electron temperature change per time step does not overcome an upper limit.

### Heat Transport

Due to the spatial extent of the target, modeling heat transport is also necessary. The main transport mechanisms are radiative and electronic, of which both are applied in Helios [78]. The latter is modeled via the Spitzer-Härm heat conductivity [57, 81] which is based on the electron mobility limited by electron ion collisions. The heat conductivity $\kappa$ then follows $\kappa \propto T_e^{5/2} Z^{-1} \Lambda^{-1}$, where $T_e$ is the local electron temperature, $Z$ the average degree of ionization, and $\Lambda$ the Coulomb logarithm (section 2.1.2, page 14). This is a good

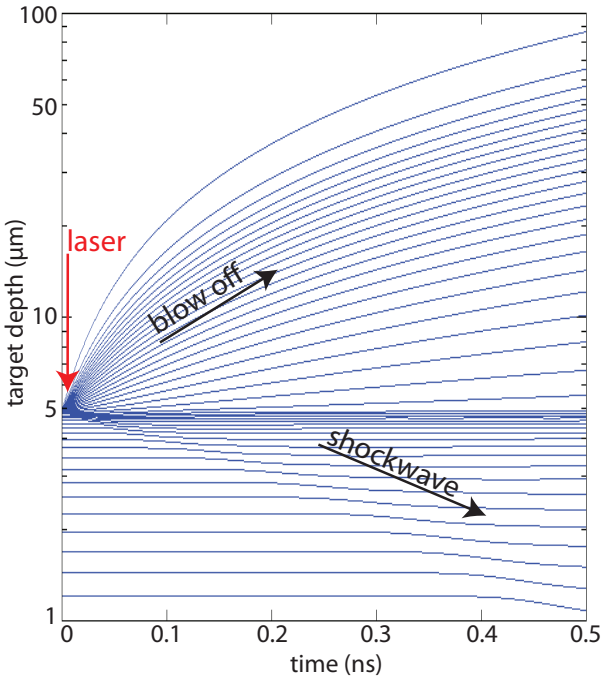


Figure 2.6: Logarithmic plot of the cell boundaries, marked by lines in a simulation of aluminium irradiated by 92 eV photons with an intensity of $10.2\,\mathrm{J\,cm^{-2}}$ and a pulse duration of 30 fs. Initially, the target extends from 0 to 5 $\mu$m.

approximation for high temperature plasmas with gentle temperature gradients. However, it fails at low temperatures and strong gradients as the electrons cannot carry more energy than $n_e T_e v_e$, where $n_e$, $T_e$, and $v_e$ are the free electron density, temperature (in eV) and velocity, respectively. This has also been observed experimentally (e.g. [82] and references in [57]). To extend the validity of the Spitzer-Härm approach an artificial flux limiter $f$ is introduced [57], so that the transported energy per time $\kappa\,\partial T_e/\partial x$ does not become greater than $f n_e T_e v_e$, where $x$ is the spatial coordinate. This allows reducing computational time while maintaining a fairly good accuracy for most applications. Experimentally an $f = 0.08 \pm 0.02$ has been observed [83]. I use $f = 0.06$ in the simulations to obtain an estimate for how inhomogeneous a plasma can be expected.

Radiative heat transport is modeled via flux limited diffusion with tabulated opacities and Black body emission [78, 84], equivalently to the flux limited Spitzer-Härm electronic heat transport.

### Limitations and Capability

The most imminent limitations of the Helios code originate from the models which simplify the actual physical processes for the sake of computational time. The assumption of a Maxwell-Boltzmann electronic energy distribution

obviously breaks down in the case of x-ray photoionization at fs time scales. Thus, the simulation results are incorrect on this time scale. However, the amount of deposited energy is modeled correctly so that sample temperature and density predictions should agree better with reality once the plasma components follow a Maxwell-Boltzmann distribution. This occurs on the fs time scale for the electronic system. The ion-electron equilibration takes ps (chapter 2.1.2).

At radiation intensities above $\sim 10^{15}\,\mathrm{W\,cm^{-2}}$ we observe a reduction of absorption in the experiment (chapter 4.1, page 84, [4]). This is not modeled in Helios' tabulated opacities and, therefore, the amount of deposited energy will be overestimated in the simulation. For our experimental conditions the deviation is up to a factor of three. Yet, most FEL experiments are situated below this critical intensity.

Our spectroscopic temperature measurements on aluminium irradiated with an average intensity of $2 \times 10^{14}\,\mathrm{W\,cm^{-2}}$ show qualitative agreement with the evolution of the plasma (chapter 4.2, page 92, [5]). However, the temperature in the simulation deviates about 35% from the spectroscopic measurement. A possible explanation is that the experiment integrates over many FEL exposures with varying irradiation intensity. Thus, the created plasma conditions vary. Furthermore, denser plasmas will contribute stronger to the temporally integrated spectrum. Therefore, a direct comparison of a time integrated experiment with a single Helios simulation using an average FEL intensity has limited validity. A possible future approach could be to run a Helios simulation with an effective irradiation intensity which is the weighted average of the individual pulse intensities in the experiment. The weighting factors account for the dependance of irradiation intensity on the plasma emission intensity. However, a direct comparison with single pulse experimental data will allow a better estimate of Helios' accuracy.

Optical or infrared radiation at high intensity ($> 10^{14} W\,cm^{-2}$) can also lead to non-thermal electron distributions, e.g. in the form of hot electron production [85, 86]. These cause an increased and non local electronic heat transport as well as an increased photoabsorption at the critical surface. Since Helios does not model this interaction unnaturally strong gradients and an underestimate of the deposited energy occurs. Equally important for optically generated plasmas, non local radiation transport is not modeled but occurs naturally when the plasma gradient length scale becomes smaller than the photon mean free path [84]. Furthermore, non-linear absorption mechanisms such as stimulated Brillouin and stimulated Raman scattering [57] are not modeled. They are important for long wavelengths (optical or infrared) radiation at high intensities. In this regime, only qualitatively correct results can be expected from Helios.

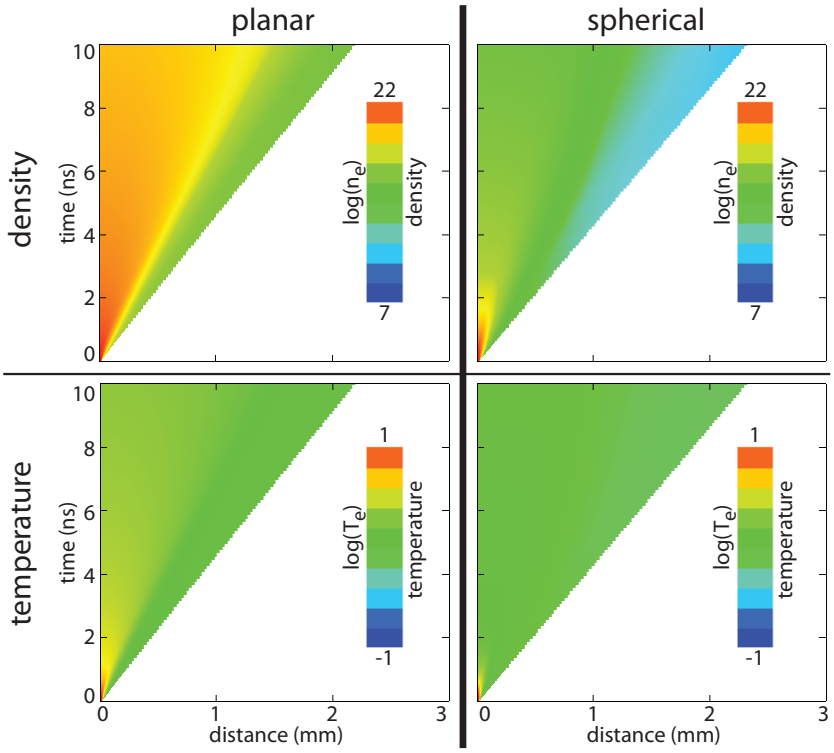


Figure 2.7: Comparison of Helios simulations in planar and spherical geometry with a 10 eV freely expanding hydrogen plasma at initially liquid density ($0.071\,\mathrm{g\,cm^{-3}}$). For planar geometry only the part expanding to positive coordinates is shown and the sample has an initial thickness of $20\,\mu$m. The spherical sample has an initial radius of $10\,\mu$m.

In some cases also the 1D model system is insufficient to represent reality. For example in the case of a droplet target irradiated from one side, a strong gradient not only radially but also along the irradiation axis is expected. This would better be simulated in 2D cylindrical geometry or even full 3D if laser polarization can be taken into account. Also, the hydrodynamic expansion of the target is influenced by the choice of e.g. spherical or planar target geometry (figure 2.7). Due to the geometry expanding spherical targets loose density faster than planar targets, whereas the speed of the removed material (blowoff) is almost equal in both cases.

Despite these shortcomings Helios delivers results in good quantitative agreement with experiments (e.g. [34, 52]), when it comes to long pulse (ps to ns) optical laser driven shock waves. Qualitative agreement has also been observed with x-ray heated targets and time scales $> 100\,$fs [5] (chapter 4.2,

page 92, [5]). For this work, Helios has proven a powerful tool to estimate target conditions for preparation or analysis of an experiment.

## 2.3 Soft X-Ray Thomson Scattering

### 2.3.1 Overview

Scattering of radiation can be used as a powerful tool to study the composition of matter. For example Brillouin, Bragg and Raman scattering have been used to determine the properties of anorganic as well as biological samples (e.g. [87–89]). Huge facilities such as Diamond in the UK, ESRF in France, and Petra III provide the necessary radiation and are prominent examples of this approach. To perturb the sample as little as possible one usually chooses radiation for which the material is transparent. Novel FELs such as FLASH, the future European XFEL in Hamburg as well as LCLS in the USA additionally enable the investigation of ultrashort timescales and the study of samples via coherent x-ray scattering (e.g. [90, 91]).

In the context of scattering by the free or quasi free electrons of a plasma, one speaks of Thomson scattering (TS), honoring the discovery of the electron by J.J. Thomson in 1897 [92]. TS was first used in the early 1960s to study the incoherent scattering of radio waves from various plasma layers of earth's ionosphere [48, 93]. Thomson scattering with visible or near visible light was used to diagnose theta- and z-pinch as well as magnetically confined plasmas [94, 95], where the plasma temperature and density could be measured. These plasmas had low enough free electron densities so that optical photons could penetrate and hence probe the plasma. To probe high density plasmas, in particular WDM, high photon energies, typically in the x-ray regime, have to be used in order to penetrate the plasma critical surface (figure 1.3, page 9). Furthermore, the duration of the probe radiation needs to be shorter than the life time of the dense plasma, which is in the ps to ns scale. Only in 2000 the first experiment using x-ray probe radiation on a dense plasma was successfully conducted by Riley et al. [49]. The x-ray probe radiation was emitted by a titanium plasma which was generated through optical laser irradiation. In the meanwhile, Thomson scattering has become a standard tool to probe plasmas and in particular their free electron density, free electron temperature and degree of ionization [22, 34, 50–52, 96]. This work transfers the Thomson scattering plasma diagnostic to FELs and in particular the soft x-ray free electron laser in Hamburg (FLASH). The fs duration of its light pulses allows us to achieve an ultrafast temporal resolution for the investigation of equilibration dynamics in the plasma.

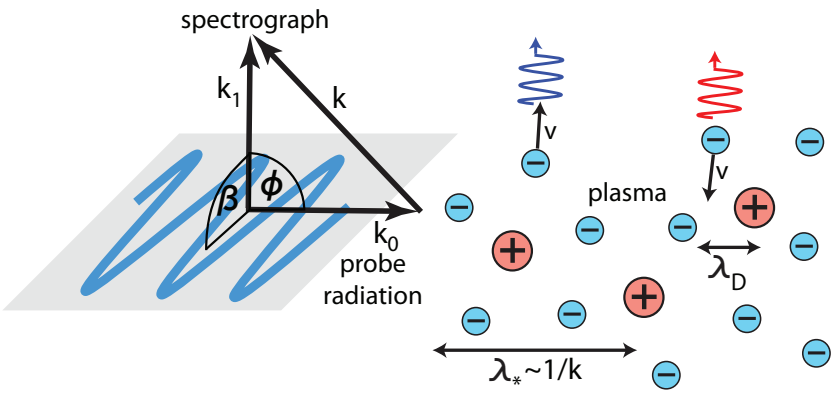


Figure 2.8: Thomson scattering geometry with linearly polarized probe light with incident ($k_0$), scattered ($k_1$) and differential ($k$) wave vectors (left), and sketch illustrating the microscopic length scale in the plasma, where $v$ is the electron velocity, $\lambda_D$ the Debye length, and $\lambda_*$ the probed length scale (right). See text for description.

This section gives an overview of the most relevant relations for non-relativistic Thomson scattering by collisionless plasmas and samples transparent to the probe radiation. During a scattering process, the momentum $\hbar k$ and the energy

$$\hbar\omega = \hbar^2 k^2 / 2m_e = \hbar\left(\omega_0 - \omega_1\right) \tag{2.12}$$

is transferred from the photons to the sample electrons, where $\omega_0$ is the incident and $\omega_1$ the scattered frequency. With the geometry in figure 2.8 and small $\omega = \omega_0 - \omega_1$ we obtain

$$\mathbf{k} = \mathbf{k_1} - \mathbf{k_0}, \tag{2.13}$$

$$k = |\mathbf{k}| = 2k_0 \sin\left(\phi/2\right), \tag{2.14}$$

where $k_0$ is the incident wave number and $\phi$ the scattering angle.

One distinguishes collective and non-collective Thomson scattering by comparing the length scale $\lambda_* \approx 1/k$ that is probed to the screening length $\lambda_D$ (Debye length, equation 1.6, page 8) [22, 97] using the dimensionless scattering parameter

$$\alpha = \frac{1}{k\lambda_D}. \tag{2.15}$$

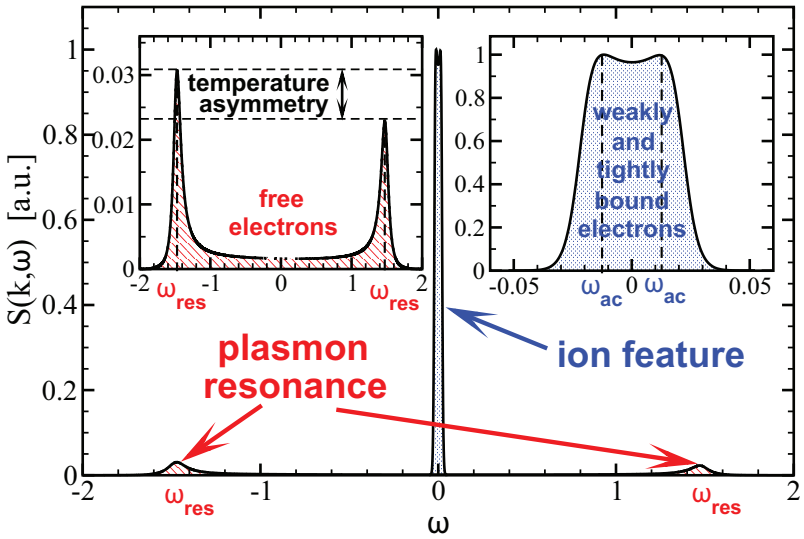


Figure 2.9: Simulated collective ($\alpha > 1$) Thomson scattering spectrum illustrating the measurement of free electron temperature and density via detailed balance and plasmon dispersion, as well as the ion acoustic modes (ionic plasmons) which are typically not resolved in WDM experiments (from [13]).

If $\alpha < 1$ than the scattering is non-collective yielding an elastic scattering spectrum which is Doppler broadened by the electron thermal velocity. For $\alpha > 1$ collective electron motion is observed (figure 2.9) and the electron temperature and density can be measured. Figure 1.2 (page 4) depicts the dependance of the scattering parameter on free electron density and temperature.

This work concentrates on collective Thomson scattering where the scattering signal consists of an elastic part and blue and red shifted contributions which are inelastically scattered by electronic plasma waves, plasmons. Here, the free electron temperature $T_e$ can be determined via the detailed balance relation [22]

$$\frac{S\left(k,\omega\right)}{S\left(-k,-\omega\right)} = e^{-\hbar\omega/k_B T_e}, \tag{2.16}$$

where $S\left(-k,-\omega\right)$ and $S\left(k,\omega\right)$ are proportional to the red and blue shifted plasmons, respectively. The dynamic structure factor $S(k,\omega)$ describes multiparticle effects in the scattering process and will be discussed in greater detail in the next section. Equation 2.16 can be applied when the electronic system

follows a Fermi or classical Maxwell-Boltzmann distribution and a directed flow of the plasma is negligible on the time scale of the probe pulse.

The free electron density in the plasma is determined by the spectral shift of the plasmons with respect to the elastically scattered light. This relation can be approximated by the Bohm-Gross dispersion [8, 98, 99]

$$\omega_{res}^2(k) \approx \omega_{pe}^2 + \frac{3k_B T_e}{m_e} k^2, \tag{2.17}$$

in the non-relativistic regime with small momentum transfers $\hbar k$, small photon energies $\hbar\omega$ and for weakly coupled plasmas with the plasma frequency $\omega_{pe}$ (equation 1.7, page 8). It describes the dispersion of purely electrostatic electron density waves, so called Langmuir waves [100]. In the case of a hydrogen plasma, the relationship (equation 2.17) holds well up to a free electron density of $\sim 5 \times 10^{20}\,\mathrm{cm}^{-3}$ and $\sim 15\,\mathrm{eV}$ temperature. Beyond this, more sophisticated models need to be applied to obtain the plasmon dispersion relation [8]. However, for soft x-ray radiation and the hydrogen plasma densities of this work, equation 2.17 is a valid approximation. This has been shown by comparing scattering codes using more sophisticated models (chapter 2.3.2) with equation 2.17.

The power of collective Thomson scattering lies in its ability to determine the main plasma parameter $n_e$ and $T_e$ by recording the scattered spectrum of a probe pulse and utilizing equations 2.16 and 2.17. In particular, the detailed balance relation (equation 2.16) only relies on the electronic system following a Fermi or classical Maxwell-Boltzmann distribution.

### 2.3.2 The Dynamic Structure Factor

#### Basic Electromagnetics

The following section outlines the treatment of light scattering in plasmas. A central quantity in this formalism is the dynamic structure factor (DSF). It is derived from basic electromagnetics by Evans and Katzenstein [48], for a fully ionized plasma and small photon electron momentum transfers. The latter condition is justified for soft x-ray radiation where Compton scattering is negligible (see chapter 2.1.1). The assumption of full ionization does not hold for the Thomson scattering experiments of this work. However, the modifications in hydrogen are minor and the results obtained with this simplification are still valid for our experimental parameters. Generalizations will also be introduced further on. For the derivation, one examines the single electron scattering of an electromagnetic wave with angular frequency $\omega_0$

to a detector and then sums over all electrons in the sampled plasma. This yields the power spectrum at the detector

$$I(\mathbf{k},\omega)\,d\omega d\Omega = NI_0\sigma(\mathbf{k},\omega)\,d\omega d\Omega, \tag{2.18}$$

with the wave vector difference $\mathbf{k}$ from equation 2.14, the incident power $I_0$, and the solid angle $\Omega$. The total scattering cross section is composed as

$$\sigma(\mathbf{k},\omega) = \sigma_T S(\mathbf{k},\omega), \tag{2.19}$$

where $\sigma_T = e^4(m_e c^2)^{-2}\sin^2\beta$ is the scattering cross section of an individual electron, the so called Thomson cross section . The angle between the polarization axis of the incident light and the detector is $\beta$. The dynamic structure factor (DSF) $S(k,\omega)$ accounts for multi particle effects and is given by

$$S(\mathbf{k},\omega) = \frac{1}{2\pi N}\int_{-\infty}^{+\infty} d\tau e^{i(\omega)\tau}\left\langle n(\mathbf{k},t)\,n^*(k,t+\tau)\right\rangle, \tag{2.20}$$

where $\langle..\rangle$ denotes the ensemble average and $n(k,t)$ is the Fourier transform of the electron density fluctuation

$$n(\mathbf{r},t) = \sum_{j=1}^{N}\delta(\mathbf{r}-\mathbf{r}_j(t)), \tag{2.21}$$

$$n(\mathbf{k},t) = \sum_{j=1}^{N} e^{i\mathbf{k}\cdot\mathbf{r}_j(t)}. \tag{2.22}$$

So, the DSF contains the temporal autocorrelation function of the electron density fluctuations. It connects observable scattering spectra determined by the DSF to microscopic multi-particle properties allowing us to measure basic parameters and also test our understanding of plasmas. The measurable parameters include plasma temperature and density.

In the course of this derivation [48], one finds that the scattered spectrum in the limit $\alpha \to 0$ is Doppler broadened by the electron velocity parallel to $\mathbf{k}$. This is the non-collective Thomson scattering regime. More qualitative results can be obtained assuming a collisionless plasma where the species follow a Fermi or Maxwell-Boltzmann distribution with possibly different temperatures. Under these circumstances, TS probes the electron velocity distribution parallel to $\mathbf{k}$ and the frequency integrated total scattering cross section $\sigma_T S(k)$ shows the following behavior for extreme conditions of $\alpha$ [48]:

$$\lim_{\alpha\to 0} \sigma_T S(k) = \sigma_T, \tag{2.23}$$

$$\lim_{\alpha\to \infty} \sigma_T S(k) = \frac{Z\sigma_T}{1+ZT_e/T_i} \overset{\substack{Z=1\\ T_e=T_i}}{=} \frac{1}{2}\sigma_T, \tag{2.24}$$

where $Z$ is the atomic number, and $T_e$ and $T_i$ the electron and ion temperature, respectively. For $\alpha \gg 1$ the scattering spectrum consists of two Lorentzians, the plasmons, peaking at $\pm\omega_{res}$ from the probing frequency, where $\omega_{res}$ follows the Bohm-Gross dispersion relation (equation 2.17).

Further, one can connect equation 2.20 to the macroscopic dielectric coefficient $\epsilon$ via the fluctuation dissipation theorem [101]. Generalizing to a not fully ionized plasma, but assuming a thermalized system with possibly different ion and electron temperature one obtains [22]

$$S(\mathbf{k},\omega) = \frac{\varepsilon_0 \hbar k^2}{\pi e^2 n_e} \frac{1}{1-e^{\hbar\omega/k_B T_e}} \operatorname{Im}\varepsilon^{-1}(\mathbf{k},\omega). \tag{2.25}$$

Detailed balance (equation 2.16) is a direct consequence of this equation and not dependent on $\alpha$, $\epsilon$ or the treatment of collisions.

### Composition for Soft X-Rays

Chihara showed that the DSF can generally be decomposed into bound, free and bound-free electronic contributions [8, 13, 102, 103] leading to the expression

$$\begin{aligned} S(k,\omega) = Z_f S^0_{ee}(k,\omega) + |f_I(k) + q(k)|^2 S_{ii}(k,\omega) \\ + Z_b \int d\omega' \tilde{S}_{ce}(k,\omega-\omega') S_S(k,\omega'), \end{aligned} \tag{2.26}$$

where the first term describes the response of the free electrons with the average number of free electrons per atom $Z_f$. The second term contains the ion form factor $f_I(k)$ representing the bound electrons, the free electrons in the screening cloud of the ion $q(k)$, and the ion structure factor $S_{ii}(k,\omega)$. The third term is due to inelastic bound-free transitions of core electrons ($\tilde{S}_{ce}(k,\omega-\omega')$), which are modulated by the ion motion ($S_S(k,\omega')$), with the binding energy $\hbar\omega'$. Depending on the relevant wavelength range and for the purpose of calculating the DSF it can be practical to decompose $S(k,\omega)$ in different ways.

In the soft x-ray regime the momentum transfer from the photons to the electrons is small in comparison to the binding energy of the electrons, so

that the last term in equation 2.26 is negligible [13]. In the same limit the size of the probed structures is in the nm regime and thus large in comparison to the atomic structure. Considering this, $|f_I(k) + q(k)| \rightarrow Z = Z_b + Z_f$ so that equation 2.26 can be written for soft x-rays as

$$S(k,\omega) = Z_f S^0_{ee}(k,\omega) + Z^2 S_{ii}(k,\omega). \tag{2.27}$$

Another representation of the DSF for soft x-rays is given by Höll et al. [13]. As the probed structures are larger than the size of an ion, the "frozen core" approximation is justified. That is, the screening cloud and free electrons are combined to $S'_{ee}$ and the bound electrons are represented by $S'_{ii}$, yielding

$$S(k,\omega) = Z_f S'_{ee}(k,\omega) + Z_b^2 S'_{ii}(k,\omega) + 2Z_b\sqrt{Z_f} S'_{ei}(k,\omega), \tag{2.28}$$

with the bound-free correlation term $S'_{ei}(k,\omega)$. The last term hardly affects the total $S(k,\omega)$ for the experimental conditions considered here. In fact, it generates a small dip between the elastic scattering signal [104] and the plasmons, which is typically washed out by the detector resolution. Thus, for practical purposes equation 2.28 can be simplified to

$$S(k,\omega) = Z_f S'_{ee}(k,\omega) + Z_b^2 S'_{ii}(k,\omega). \tag{2.29}$$

Equations 2.27, 2.28, and 2.29 are different approximations of equation 2.26 for the soft x-ray regime. These approximations are all in agreement within the accuracy of experiments described here. Depending on the method to calculate the components of the DSF, a particular representation can be more practical.

### Cold Ions and the Debye-Waller Factor

The scattering of radiation by bound and screening cloud electrons is strongly influenced by the relative location of the ions, represented by $S_{ii}(k,\omega)$ in equation 2.27. The spatial correlation of the ions is contained in the frequency integrated ionic structure factor $S_{ii}(k)$ and is observable in the scattering spectrum as Bragg peaks for different $k$. The random thermal motion of the ions reduces the correlation between them and, thus, reduces the intensity of the Bragg peaks. At the same time the thermal ion motion causes the diffuse scattering of radiation, i.e. scattering at $k$ away from the Bragg peak. This is the well known Debye-Waller-Effect [105]. It also applies to plasmas which was shown theoretically [48, 106] and experimentally [6, 107] (chapter 4.3). Particularly interesting for the Thomson scattering experiments of this work

[6] (chapter 4.3) is the strong reduction of elastic scattering at small ion temperatures $T_i$ and at $k$ away from the Bragg peak (diffuse scattering). The reduced elastic scattering intensity can be accounted for by the diffuse Debye-Waller factor $\left(1 - e^{-2W}\right)$ which modulates $S_{ii}$ from equation 2.27 calculated without collisions. One obtains

$$S\left(k,\omega\right) = Z_f S^0_{ee}\left(k,\omega\right) + Z^2\left(1 - e^{-2W}\right) S_{ii}\left(k,\omega\right), \tag{2.30}$$

where $\left(1 - e^{-2W}\right) \simeq 2W$ and

$$2W = \frac{\pi^2 k^2 \hbar^2}{4 M k_B T_D}\left(\frac{T_i}{T_D}\right)^2, \tag{2.31}$$

with the ion mass $M$. The Debye temperature $T_D$ [106, 108] can be estimated using the Bohm-Staver relation [106, 109], in practical units

$$\begin{aligned}\frac{T_D}{\mathrm{eV}} = 8.38 \times 10^{-13}&\left(\left(\frac{Z_f}{1}\right)\left(\frac{\mathrm{u}}{m_i}\right)\left(\frac{n_e}{\mathrm{cm^{-3}}}\right)\right)^{1/2} \times \\ &\left[1 + \left(1.14589 \times 10^{-22}\left(\frac{n_e}{\mathrm{cm^{-3}}}\right)\left(\frac{\lambda}{\mathrm{nm}}\right)^2 \sin^{-2}\phi\right) \times \right. \\ &\left.\left(\left(\frac{T_e}{\mathrm{eV}}\right) + \frac{1.33 \times 10^{-29}\left(\frac{n_e}{\mathrm{cm^{-3}}}\right)^{4/3}}{\left(1.3251 - 282105\left(\frac{n_e}{\mathrm{cm^{-3}}}\right)^{1/6}\right)^2}\right)^{-1/2}\right]^{-1/2},\end{aligned} \tag{2.32}$$

where $m_i$ is the ion mass in proton masses u, $\lambda$ the probe wavelength, and $\phi$ the scattering angle. This $T_D$ can be used for example as an input to the scattering code by Gregori et al. [106, 110–112] to calculate the Thomson scattering spectrum of a plasma with $T_i < T_e$. It was applied in chapter 4.3.

For the Thomson scattering experiment [6] (chapter 4.3) we estimate a $k_B T_D = 10\,\mathrm{meV}$ using equation 2.32. From scattering simulations using the code by Gregori et al. we see that the elastic scattering is not observable for ion temperatures below 0.1 eV. In the experiment we excite a cryogenic sample on the fs timescales, where the ions are hardly heated. We do not observe elastic scattering and with the simulation this gives us an upper limit for the sample's ion temperature $T_i < 0.1\,\mathrm{eV}$. At the same time we measure via the plasmons a free electron temperature of 13 eV. Therefore, we observe a non-equilibrium plasma [6] (chapter 4.3).

### Calculation of the Dynamic Structure Factor

To calculate the DSF one typically uses a convenient decomposition of $S(k,\omega)$ and thus splits the problem into calculating the different contributions to $S(k,\omega)$. Those contributions relate to different parts of the dielectric constant $\epsilon$ or of the electron density response function $\chi_{ee}^{tot} \propto 1/\epsilon$ via the fluctuation dissipation theorem [101]. Ideal and collisionless plasmas have been studied thoroughly in the last decades [48, 113–115]. Their DSF can be calculated assuming that the local electric potential in the plasma averages to zero due to the random phase of fluctuations, so that only the probing electromagnetic wave contributes. This is called the random phase approximation (RPA) [8, 110]. At free electron densities above approximately $n_e > 5 \times 10^{20}\,\mathrm{cm}^{-3}$, higher than the densities reached in this work, particle collisions inhibit the free oscillations of the plasma electrons. This affects the DSF and RPA is no longer valid. The calculation of the DSF and the underlying models in this regime are a topic of current investigation [1, 8]. However, the plasmas of this work are well described within RPA.

In the course of this work I have used three programs that are capable of synthesizing scattering spectra. They are useful to predict experimental data in the planing stage and to analyze the data after the experiment. Furthermore, microscopic models included in the codes can be tested by comparing their prediction with the experiment. At the current state of research this is particularly interesting for ionic correlations $S_{ii}(k,\omega)$ (e.g. [116]) and their relative intensity to $S_{ee}(k,\omega)$. One code to generate Thomson scattering spectra is from Fortmann, Thiele, et al. [117, 118] and another one from Gregori et al. [106, 110–112]. Both codes are capable of calculating the DSF in RPA. They also include various other approximations and in particular the latter includes the Debye-Waller effect.

Furthermore, in collaboration with Thiele and Fortmann I have generated an RPA based Matlab code to fit the data from Thomson scattering measurements in Hydrogen (chapter 4.3). I also used this code to batch process density and temperature profiles of inhomogeneous samples generating more realistic total scattering spectra (see also chapter 2.4).

### Scattering Regimes

Finally, we classify Thomson scattering within a larger scope of scattering regimes in order to see where the above treatment is applicable. Figure 2.10 shows various $k$ regimes. In the long wavelength limit (hydrodynamic limit, $k \to 0$) using optical or microwave radiation, the scattering spectrum typically shows an elastic Rayleigh peak from a non propagating lattice mode as

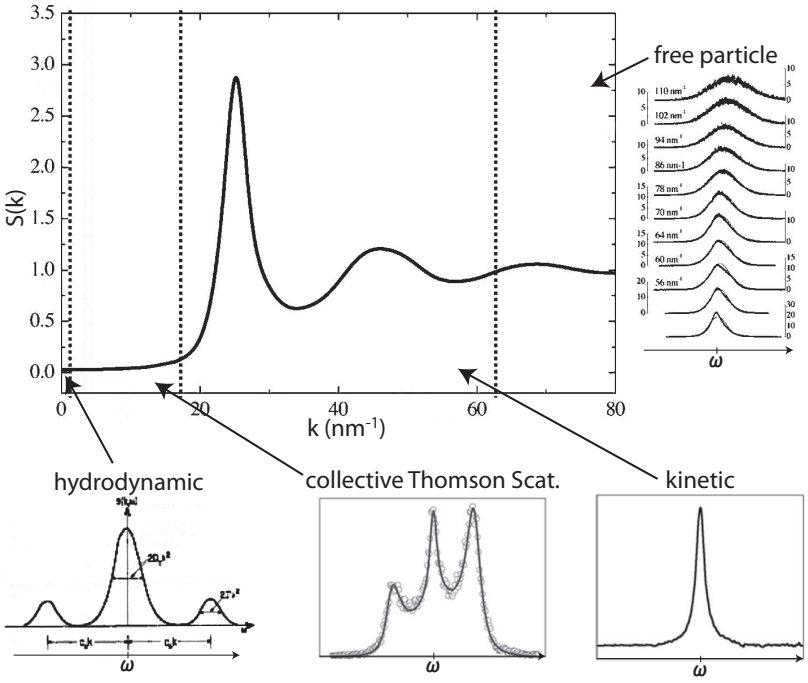


Figure 2.10: Sketch of the frequency integrated DSF $S(k)$ for a dense plasma and frequency dependent DSF for various k-regimes (inserts). Based on [14].

well as an inelastic Brillouin doublet red and blue shifted by $kc_s$, with the sound speed $c_s$, and dampened by viscous and thermal effects. This regime can be investigated using optical Brillouin scattering if the material is sufficiently transparent [14]. This is clearly challenging with metals or dense plasmas. Approaching this regime of small $k$ via low angle x-ray scattering is a topic of current research [14, 119].

At larger $k$, typically in the x-ray regime, the frequency integrated spectrum, proportional to $S(k)$, shows resonances (figure 2.10). These correspond to the Fourier transform of the ionic correlation lengths in the sample. The sample's state of matter (solid, liquid, gas) and its crystal structure mainly determines how pronounced these features are. They are for example visible in x-ray diffraction. This is called the kinetic regime (figure 2.10) and the $k$ dependent variation of $S(k)$ is mainly due to $S_{ii}$ which dominates the spectrum here [14, 48]. In this work, we use Thomson scattering of 13.5 nm radiation under 90° resulting in a probed length scale of $\lambda_* \approx 10\,\mathrm{nm}$. This is substantially larger than the average atomic distance of $(3/(4\pi n))^{1/3} \approx 0.2\,\mathrm{nm}$ in the liquid hydrogen sample of atomic density $n = 4 \times 10^{22}\,\mathrm{cm}^{-3}$. There-

fore, such resonances are not visible in the Thomson scattering experiment described here (chapter 4.3). However, collective electron effects are visible in the scattering spectrum as described in the previous sections.

In the limit of $k \rightarrow \infty$ single particle motion is probed. This is the non-collective Thomson scattering regime. Note that the detailed balance relationship (equation 2.16) is still valid in this regime.

## 2.4 Thomson scattering in dense plasmas with density and temperature gradients [1]

*In the following publication we apply the Thomson scattering code (chapter 2.3, page 26) on Helios radiative hydrodynamic simulations (chapter 2.2, page 21) to investigate the impact of FEL generated density and temperature inhomogeneities on the scattering spectrum. Thus, we study the reliability of Thomson scattering measurements at FELs which is a prerequisite for the analysis of experiments [6] (chapter 4.3, page 103) and combines methods discussed in previous sections.*

**Abstract**

Collective X-ray Thomson scattering has become a versatile tool for the diagnostics of dense plasmas. Assuming homogeneous density and temperature throughout the target sample, these parameters can be determined directly from the plasmon dispersion and the ratio of plasmon amplitudes via detailed balance. In inhomogeneous media, the scattering signal is an average of the density and temperature dependent scattering cross-section weighted with the density and temperature profiles. We analyse Thomson scattering spectra in the XUV range from near solid density hydrogen targets generated by free electron laser radiation. The influence of plasma inhomogeneities on the scattering spectrum is investigated by comparing density and temperature averaged scattering signals to calculations assuming homogeneous targets. We find discrepancies larger than 10% between the mean electron density and the effective density as well as between the mean temperature and the effective temperature.

### Introduction

Recently, X-ray Thomson scattering has been demonstrated to be a reliable and versatile tool for the diagnostics of dense plasmas [22]. Examples for applications cover a large range from laser produced plasmas at temperatures of several keV and densities between solid density and a few percent of solid density (hot dense plasmas) [111, 120] from so-called warm dense matter (WDM) [121, 122] with temperatures of several eV and densities close to solid density [50, 51], up to compressed matter at temperatures between 0.1 eV and several 10 eV [123, 124].

[1] Peer reviewed paper. This section has been published as: C. Fortmann, R. Thiele, R.R. Fäustlin et al., High Energy Density Physics [1] © 2009 Elsevier B.V.

The determination of the plasma properties, such as the plasma density, the plasma temperature, and the plasma composition, requires knowledge of the density and temperature dependent scattering cross-section. As will be outlined in Sec. 2.4, the cross-section for Thomson scattering is usually expressed via the dynamical structure factor (DSF) $S_{\mathrm{ee}}(\mathbf{k},\omega)$ [103], which is a function of the scattering wavevector $\mathbf{k}$ and the frequency shift $\omega$, convoluted with the density and temperature distribution of the target. In this way, plasma inhomogeneities can be taken into account in the simulation of the scattering spectrum, which is the main purpose of this paper. Such analysis was performed earlier by Baldis et al. [125] for the case of VUV photons interacting with solid aluminum targets. Here, the scenario of XUV photons delivered by the free electron laser facility at DESY-Hamburg (FLASH) [15] scattering on solid hydrogen (mass density $\rho = 0.088\,\mathrm{g/cm^3}$) as proposed by Höll et al. [13], will be considered.

**Theory of Thomson scattering and the dynamic structure factor**

The scattered power per solid angle $d\Omega = \sin\vartheta\, d\vartheta\, d\varphi$ and unit frequency interval $d\omega$ is given by the expression [125]

$$\frac{d^2P_{\mathrm{sc}}}{d\Omega\, d\omega} = \frac{\sigma_{\mathrm{T}}}{A_{\mathrm{rad}}}\frac{k_{\mathrm{f}}}{k_{\mathrm{i}}}\int_{-\infty}^{\infty}\frac{d\omega'}{2\pi}G_{\Delta\omega}(\omega-\omega')\times\int_{\mathcal{V}_{\mathrm{rad}}}d^3\mathbf{r}\, I(\mathbf{r})\, S_{\mathrm{ee}}(\mathbf{k},\omega';n_{\mathrm{e}}(\mathbf{r}),T(\mathbf{r}))\, n_{\mathrm{i}}(\mathbf{r})\ . \tag{2.33}$$

$\sigma_{\mathrm{T}} = 6.65\times10^{-24}\,\mathrm{cm^2}$ is the Thomson cross-section, $\mathbf{k}_{\mathrm{i}}$ and $\mathbf{k}_{\mathrm{f}}$ are the initial and the final photon wavevector, respectively. By $\mathbf{k} = \mathbf{k}_{\mathrm{i}} - \mathbf{k}_{\mathrm{f}}$, we denote the scattering wavevector. From the conservation of momentum, we obtain $k = 4\pi\sin(\vartheta/2)/\lambda_0$, with $\lambda_0$ being the probe wavelength. $I(\mathbf{r})$ is the $\mathbf{r}$ dependent power density of incoming photons, while $A_{\mathrm{rad}}$ is the radiated surface of the target. Using the convolution of the DSF with an appropriately chosen instrumental function $G_{\Delta\omega}(\omega)$, the finite resolution of the spectrometer as well as the probe's bandwidth is taken into account. Here, we use the normalized Gaussian distribution

$$G_{\Delta\omega}(\omega) = \frac{1}{\sqrt{2\pi}\sigma}\exp\left(-\frac{\omega^2}{2\sigma^2}\right)\ , \tag{2.34}$$

$\Delta\omega = 2\sqrt{2\ln 2}\,\sigma$ is the full width at half maximum (FWHM) of the instrumental function.

Finally, the plasma inhomogeneities are taken into account by averaging the DSF with the electron density profile $n_{\mathrm{e}}(\mathbf{r})$ and the temperature profile $T(\mathbf{r})$.

It is convenient to separate the DSF into contributions from free-free, free-bound and bound-bound correlations as proposed by Chihara [103],

$$\begin{aligned} S_{\mathrm{ee}}(\mathbf{k},\omega) = &\left|f_{\mathrm{i}}(k)+q(k)\right|^2 S_{\mathrm{ii}}(\mathbf{k},\omega) \\ &+ Z_{\mathrm{c}}\int_{-\infty}^{\infty} d\omega'\, S_{\mathrm{c}}(\mathbf{k},\omega) S_{\mathrm{s}}(\mathbf{k},\omega-\omega') \\ &+ Z_{\mathrm{f}} S^0_{\mathrm{ee}}(\mathbf{k},\omega). \end{aligned} \tag{2.35}$$

The first part gives the correlation of electrons that are weakly and tightly bound to the ions and follow the ion's movement adiabatically. The amplitude is determined by the atomic form factor $f_{\mathrm{i}}(k)$, i.e. the charge distribution of the electrons in the valence shell orbitals and the screening cloud $q(k)$ which gives the distribution of quasi-free electrons screening the ion's charge [112].

The second term contains the contribution of core electrons, $S_{\mathrm{c}}(\mathbf{k},\omega)$ and describes Raman type transitions of inner shell electrons to the continuum, modulated by the ion's movement which is contained in $S_{\mathrm{s}}(\mathbf{k},\omega)$ [126].

Finally, $S^0_{\mathrm{ee}}(\mathbf{k},\omega)$ is the free electron contribution. It determines the behaviour of the total electron structure factor at frequencies close to the plasma frequency. Since we focus on the application of Thomson scattering to diagnostics of dense plasmas via analysis of the plasmon feature, the third term in Eq. (2.35) will be discussed in more detail in the following. This contribution is calculated in the Born-Mermin approximation [118], thereby including collisions among electrons and ions in second order Born approximation. Higher order terms can be treated via the t-matrix and inclusion of dynamical screening, see Ref. [127]. The influence of collisions on the collective scattering spectrum has been thoroughly discussed by some of the authors in Ref. [56]. In this paper, we will concentrate on the impact of the density and temperature profiles on the scattering signal.

### Temperature and density profiles

We consider the interaction of cryogenic ($T \simeq 20\,\mathrm{K}$) hydrogen droplets of about $30\,\mu$m diameter with XUV free electron laser radiation delivered by FLASH at 13.5 nm wavelength with a pulse length of 30 fs and $50\,\mu$J pulse energy. In order to infer the absorption characteristics of the target, we calculate the inverse absorption length $\alpha(\omega)$ of cryogenic hydrogen ($T = 20\,\mathrm{K}$) via ab-initio quantum molecular dynamic simulations using the Kubo-Greenwood formula [128]. The inverse absorption length as a function of the photon energy is shown in Fig. 2.11. At the FLASH energy (92 eV, indicated by the red arrow) the absorption length is $7\,\mu$m, in excellent agreement with tabulated x-ray absorption data [72], which is in the same order of

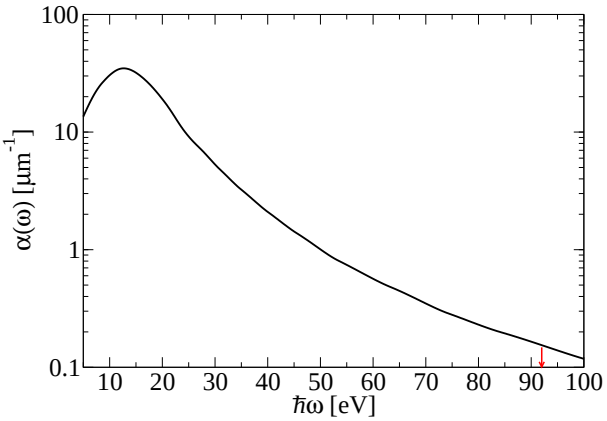


Figure 2.11: Ab-initio simulation of the inverse absorption length for cryogenic hydrogen at solid density as a function of the photon energy. The arrow indicates the FLASH energy (92 eV).

magnitude as the diameter of the hydrogen droplet. Thus, FLASH photons can penetrate deeply into the target.

The interaction of FLASH photons with the hydrogen target was simulated using the radiation-hydrodynamic simulation code HELIOS [78]. HELIOS features a Lagrangian reference frame, separate ion and electron temperatures, and flux-limited Spitzer thermal conductivity. It allows for deposition of laser energy via inverse bremsstrahlung as well as bound-bound and bound-free transitions, using a SESAME-like equation of state.

Figure 2.12 shows the free electron density profile (a) and temperature profile (b) (red solid curves). The density profile decreases exponentially from $n_\mathrm{e} = 2.2 \times 10^{22}\,\mathrm{cm}^{-3}$ at the irradiated surface ($x = 0$) to $n_\mathrm{e} = 1.0 \times 10^{20}\,\mathrm{cm}^{-3}$ at the rear surface ($x = 3.0\,\mu\mathrm{m}$). The 1/e-decay length of the exponential profile is roughly $11\,\mu\mathrm{m}$, which is consistent with the absorption length obtained from the QMD simulation, c.f. Fig. 2.11; the absorption is mainly due to bound-free transitions.

The plasma temperature decreases from $T = 2\,\mathrm{eV}$ to $T = 1.1\,\mathrm{eV}$. For comparison, the dashed lines indicate the mean electron density $\bar{n}_\mathrm{e} = 7.0 \times 10^{21}\,\mathrm{cm}^{-3}$ and mean temperature $\bar{T} = 1.5\,\mathrm{eV}$, respectively.

### Results

In Fig. 2.13, we show calculations of the scattered intensity as a function of the photon energy shift with respect to the FLASH photon energy, assuming FLASH photons scattering from partially ionized hydrogen under an angle of $\vartheta = 90°$. The thin curves show calculations of the scattering spectrum using a single density and temperature combination corresponding to a particular position $x$ in the HELIOS profiles, see Fig. 2.12. Scattering from plasma regions close to the front surface (high density, high temperature) results

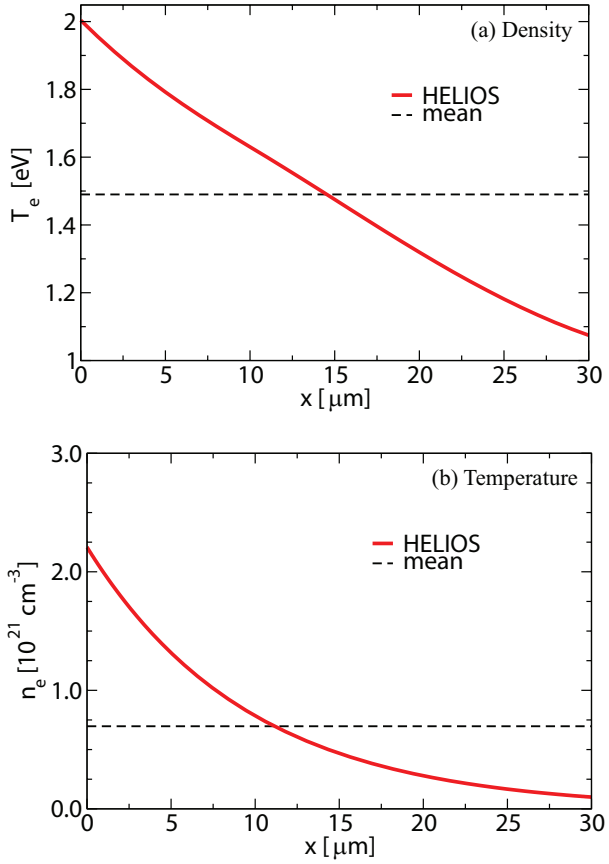


Figure 2.12: Density (a) and temperature (b) profile from HELIOS simulation of liquid hydrogen droplet irradiated by XUV-FEL pulses, $\lambda_0 = 13.5\,\mathrm{nm}$, pulse length 30 fs, pulse energy $50\,\mu\mathrm{J}$ (bold curves). The dashed curves indicate the corresponding mean density and temperature.

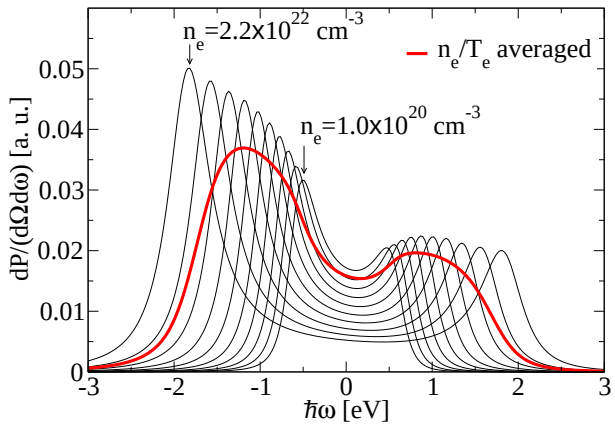


Figure 2.13: Thin curves: Scattered intensity spectra at constant density and temperature corresponding to the HELIOS profiles (Fig. 2.12). Bold curve: Density and temperature averaged scattering spectrum. Scattering angle $\vartheta = 90°$.

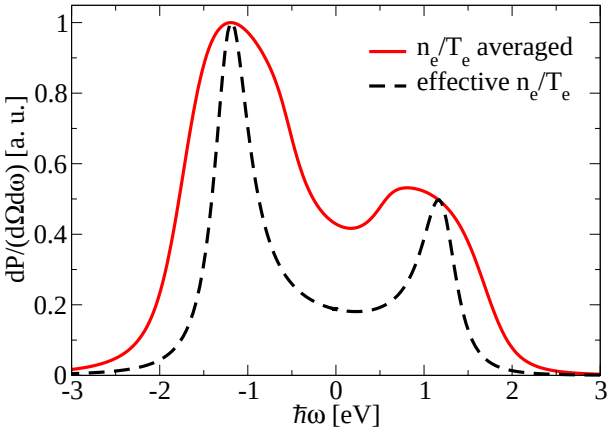


Figure 2.14: Density and temperature averaged scattering spectrum (bold curve) compared to a calculation using the effective density and temperature (dashed curve) obtained from the plasmon peak positions and detailed balance analysis from the profile averaged spectrum. Scattering angle $\vartheta = 90°$.

in a comparatively large plasmon resonance energy, while scattering from the rear surface (low density, low temperature) gives rise to small plasmon energies, as indicated by the arrows and the corresponding electron densities. Finally, the bold curve gives the density and temperature averaged scattered intensity, c.f. Eq. (2.33). Note, that since the DSF is weighted with the local density $n_\mathrm{e}(\mathbf{r})$, i.e. with the number of scattering electrons in the unit volume $d^3\mathbf{r}$, as well as with the number of photons in that volume, regions close to the irradiated surface with increased density contribute more strongly to the spectrum than the dilute parts located towards the rear surface. This results in a scattering spectrum that is significantly more broadened than the original spectra taken at constant density and temperature.

We compare the averaged spectrum to a calculation for the DSF using homogeneous density and temperature distributions. The result is shown in Fig. 2.14. The bold curve is again the DSF averaged with the HELIOS profiles as in Fig. 2.13, the black dashed curve gives the DSF using the effective electron density $n_\mathrm{eff} = 8.3 \times 10^{20} \mathrm{cm}^{-3}$ and effective temperature $T_\mathrm{eff} = 1.7\,\mathrm{eV}$, which are inferred from the peak position of the plasmon resonances and the detailed balance analysis of the profile-averaged spectra (red curve). Both, effective density and effective temperature deviate significantly (i.e. more than 10%) from the corresponding mean values $\bar{n}_\mathrm{e} = 7.0 \times 10^{20}\,\mathrm{cm}^{-3}$ and $\bar{T} = 1.5\,\mathrm{eV}$. Also note that in different setups, e.g. excitation of the plasma via intense optical laser radiation, stronger density and temperature gradients are observed [129], and even larger deviations between the effective values and the mean values for $n$ and $T$ may occur. A further interesting observation is that the peaks of the averaged spectrum (Fig. 2.14) are not symmetrically located with respect to the incident photon energy as would be the case for a homogeneous temperature and density distribution in the target.

## Conclusions

We simulated Thomson scattering spectra including density and temperature gradients in the target. By comparing these spectra to calculations that assume homogeneous density and temperature distributions, we found significant differences between these methods. In particular, the free electron density that is inferred from the simulated spectrum from the plasmon dispersion, as well as the effective temperature, inferred via detailed balance analysis of the simulated spectrum may not be interpreted as the mean values of these observables. In the scenario studied here (FLASH photons at 13.5 nm wavelength scattering on near solid density hydrogen heated by the same photons), both $n_{\text{eff}}$ and $T_{\text{eff}}$ differ by more than 10% from the corresponding mean value.

Besides being important for the determination of density and temperature as demonstrated in this paper, deconvolution of the scattering spectra and the profiles is also crucial if one is interested in the broadening of the plasmon satellites due to collisions and Landau damping [56]. Collisional broadening of plasmons gives valuable information about the electrical and thermal conductivities in the plasma and is thus an important feature of the scattering spectrum. However, neglecting the homogeneous broadening due to the density and temperature gradients may lead to significant underestimation of the conductivity. Thus, gaining information about the density and temperature profile of the target, e.g. from radiation hydrodynamic simulations, is indispensable for the application of Thomson scattering spectra to plasma diagnostics.

## Acknowledgments

This work was partly supported by the Deutsche Forschungsgemeinschaft (DFG) under Grant SFB 652 “Strong correlations and collective phenomena in radiation fields: Coulomb systems, Cluster, and Particles”, by the DFG-Graduiertenkolleg 1355 (RRF), and the German Federal Ministry of Education and Research (BMBF) under Grant FSP 301-FLASH, project No. 05 KS7HRA.

# Chapter 3

# Experiments and Equipment

## 3.1 The FLASH Facility

Free electron lasers (FELs) are novel light sources with a variety of research applications ranging from diffraction imaging [90, 130] over cluster [131, 132] to atomic physics [133–135]. Their physical principle is described in text books (e.g. [136]) and the properties of the soft x-ray FEL in Hamburg (FLASH) in various publications (e.g. [15, 137–140]).

X-ray FELs are of particular interest for WDM research due to three key properties: They are capable of producing short wavelength light that can penetrate dense plasmas (see critical density, chapter 1.2, page 4), so that studies are not limited to surface effects. Furthermore, their fs pulse duration is substantially shorter than the plasma life time (ps to ns), which allows even the investigation of ultrafast fs equilibration processes. On top of that, the number of photons in an FEL pulse is sufficiently high to generate homogenous plasmas and to enable the Thomson scattering diagnostic, which has a low cross section (chapter 2.3). The latter two properties can be combined into the peak brilliance, which is the number of photons emitted per unit time, solid angle, source surface area, and within 0.1 % bandwidth. The figures of merit are displayed in a two dimensional graph for various current and future light sources (figure 3.1). It clearly shows the advantages of x-ray FEL sources for WDM research.

Besides the soft x-ray FEL itself, the FLASH facility also offers various diagnostic instruments. Of particular interest for this work is the residual gas ionization detector, also called gas monitor detector (GMD), and a spectrograph located in the soft x-ray transport line. The GMD measures the energy of each soft x-ray pulse [141]. This is important as FLASH uses self-amplified spontaneous emission, where the light pulse is amplified from noise

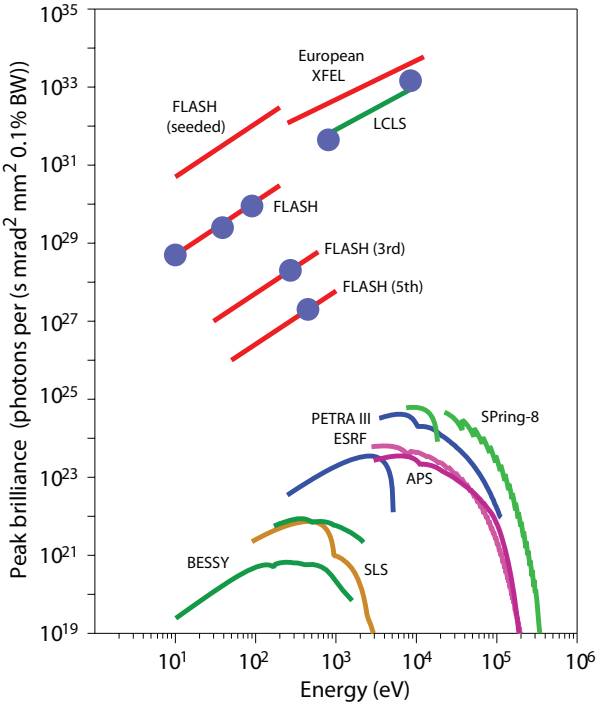


Figure 3.1: Peak brilliance of current and future light sources over photon energy (based on [15, 16]).

leading to ∼10% pulse energy fluctuation in our experiment. The FEL spectral structure can be measured by steering the soft x-ray pulse with a mirror into a spectrograph. However, the mirror blocks the light from reaching the experiment, so that no parasitic operation is possible. To monitor the FEL spectrum synchronously to the experiment we use an additional spectrograph at the experiment (section 3.5).

Two experimental setups were used. Figure 3.2 shows the instruments used for Thomson scattering and low FEL intensity solid bulk target irradiation and spectroscopy [5, 6] (chapters 4.2 and 4.3), while figure 3.3 depicts the setup for high intensity solid target irradiation with micro-focused FEL pulses and spectroscopy [4] (chapter 4.1). The following sections describe the most important components of the setup in more detail.

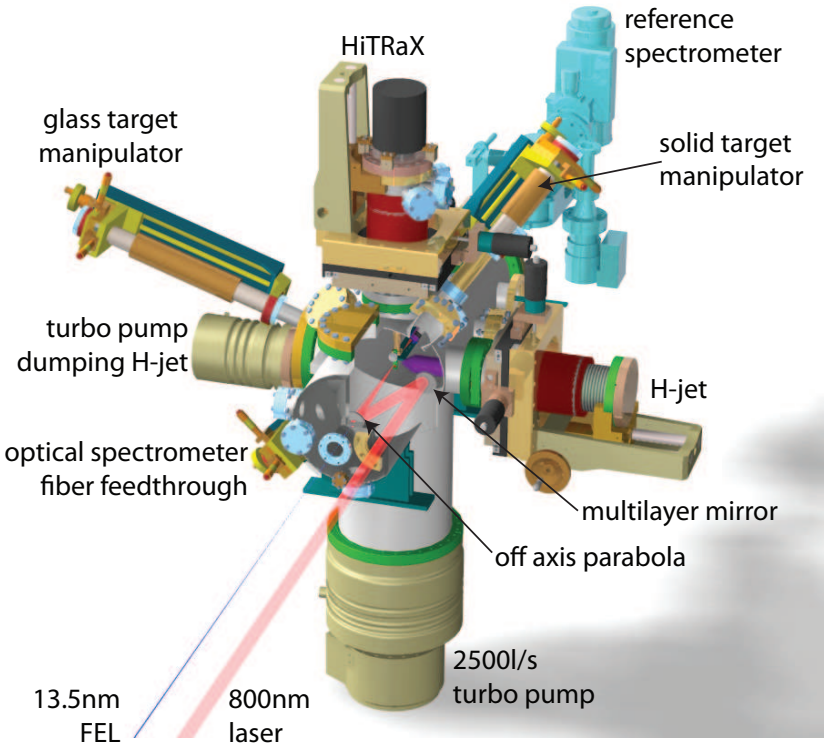


Figure 3.2: Raytrace of the Thomson scattering and bulk solid target irradiation experimental setup from computer aided design drawings. Interactive CAD drawings of this setup are in the appendix (figure A.1).

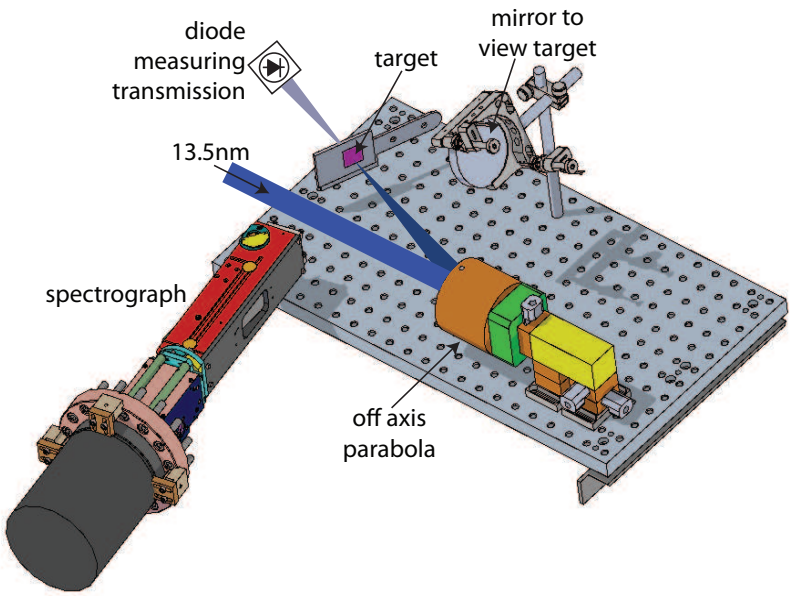


Figure 3.3: Experimental setup for high intensity solid target irradiation and transmission measurement, here depicted without vacuum chamber.

## 3.2 Soft X-ray scattering using FEL radiation for probing near-solid density plasmas at few electron volt temperatures[1]

*The following publication describes techniques and setup used for FEL sample heating, Thomson scattering (chapter 4.3, page 103) and emission spectroscopy (chapter 4.2, page 92). It also presents preliminary results that demonstrate the feasibility of the experiments.*

**Abstract**

We report on soft X-ray scattering experiments on cryogenic hydrogen and simple metal samples. As a source of intense, ultrashort soft X-ray pulses we have used free-electron laser radiation at 92 eV photon energy from FLASH at DESY, Hamburg. X-ray pulses with energies up to 150 $\mu$J and durations $15 - 50$ fs provide interaction with the sample leading simultaneously to plasma formation and scattering. Experiments exploiting both of these interactions have been carried out, using the same experimental setup. Firstly, recording of soft X-ray inelastic scattering from near-solid density hydrogen plasmas at few electron volt temperatures confirms the feasibility of this diagnostics technique. Secondly, the soft X-ray excitation of few electron volt solid-density plasmas in bulk metal samples could be studied by recording soft X-ray line and continuum emission integrated over emission times from fs to ns.

### 3.2.1 Introduction

Short-wavelength radiation exhibits significant differences in its interaction with matter compared to near-visible radiation. This had led to the proposal to employ intense, ultrafast, tunable and bright X-ray sources in studying properties of dense plasmas at an un-paralleled level of detail [122]. Several studies suggested the creation of solid-density plasmas by intense femtosecond X-ray pulses [137, 142] or the probing of dense plasmas using various X-ray scattering and spectroscopy techniques [13, 49, 125, 126, 143, 144]. Since existing conventional sources could not provide X-ray radiation with the required properties these experiments were, until recently, not possible. The first facility to provide intense, femtosecond, high brightness, soft X-ray

[1]Peer reviewed paper. This section has been published as: S. Toleikis, R.R. Fäustlin et al., High Energy Density Physics [2] © 2010 Elsevier B.V.

radiation is the free-electron laser (FEL) facility FLASH at DESY, Hamburg starting user operation in 2005 [15, 145]. In this paper we report on two types of soft X-ray plasma physics experiments, both carried out for the first time and both using 92 eV FEL radiation. These experiments aim at the investigation of thermodynamic properties such as electron temperature, electron density and ionization for strongly coupled plasma systems. In particular, the regime of interest is near-solid electron densities of $n_e = 10^{21} - 10^{23}\,\mathrm{cm}^{-3}$ and temperatures from a few to tens of electron volts.

In contrast to ideal plasmas, for strongly coupled plasmas correlations between the charged particles have to be considered. The regime of strongly coupled plasmas can be identified by the ratio of Coulomb energy to the thermal energy, i.e., the dimensionless coupling parameter $\Gamma = e^2/(4\pi\varepsilon_0 \overline{d} k_B T_e)$, being larger than unity, where $\overline{d} = (4/3\pi n_e)^{-1/3}$. The interest in studying these systems experimentally arises from the complexity of the theoretical description and the necessity to verify the applicability of models using experimental data. Experiments have been limited so far by the fact that near-visible laser methods bear intrinsic restrictions for the investigation of near-solid density matter.When using near-visible radiation the probing of dense matter is not possible due to strong absorption and reflection. Further, the generation of plasmas using high intensities is accompanied by complex shock wave creation as well as strong density and temperature gradients. X-rays overcome both problems due to their largely increased penetration power.

### 3.2.2 Description of experimental techniques

#### Measuring near-solid density plasma parameters using inelastic soft X-ray scattering

The measurement of plasma parameters such as temperature, free-electron density or ionization is required for the investigation of equation-of-state properties. One standard technique is Thomson scattering using near-visible radiation [94, 95]. The applicability of this method is limited to plasmas with much smaller densities than targeted here. For near-solid density plasmas X-ray radiation is required and the technique of X-ray Thomson scattering had been successfully introduced using few keV X-rays, generated by high-energy laser radiation interaction with backlighter samples [50, 51]. Since FEL pulses provide similar photon numbers per pulse as used in the reported high-energy laser experiments, but have an even higher brightness, it is conceptually straightforward to implement this inelastic X-ray scattering technique using these new sources. Moreover, the much higher repetition

rates of the FEL, when compared to the high-energy lasers, further facilitate the investigation of various samples, sample configurations, as well as scanning wide parameter ranges. At the same time the high temporal resolution in FEL experiments enables one to investigate the dynamics of plasma formation and equilibration. We report here initial experiments carried out in the soft X-ray regime at 92 eV photon energy.

The scattering kinematics in inelastic X-ray scattering is determined by the momenta of incoming X-ray photon $\overrightarrow{k_i}$ and scattered photon $\overrightarrow{k_f}$, where the momentum $\overrightarrow{K} = \overrightarrow{k_i} - \overrightarrow{k_f}$, $\left|\overrightarrow{K}\right| = K$ is transferred to the scattering particle. The kinematics determines if the collective plasmon-like character of electron excitations or noncollective single electron properties is probed. To distinguish the two regimes the scattering parameter $\alpha = 1/(K\lambda_{D,sc})$ is used. $\alpha > 1$ corresponds to the collective regime where the probed length scales are larger than the Debye screening length $\lambda_{D,sc}^2 = \varepsilon_0 k_B T/(n_e e^2)$. Here, scattering from collective electron excitations, i.e., plasmons, can be observed. In the non-collective regime, $\alpha < 1$, the probed length scale is shorter than $\lambda_{D,sc}$ and the momentum distribution for individual electrons is probed. The energy transfer from the photon to the single electron is $\hbar\omega = \hbar(\omega_i - \omega_f)$. For bound electrons with $\hbar\omega \geq E_B$; $E_B$ being the binding energy of this electron, Compton scattering becomes observable. Since the energy transfer in the soft X-ray regime is very small, typically below the energy resolution and difficult to investigate, these first inelastic X-ray scattering experiments using FEL sources have been carried out in the collective scattering mode. In this mode scattering from the plasmon gives rise to down- and up-shifted resonances, relative to the elastic scattering. From the energy difference of the resonances with respect to the FEL probe pulse the electron density can be estimated and the slope of the peak heights of the resonances allows an independent estimate of the electron temperature [13]. Experimentally, an infrared femtosecond laser is used to heat a liquid hydrogen sample with an initial density below solid-density. We estimate that the plasma equilibrates within a few picoseconds, before the measurement of plasma parameters by soft X-ray scattering occurs. Using two soft X-ray spectrometers at different scattering angles q, the simultaneous measurement of scattering for two values of a, respectively K, provides the possibility of investigating the scattering from electrons bound to the ions [34].

### Creation of solid-density plasmas using soft X-ray radiation

The current operation of FLASH allows one to obtain intensities up to $10^{17} - 10^{18}\,\mathrm{Wcm}^{-2}$ by focusing the soft X-ray FEL beam. The interaction of the focused soft X-ray radiation with a small volume of solid-density matter

can lead to an energy deposition of up to $\approx 10^3\,\mathrm{kJ/cm^3}$ and subsequent plasma formation. The energy absorption occurs over the duration of the FEL pulse of few ten femtoseconds, which is too short for the material to expand. For our experimental conditions and sample materials the primary absorption process is photoabsorption by L-shell electrons. Initially, the material enters into a highly excited, non-equilibrium state that develops with time after the FEL impact. During the entire cycle the sample transits from strongly-correlated cold matter, via a highly excited non-equilibrium plasma, to an equilibrated plasma state that cools down while expanding. Both continuum and line emission occur at different times in this cycle. The spectral shape of the continuum radiation and the relative intensities of plasma emission lines can be used to determine plasma parameters [5]. In these experiments one has to consider averaging effects due to spatially varying energy deposition and to time integration of the developing plasma states. Initially no time resolution could be applied to the spectral measurements. Therefore it is not possible to determine when radiation from the various emission channels occurred.

### 3.2.3 Experimental setup

Experiments have been carried out using soft X-ray radiation provided by FLASH, an FEL facility operating in the self-amplified spontaneous emission (SASE) mode [136]. In FLASH very low emittance electron bunches are generated in a photo-injector and are immediately accelerated to avoid space charge effects. After two compression steps using magnetic chicanes the electrons are accelerated to their final energy of $300 - 1000\,\mathrm{MeV}$, producing soft X-ray FEL radiation, in a fixed gap 30 m long permanent magnet undulator, in the range $30 - 200\,\mathrm{eV}$ [140]. In these experiments we used 92 eV photon energy, which corresponds to an electron energy of 700 MeV. In the employed operation mode of FLASH the electron bunch, which has a higher density on the its leading edge, generates X-ray pulse durations of $15 - 50\,\mathrm{fs}$ with a bandwidth near 1.0% and pulse energies up to 150 mJ. These X-ray pulses are transported to the experiments using carbon-coated mirrors operated at a grazing angle of 2 and 3°. The experiments have been carried out at BL2 of FLASH with two flat and one ellipsoidal mirrors, the latter producing a focal spot of $20 - 30\,\mathrm{mm}$ diameter (FWHM). The total beamline transmission is considered to be $64 \pm 4\%$ [140].

For the experiments reported here fluctuations of the pulse energy and of the spectral distribution need to be considered. The pulse energy Io is measured pulse-by-pulse and this measurement is used for normalization of single-pulse data [141]. For measurements that integrate over several X-ray

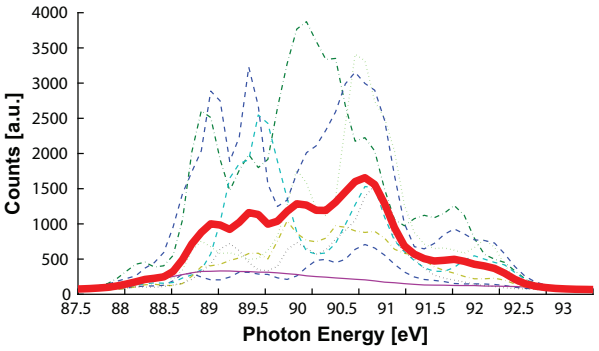


Figure 3.4: Single-pulse spectra indicating the pulse-to-pulse fluctuation of the spectral distribution of incident SASE FEL pulses. The bold line corresponds to the spectral distribution averaged over 8 pulses and indicating the incident bandwidth of ∼2 eV corresponding to ∼2 % relative bandwidth.

pulses the averaged pulse energy is used for normalization. The spectral distribution also fluctuates from pulse-to-pulse as is shown in Fig. 3.4. In the case shown, which has been collected during a particularly unstable period of FEL operation, the averaged distribution exhibits a bandwidth of ≈2% corresponding to 2 eV, and the individual spectra indicate a spectral structure with a typical peak width of 0.3 − 0.5 eV. Since only few modes are populated the weight of the spectral distribution can vary strongly from pulse-to-pulse. In order to normalize the scattering spectra with respect to this fluctuation an additional spectrometer measures the spectral distribution of the incident beam. Fluctuations of the temporal distribution of the FEL pulses can occur within an envelope of smaller 50 fs, but do not affect the data analysis presented here. FLASH can accelerate trains of $1 - 800$ electron bunches with a repetition rate of 5 Hz. The repetition rate of bunches within the train can be selected between 40 kHz and 1 MHz. Most of the experiments reported here have used single pulses or a 5 Hz repetition rate. In a few cases trains with up to 30 pulses at 5 Hz, corresponding to 150 pulses per second have been used to increase the counting statistics.

The experimental setup is mounted in ultrahigh vacuum conditions using a total of 2200 l/s pumping speed. The geometry is chosen such that the soft X-ray spectrometers are mounted in the vertical plane at scattering angles $\theta$ equal to 0, 16 and 90°. The choice of the vertical plane follows from the very high degree of linear polarization of incident radiation in the horizontal plane. The spectrometer at $\theta = 0°$ is used for measuring the spectral distribution of the incident radiation. In flat-field geometry a planar variable line spacing grating with 1200 lines/mm is mounted at ∼170 cm from the interaction point. A 100 $\mu$m slit is used for background reduction and vacuum separation.

For detection a back-illuminated CCD is used and we obtain an energy resolution $\Delta E/E \cong 3.6 \times 10^{-3}$ [146]. The spectrometer at $\theta = 16°$ employs the same spectrometer principle and the same grating, which is mounted 23.5 cm from the interaction point. The main spectrometer, mounted at $\theta = 90°$, was optimized to provide large solid angle, high throughput and high spectral resolution in order to maximize the signal level. For the first experiment a focusing spectrometer based on a transmission grating was used [147], but artifacts arising from the support grid of the grating and the need for improved alignment and higher efficiency led to design and construction of a new spectrometer [3]. This spectrometer employs a toroidal mirror together with an 800 lines/mm variable line spacing reflection grating, accepts a solid angle of $19 \times 10^{-4}$ sr, obtains a resolution of $\Delta E/E \cong 5 \times 10^{-3}$ at 92 eV and has an estimated throughput of $\approx 4 \times 10^{-2}$ including detection efficiency of the back-illuminated CCD. In addition to the soft X-ray spectrometers we use optical spectrometers for detection of emission radiation in the near-visible regime. Analysis of line and continuum emission in this regime should provide further information about the temperature of the hydrogen plasma.

The samples are positioned in the focus of the FEL beam. The inelastic scattering experiment uses a liquid hydrogen jet produced by nozzles of $10 - 20$ mm diameter at a temperature $\sim$20 K [148]. The jet diameter under ideal conditions is equal to the nozzle of the liquid hydrogen source. The preparation of the liquid jet can lead to a variety of jet conditions. The phase space of liquid hydrogen is rather dense in this regime and small fluctuations of parameters like pressure or temperature and impurities will lead to rather strong variations. In particular, we have observed that the mean density of the liquid jet can vary strongly. In the ideal condition we observe a homogeneous jet of liquid hydrogen with a mass density $\rho = 0.0706\,\mathrm{gcm}^{-3}$ [149]. In another operation mode the hydrogen is ejected in tiny droplets with liquid density forming a jet with a mean density approximately 5-10 times less than for the liquid. The solid samples are mounted on a manipulator enabling translation to the chamber center once the liquid hydrogen source is retracted. The incidence angle of FEL radiation is roughly 45° with respect to the sample surface.

The near-solid density hydrogen plasma is created using a femtosecond infrared laser delivering $3 - 5$ mJ pulses at 800 nm at 5 Hz into a focal spot of $\sim$30 $\mu$m diameter. A nearly collinear excitation geometry using a parabolic mirror with a central hole is chosen. With a measured pulse duration of roughly 150 fs obtained by compression of the stretched pulse just before entering the vacuum chamber this system reaches intensities of $\geq 10^{15}\,\mathrm{Wcm}^{-2}$ [150]. The laser is synchronized using a radiofrequency clock to the arrival of the X-ray pulse with an accuracy of few ps over of several hours duration

[151]. Sub-picosecond time resolution can be obtained in a pulse-by-pulse measurement of the temporal fluctuation of the infrared laser with respect to theX-ray arrival [152]. In the experiments reported here we use a time resolution of the order $1-2$ ps obtained by cross-correlating the infrared laser to visible synchrotron radiation using a streak camera [151]. To improve the signal-to-noise ratio we always analyzed differences of two measurements: Onewith the infrared laser before the FEL, leading to plasma formation, and a second, with the infrared laser after the FEL, thus probing the cold hydrogen system. In addition, background images without X-ray illumination and of similar duration are taken to account for stray scattering and detector noise.

In the reported experiments X-ray scattering emerges from an interaction volume formed by the crossing of the soft X-ray beam of 25 $\mu$m (FWHM) diameter and the 20 $\mu$m diameter cryogenic liquid hydrogen jet. The incident intensity in this scenario is $2.5 \times 10^{14}$ Wcm$^{-2}$ corresponding to 30 $\mu$J pulse energy at the sample, 25 fs duration and 25 $\mu$m focal spot diameter. The absorption length of 92 eV radiation in liquid hydrogen of 9.5 $\mu$m [72] corresponds to 12% transmission for a 20 $\mu$m thick sample. For the measurements on solid aluminum and magnesium the FEL beam hits the surfaces at an angle close to 45° and the absorption lengths are 0.036 $\mu$m and 0.039 $\mu$m, respectively. These absorption lengths are valid for the unperturbed ground-state materials. If the deposited energy is sufficient to modify the material properties significantly, one has to consider a transiently changing absorption. We have simulated this effect using the HELIOS code [78] assuming that the energy deposited by the FEL beam is absorbed through photoabsorption and inverse Bremsstrahlung. For the particular conditions the main mechanisms are bound-free (photoionisation) and free-free (inverse Bremsstrahlung) transitions. To determine the appropriate ratios the code uses the sample charge state which is obtained from tabulated values via the current electron temperature which for simplicity is assumed to settle on a timescale shorter than the pulse durations. The simulations confirm that the soft X-ray FEL pulse heats the sample more homogeneously than the infrared laser pulse. We are currently investigating the effect of inhomogeneous heating of the liquid hydrogen jet by the infrared laser leading to variations of the electron temperature and density. Initial analysis indicates that the use of the plasmon peak to estimate the plasma parameters provides good accuracy [1].

For the experimental conditions of these experiments we obtain the following relation for the scattering parameter

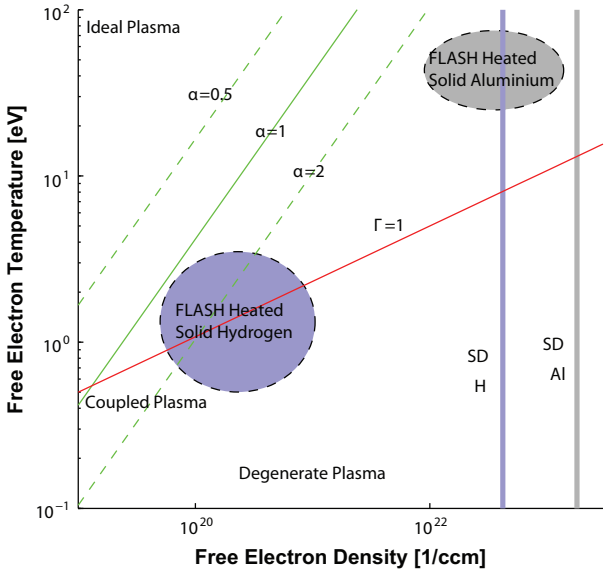


Figure 3.5: Phase space representation for electron density $n_e$ and temperature $T_e$, probing photon energy $\hbar\omega = 92\,\mathrm{eV}$ and scattering angle $\Theta = 90°$. Lines for $\alpha = 0.5$; 1; 2 and $\Gamma = 1$ have been calculated according to the relations in the text and in equation (1). Filled areas indicate the expected parameter regimes for hydrogen and Al plasmas investigated. Densities of cold hydrogen and aluminum are indicated.

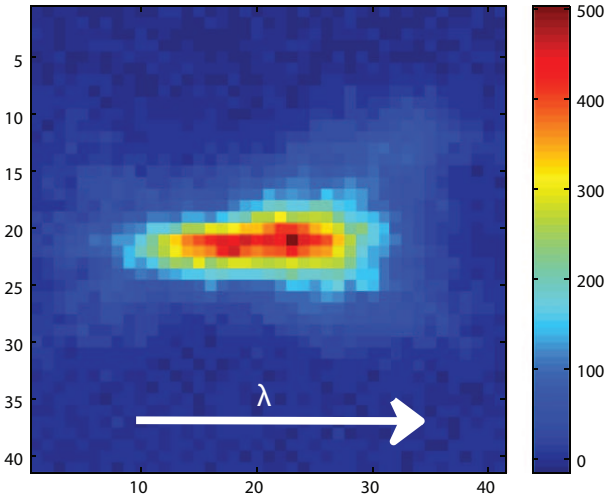


Figure 3.6: Scattering signal from a single FEL pulse of 60 mJ energy at the sample obtained at the CCD of the HiTraX spectrometer [3] after background subtraction. 500 counts in the maximum correspond to a very high S/N ratio that is well beyond 50.

$$\alpha = \frac{e\sqrt{n_e}}{K\sqrt{\varepsilon_0 k_B T_e}} \cong 20.4 \times \frac{\sqrt{n_e\,[10^{22} cm^{-3}]}}{\sqrt{T_e\,[eV]}} \tag{3.1}$$

that is shown graphically in Fig. 3.5. One finds that in the case of liquid hydrogen scattering occurs in the collective regime for all densities between the liquid ($n_e = 4.2 \times 10^{22}\,\mathrm{cm}^{-3}$) and expanded densities of below $n_e \approx 10^{20}\,\mathrm{cm}^{-3}$ if one assumes that the electron temperatures do not exceed a few eV. For solids ($n_e \approx 10^{23}\,\mathrm{cm}^{-3}$) temperatures can be considerably higher still fulfilling the condition for collective scattering. Using 60 $\mu$J FEL pulses at the sample and scattering from a liquid hydrogen jet of $\sim$20 $\mu$m diameter we are able to obtain significant scattering from a single pulse (compare Fig. 3.6). These are ideal conditions for this experiment, as they allow measuring the beam properties of FEL beam on a pulseby- pulse basis. Unfortunately we could not operate the whole experiment in this mode but had to collect scattering data from laser-heated hydrogen plasma using integration over several hundred pulses. During integration both FEL pulse energy and mean density of the liquid jet were fluctuating. In this mode signal was collected over a predefined time and in parallel the mean FEL pulse energies and the spectral distribution were measured for normalization of the scattering data. In order to normalize the fluctuations of the liquid jet a monitoring signal is needed which is linear with respect to the scattering probability of the FEL beam. Two approaches were attempted: First, one can use the transmitted beam intensity to determine the absorbed beam fraction. This method was shown to be unfeasible since a detector for the transmitted beam gets overloaded with the infrared pump laser beam. Second, one can use a fast, pulse resolved scattering signal. Both light scattering and particle emission have been analyzed using a multi-channel plate detector mounted for this purpose. The normalization using this signal works, in principle, providing sufficient counting statistic can be acquired. As this is not always the case, the error margin can be relatively high.

Providing fresh sample volumes is a prerequisite for integrating experiments. Using the liquid jet with an expansion speed $\sim$60 m/s we calculate that fresh sample volumes are safely achieved for FEL repetition rates up to 1 MHz. Using the femtosecond infrared laser for pumping the system experiments were carried out using the 5 Hz repetition rate. In the solid experiments the sample was continuously translated using the 5 Hz repetition rate of the FEL.

### 3.2.4 Results and discussion

The results of soft inelastic X-ray scattering experiments from liquid hydrogen can be separated into two areas. These are: a) the experimental procedures to observe scattering of FEL radiation and detection using efficient spectrometers and b) the time-resolved investigation of the parameters of an infrared laser prepared hydrogen plasma. The experiment itself can be subdivided into (i) the scattering of FEL radiation including the preparation and characterization of the FEL beam and the spectrometer for efficient detection, (ii) the sample preparation and characterization and (iii) the infrared laser heating of the hydrogen plasmas.

For soft X-rays absorption is considerable even in the case of the reduced density of liquid hydrogen. The energy absorbed from the focused FEL radiation will therefore itself lead to strong excitation of the sample that eventually leads to plasma formation. The amount to which a transient change of the sample affects the inelastic scattering, a process called self-scattering, is the issue of a forthcoming publication [153]. The experimental results show that the two parameters of the FEL radiation that are most critical to the success of these experiments are the pulse energy and the bandwidth. It is found that a pulse energy of order $30 - 50\,\mu$J is needed to obtain a significant amount of scattered signal using single pulses or very short (few 10 s) integration times. In addition, it is crucial that the liquid hydrogen source operates stably throughout the integration time in the high average density liquid jet mode. Short integration times can be still acceptable as the stabilization of parameters can work on this timescale. Further, it is extremely critical for the observation of plasmon peaks that the bandwidth of incident FEL radiation be sufficiently small and the spectral resolution of the spectrometer be sufficiently high. As shown in Ref. [13] the shift of the plasmon signal with respect to the elastic scattering is in the order of only a few eV. The broadening of the spectroscopic data due to the incident bandwidth or by spectrometer resolution would wash out the experimental results. A total spectral resolution better than 1% is therefore required for the conditions of these experiments. Fig. 3.7 shows experimental data obtained from liquid hydrogen. Spectra shown are for the cases of infrared laser arriving 3 ps before and 3 ps after the FEL pulse and integrating over 9000 pulses at 5 Hz. Since the two spectra do not differ significantly we subtract them after background subtraction and normalization to the same value. The resulting difference signal yields a small signal. Also shown are the corresponding spectra of the incident FEL radiation, measured at $\theta = 0°$ and using the same integration times as for the scattered spectra. After normalization the difference profile of the incident FEL radiation shows features similar to the difference pro-

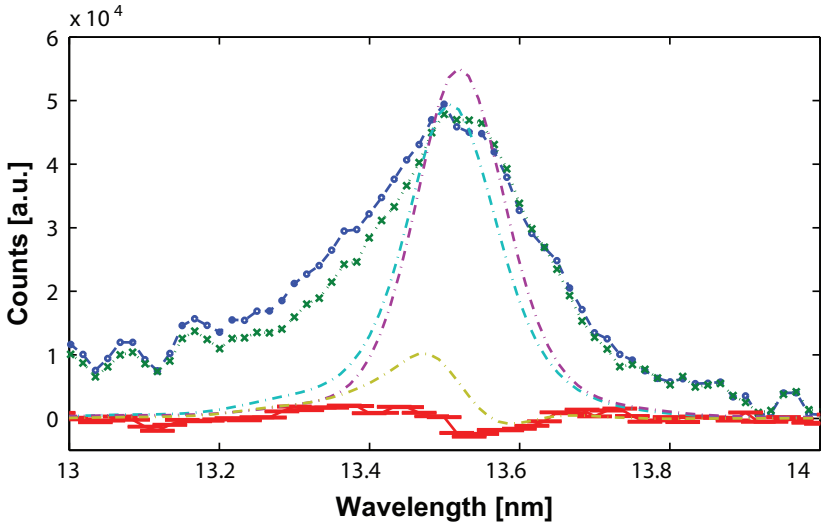


Figure 3.7: Soft X-ray Thomson scattering spectra near 92 eV from hydrogen integrated over 9000 FEL pulses. Scattering spectra for the cases that the 800 nm infrared laser hit the liquid hydrogen 3 ps prior (dots, broken line) and 3 ps after (crosses, dotted line) the FEL pulse are shown. Differentence spectra (error symbols, line) have been obtained from normalized scatter data after background subtraction. The corresponding FEL spectra and their difference are shown as dash-dotted lines.

file of scattered radiation. In this case we conclude that likely fluctuations of the spectral composition of FEL radiation over the integration period of the measurement are responsible for the different profiles. This result demonstrates the crucial importance of a simultaneous measurement of the spectral composition of FEL radiation and the requirement that the FEL must operate under very stable conditions in order to enable experiments of this kind. Comparing the peak width of the scattered radiation and the measured FEL spectrum we observe a clear broadening in the scattered spectrum. Whether this broadening is due to inelastic scattering near the elastic peak or is due to source broadening requires still further clarification. The oscillations of the signal away from the scattering peak is reproducible and are due to density modulations of the 200 nm Zr filter for visible light suppression inside the spectrometer.

The preparation of the liquid hydrogen jet needs to include the characterization of its correct alignment with respect to the crosssection of FEL beam, optical laser and spectrometer axis and of the mean density of the jet during the measurement. These measurements are critical for determining

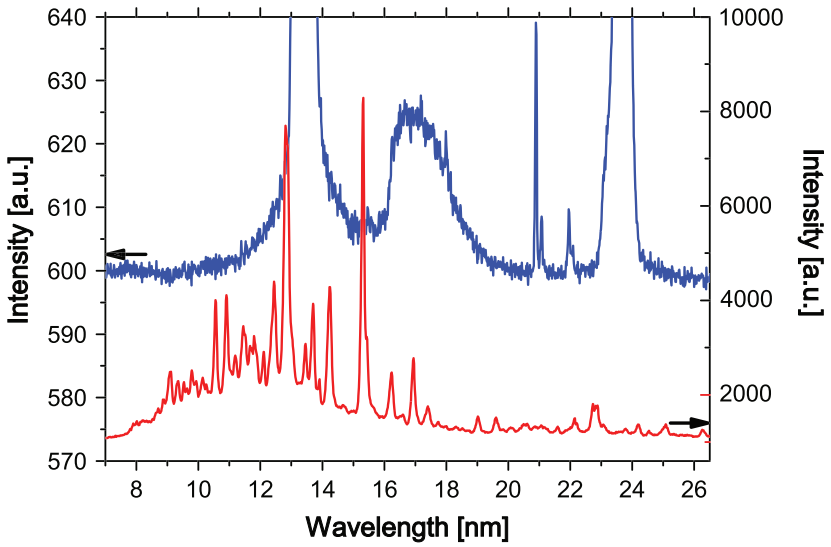


Figure 3.8: The upper curve shows an unfiltered soft X-ray spectrum obtained from bulk aluminum following impact of 92 eV FEL radiation and the lower curve the spectrum for 1.6 eV infrared laser radiation using a 200 nm Zr filter. The intensities were $4 \times 10^{14}$ Wcm$^{-2}$ and $4 \times 10^{15}$ Wcm$^{-2}$, respectively.

the absolute scattering intensity, e.g. in investigations of the FEL intensity dependence of the amount of self-scattering. We further note that the fluctuations of the infrared laser pulse energy and beam pointing need to be monitored to ensure identical plasma conditions in these highly repetitive measurements.

These experiments are challenging in that FEL, liquid hydrogen jet, and infrared laser have to operate simultaneously with specified parameters otherwise the experimental outcome will be compromised. Integration over many FEL pulses introduces uncertainty and broadening of experimental parameters which are crucial to the observation of results for the plasma parameters. On the other hand, the operation of FLASH at high pulse energies ($> 30\,\mu$J) has shown the feasibility of carrying out these measurements using single-pulse spectra. In this case the accumulation of a significant amount of spectral data with good resolution can be achieved by sorting data according to simultaneously measured FEL and infrared laser data. Also, dependencies related to FEL intensity or sample variation can be followed using this procedure.

The impact of the FEL pulse on solid samples was investigated by observation of emission radiation using the same experimental setup. The deposited

energy leads to the formation of a plasma exhibiting emission characteristics that are fundamentally different from those of a plasma created by an infrared laser of similar intensity. Fig. 3.8 shows a comparison of the emission spectra of a bulk aluminum sample for FEL and infrared laser irradiation. Following soft X-ray excitation one observes, in addition to the elastically scattered soft X-ray radiation, a strong difference of ion line emission and continuum radiation indicating the different plasma state the aluminum has turned into after soft X-ray irradiation. In contrast to the elastic and near-elastic scattering the continuum, the ion line emission can occur at delayed times after impact of the FEL pulse. The spectra shown in Fig. 3.8 integrate over timescales up to ns in which the plasmas may emit. Detailed results of this characterization of FEL createdwarm dense Al plasmas using soft X-ray emission spectra have been published separately [5]. In order to achieve high statistical accuracy during these measurements they are carried out integrating over a large number of FEL pulses. The variation of FEL pulse energy and the modification of sample conditions related to the high repetition rate of the FEL pulses require further investigation using single-pulse spectra.

### 3.2.5 Conclusions

The experimental procedures for soft X-ray inelastic scattering experiments on cryogenic liquid hydrogen jets using FEL radiation have been developed. The observation of single-pulse scattering spectra using efficient spectrometers is found to be possible. First results have been obtained for the time-resolved investigation of the parameters of an infrared laser prepared hydrogen plasma. The interaction of the FEL pulse with the sample leading to plasma heating, thereby changing the measured state, is still under investigation. The experiments reported here were the first of their kind carried out using FEL radiation. The results of these experiments indicate the requirements for future experimental campaigns with respect to diagnostics of FEL and infrared laser radiation as well as sample characterization. Scattering data have been collected using an integrating 5 Hz mode for laser-heated hydrogen plasmas varying the time delay between excitation and probing. These results will be subject of future work. Most importantly we found that single-pulse scattering on liquid hydrogen gives significant scattering signal for a detailed study of plasma conditions. Applying single-pulse data collection offers the advantage of reducing statistical errors and experimental uncertainty introduced by integration over varying parameters.

For solid aluminum samples the absorption of intense soft X-ray FEL radiation and subsequent formation of warm dense plasmas have been investigated by observation of the time-integrated emission spectrum which differs

strongly from the spectrum after heating using infrared lasers.

## Acknowledgements

This work was initiated by the Virtual Institute Plasma Physics using FEL radiation funded by the Helmholtz association under No. VH-VI-104 and is continued in the project FSP 301-FLASH funded by the German Federal Ministry for Education and Research. University Rostock acknowledges support by the Deutsche Forschungsgemeinschaft through the SFB 652 and RRF received support for the spectrometer and simulation codes from the GRK 1355 at University Hamburg. The provision of a CCD detector by D. Riley at QUB, U.K., and support for access to FLASH by DESY and by the European Community under contract RII3-CT- 2004-506008 (IA-SFS) are gratefully acknowledged.

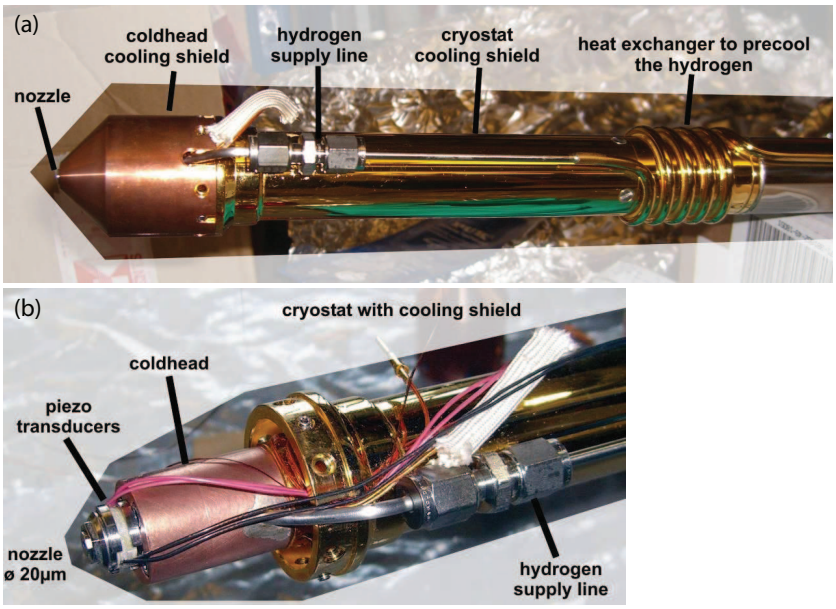


Figure 3.9: Description of the hydrogen source components with (a) and without (b) heat shield.

## 3.3 Cryogenic Hydrogen Jet

As a target for Thomson scattering experiments we use a liquid hydrogen jet [154, 155]. Its location in the experimental setup is depicted in figure 3.2. Hydrogen has the advantage of being the most simple element which reduces the number of processes that can occur in the plasma. In particular, Auger decay (section 2.1.2, page 15) does not occur. Furthermore, the jet provides a target with sufficient refresh rate so that we can make use of the 5 Hz FEL repetition rate by integrating scattering spectra over several pulses. Also, hydrogen has with $Z = 1$ the lowest number of bound electrons and, therefore, a small elastic scattering signal (see Thomson scattering, section 2.3.2, page 29). This facilitates to spectrally resolve the plasmon peaks from the elastically scattered signal.

The source of this jet is based on a cryostat (figure 3.9). It cools the hydrogen by liquid helium to around 20 K and injects it into the vacuum chamber through a 20 $\mu$m nozzle with about 1 bar pressure. The hydrogen reaches a speed of around 60 m/s which guarantees a new target for every FEL pulse.

Moreover, the nozzle is equipped with piezoelectric actuators which can induce a controlled and reproducible breakup of the liquid jet into droplets

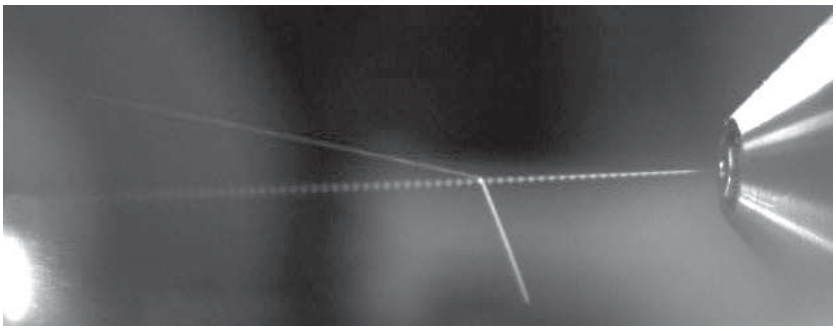

Figure 3.10: Modulated hydrogen jet ejected from the cryogenic nozzle into the vacuum chamber. One can see how a droplet collides with another droplet which has been reflected by the chamber walls and is substantially slower than the stroboscopic illumination. See also the appendix for a video of the source (figure A.3).

via the Rayleigh instability. The formation of droplets can be adjusted by the vibration frequency and amplitude of the actuators. Figure 3.10 shows the nozzle ejecting a modulated hydrogen jet. A video of the source operation can also be seen in the appendix (figure A.3). By changing the phase of the actuator frequency with respect to the FEL pulse one can adjust the location of the droplet during that event. This way, one can synchronize the arrival of a droplet at the interaction point with the arrival of an FEL pulse. After switching off the piezoelectric actuators the string of droplets transforms back into a continuous jet.

# 3.4 A Compact Soft X-Ray Spectrograph Combining High Efficiency and Resolution[2]

*The following publication describes a spectrograph which was constructed with the Thomson scattering requirements in mind, namely high resolution and throughput. It is the main diagnostic of the Thomson scattering and low intensity bulk target irradiation experiments of this work (chapter 4.3, page 103). Due to its flexibility it could also be used with the experimental setup for high intensity solid target irradiation (chapter 4.1, page 84). Interactive CAD drawings of the spectrograph are also shown in the appendix (figure A.2).*

**Abstract**

A compact and light weight soft X-ray spectrograph covering $5 - 35\,\mathrm{nm}$ and employing a toroidal mirror and a variable line space reflection grating has been newly developed. Particular emphasis has been placed on achieving a large collection solid angle ($1.9 \times 10^{-3}\,\mathrm{sr}$) and a high efficiency of the components in order to enable Thomson Scattering plasma diagnostics which has a small total cross section ($6.65 \times 10^{-25}\,\mathrm{cm}^2$). The instrument achieves a signal-to-noise ratio of 5 with a 13.5 nm source which isotropically emits $2.5 \times 10^5$ photons. A resolution $\lambda/\Delta\lambda = 330$ was measured at 21 nm and the dispersion was calibrated. The instrument is housed inside a DN 100 CF ultra high vacuum manipulator ($43 \times 46 \times 47\ \mathrm{cm}^3$) which allows positioning relative to the source within $\pm 5\,\mathrm{mm}$ and $\pm 50\,\mathrm{mm}$ in X,Y and Z direction, respectively. It can be used with or without entrance pinhole and is equipped with a motorized grating, a filter wheel with five filters, and a shutter. Altogether, these features make the spectrograph a versatile instrument which can be employed in a variety of physics applications such as line and bremsstrahlung spectroscopy or Thomson scattering.

## 3.4.1 Introduction

Soft X-ray emission and scattering spectra are of great interest for various fields of physics. Possible applications range from the investigation of liquid and solid matter electronic structure [156] over lithography [157] and

[2]Peer reviewed paper. This section has been published as: R.R. Fäustlin, U. Zastrau, S. Toleikis et al., Journal of Instrumentation [3] 

astrophysics [158, 159] to plasma diagnostics [5, 53]. In particular, plasma emission spectroscopy has profited from the abundance of emission lines in the range from 2 to 35 nm motivating the construction of advanced spectrographs [147, 160, 161]. The advent of soft X-ray free electron lasers (FELs) with the first of its kind in Hamburg (FLASH, DESY) [15] opens this spectral range for applications requiring higher intensity radiation. Here, we focus on the realization of soft X-ray Thomson scattering to investigate dense plasmas [2, 13, 117]. With this technique, temperature, density and degree of ionization of the plasma can be obtained via the spectral measurement of inelastic and elastic scattering components of the probe radiation [22]. It demands sufficient resolution to discriminate the different spectral contributions which is $\lambda/\Delta\lambda \geq 100$ in the FEL case [13]. More challenging, a high collection angle and efficiency of the spectrograph are required, as the total cross section for Thomson scattering is relatively small ($6.65 \times 10^{-25}\,\mathrm{cm}^2$). The greatest challenge is to integrate all these requirements into a most compact spectrograph so that it can be attached to various experimental chambers. Compactness and versatility are also what commercial products fail to offer. Therefore, the design of a new spectrograph was necessary. Beyond fulfilling these specifications, we aimed to construct a most versatile, easy to operate and in vacuum adjustable instrument with motorized filter change, motorized grating rotation and motorized shutter. In this paper we present the successful technical realization of these design goals as well as the calibration of the High Throughput, High Resolution Spectrograph for Soft X-Ray Light (HiTRaX) which has already been applied in various experiments [2, 4].

### 3.4.2 Design

For the use in soft X-ray ($5 - 35\,\mathrm{nm}$) Thomson scattering the spectrograph requires a resolution $\lambda/\Delta\lambda \geq 100$ [13], a maximized efficiency due to the low cross section, various filters to suppress visible light over the whole spectral range, and a compact and light weight construction to be compatible with various experimental chambers and geometries. The combination of these design goals made the construction of a new instrument necessary. To increase the efficiency and in particular the acceptance angle, a collection and imaging optic is needed. As a dispersive element, we choose a planar variable line space (VLS) grating. It is more robust against the necessary evacuation and venting cycles of the instrument then the alternative transmission gratings, as the latter have to be free standing in this wavelength region (e.g. [147]). Also, larger transmission gratings are supported by a grid structure which in turn produces artifacts in the dispersion direction. Therefore, we chose customized reflection optics from Horiba Scientific$^{\mathrm{TM}}$.

 

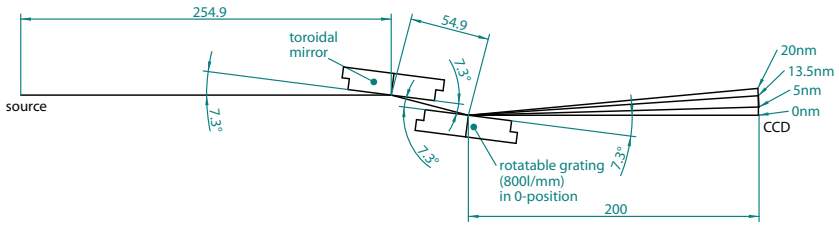


Figure 3.11: Geometry of the optics utilized in the spectrograph. Dimensions are in mm or degrees.

These are platinum coated and consist of a toroidal mirror and a planar variable line space (VLS) holographic grating with an average line density of 800 lines/mm (Figure 3.11). The mirror root mean square surface roughness was measured 0.6 nm which enables a high specular reflectivity throughout the wavelength range. Both optics have an active optical surface area of $50 \times 20\,\mathrm{mm}^2$. The mirror images the source with no magnification onto a Princeton Instruments PIXIS-XO: 2KB$^{\mathrm{TM}}$ back thinned CCD which has a pixel size of $13.5 \times 13.5\,\mu\mathrm{m}^2$. The grating in between CCD and mirror disperses the image spectrally while the variable spacing of the lines focuses the light further along the dispersion direction improving spectral resolution and producing a flat focal plane. The CCD ($28 \times 7$ mm) then typically records a spectral bandwidth of 35 nm without moving grating or camera. To obtain high reflectivity even with soft X-ray light the optics are placed at grazing incidence geometry for total external reflection (78% at 7.3 degree and 13.5 nm for the mirror [72]). The distance between mirror and source is 255 mm resulting in a solid collection angle of $1.9 \times 10^{-3}$ sr. Figure 3.11 shows the distances and angles of the optical components in the setup.

The spectrograph includes a motorized shutter to protect the optics from debris when not in use, motorized grating rotation with ±3 degree range of motion and a motorized filter wheel containing up to five filters (Figure 3.12). The electric motors are vacuum compatible and all are equipped with drive trains that do not require end switches, reducing possible sources of malfunction. The shutter is driven via a slipping clutch, the planar grating via an excenter wheel and the filter wheel can rotate perpetually. The filters help suppress visible light to which the CCD is sensitive as well as certain ranges in the soft X-ray spectrum depending on the filter material. The most used filters are 200 nm thick zirconium and aluminium which suppress visible light and have a bandpass of 6 nm − 16 nm and 17.1 nm − 75 nm, respectively. These filters can be produced without fractures or holes and thus reduce visible and stray light reliably. Their dimensions (28 mm × 6 mm)

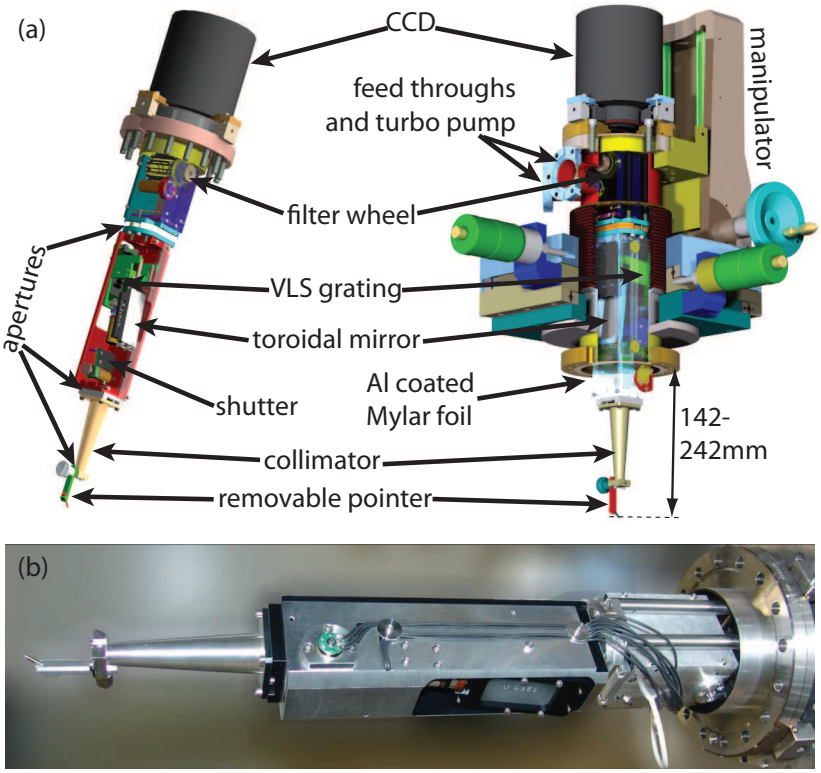


Figure 3.12: Three dimensional raytrace of the computer aided spectrograph design (a) indicating various components of the instrument in (right) and outside (right) of the manipulator. (b) Photograph of the spectrograph interior.

match the local soft X-ray beam size. The filter wheel is located between the CCD and the grating, away from the source, to protect fragile filter foils from debris that is common in laser plasma experiments. Furthermore, the filter wheel is surrounded by sufficient open space to minimize the pressure on the foils by air currents during evacuation and venting of the apparatus. The components facing the optical path have been anodized and dyed black to minimize stray light. Three apertures (Figure 3.12), shaped and experimentally adjusted to the optics outer dimensions also reduce stray light. The optics housing is built from aluminium to reduce weight to a minimum.

The whole spectrograph was built compact enough to be completely embedded in a DN 100 CF ultra high vacuum three-way-manipulator with dimensions $43 \times 46 \times 47$ cm$^3$. Using the manipulator the instrument can be adjusted by $\pm 5$ mm parallel and $\pm 50$ mm perpendicular to the DN 100 CF base flange. These degrees of freedom as well as a removable tip pointing to

the source location reduce alignment time to the source significantly and allow the spectrograph to adapt to possibly changing source locations without having to break vacuum. The removable tip can be replaced with a pinhole holder so that high resolution spectra can be recorded even with large radiation sources. A flexible, 20 $\mu$m thin Mylar foil coated on both sides with 250 nm of Al covers the gap between the spectrograph and the opening of the DN 100 CF manipulator to prevent stray light from reaching the CCD while maintaining the full range of motion (Figure 3.12). The foil also separates the vacuum chamber of the experiment from the spectrograph interior, which is differentially pumped by means of a small turbo pump. Thus, the interior reaches an estimated pressure of $10^{-6}$ mbar. This prevents residual gas freeze-out on the CCD chip which is peltier cooled to $\sim$200 K with ambient air and no additional water cooling is necessary. The CCD housing is held in place using clamps. These press the CCD flange with an o-ring seal against the polished surface of the DN 100 CF. The construction allows the CCD to be rotated and shifted parallel to the flat flange surface when the instrument is not evacuated, thereby aligning the camera to the dispersion direction. Via this flange the filter wheel can be accessed quickly without having to remove the whole instrument and thus without loosing neither time nor alignment of the whole instrument. The above features allow a seamless integration and operation within the Thomson Scattering setup at FLASH for a most efficient use of experimental time.

### 3.4.3 Measurements and Calibration

#### Dispersion

The dispersion was calibrated using radiation from the DORIS-III synchrotron beam line BW3 [162–164] at DESY. The monochromator of this beam line delivers $10^{12}$ photons per second with an energy between 2 nm and 80 nm and a typical resolution of $\lambda/\Delta\lambda \cong 10^4$. A pinhole of 5 $\mu$m diameter in the soft X-ray beam and at the source location of the spectrograph reduces intensity and produces a collimated ray of light entering the evacuated instrument ( $10^{-6}$ mbar) and generating a small image on the CCD. The location of the image in $0^{\text{th}}$, $1^{\text{st}}$ and $2^{\text{nd}}$ order on the CCD is recorded for different wavelength settings of the beamline. Figure 3.13 shows this characterization of the spectrograph's dispersion.

Due to the geometry of the setup the dispersion is not perfectly but in in good approximation linear with 0.0170 nm/pixel (1.259 nm/mm) at 13.5 nm. The relative error of this linear fit is less than 1 % in the wavelength region from 10.2 nm to 18.2 nm and below 0.1 % within 12.3 nm to 14.8 nm. Beyond

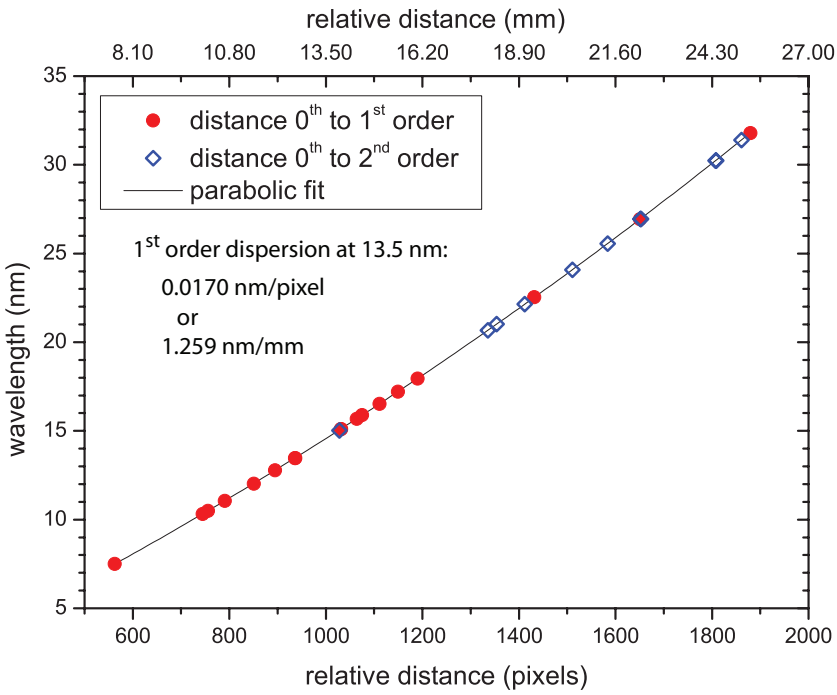


Figure 3.13: Measurement of the distance between different diffraction orders of the grating at various monochromator wavelength settings of the DORIS-III BW3 beam line. Data points from the $2^{nd}$ order have been entered with twice their wavelength to allow a common dispersion fit with the $1^{st}$ order.

 

this, the dispersion curve (Figure 3.13) can be fitted and interpolated with a parabola. Thus, radiation in the 1$^{st}$ order and at a distance $x$ in pixels from the 0$^{th}$ order corresponds to a wavelength

$$\frac{\lambda}{nm} = 2.60 \times 10^{-6} \left(\frac{x}{\text{pixel}}\right)^2 + 1.211 \times 10^{-2} \left(\frac{x}{\text{pixel}}\right) - 0.137 \qquad (3.2)$$

or taking the pixels size of 13.5 $\mu$m into account we obtain for with the distance $x$ in mm

$$\frac{\lambda}{nm} = 1.43 \times 10^{-2} \left(\frac{x}{\text{mm}}\right)^2 + 8.970 \times 10^{-1} \left(\frac{x}{\text{mm}}\right) - 0.137. \qquad (3.3)$$

In linear approximation, this corresponds to the above dispersion of 0.0170 nm/pixel (1.259 nm/mm) at $\lambda = 13.5$ nm. Generally, the dispersion can vary up to 15 % for other source positions and grating angles than applied here. This measurement was conducted with the CCD located in the center of the flange and the 0$^{th}$ order light focusing onto the 125$^{th}$ pixel (1.69 mm) from the edge of the CCD. One should also point out that the linear fit dispersion for a given wavelength in first order will be slightly different from that in the second order of that wavelength. This is due to the non-linearity of the overall dispersion.

**Resolution**

To determine the resolution we use plasma line emission spectra from FEL and optical laser irradiated bulk aluminum (figure 3.14). In the case of optical laser irradiation, the lines have a natural width mainly determined by the plasma temperature. Therefore, the measured line width gives a lower limit for the resolution of the spectrograph where the plasma temperature is high, i.e. for the optical laser produced plasma. However, the FEL generates a relatively cold plasma (∼34 eV [5]) so that we can use those lines to estimate the spectrograph's resolution. They have an average full width half maximum of 0.065 nm between 21 nm and 22 nm. We also observe spectral structures from FEL single pulse scattering at 13.5 nm which have a width of 0.06 nm. That agrees well with the FEL plasma lines at 21 nm and 22 nm and is evidence of the low dependance of the optics' imaging quality on the wavelength in this spectral region. From the average of the spectral widths we estimate that the spectrograph can resolve $\Delta\lambda = 0.063 \pm 0.006$ nm where the error is estimated using the standard deviation of the line widths. This corresponds to a resolution of $\lambda/\Delta\lambda = 330^{+35}_{-30}$ at 21 nm. The average

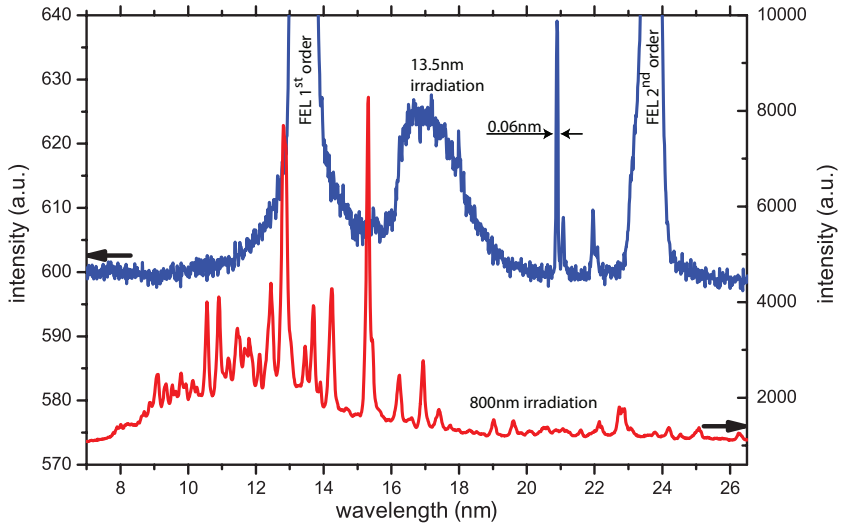


Figure 3.14: Comparison of soft X-ray emission spectra from bulk aluminium irradiated by $4 \times 10^{14}\,\mathrm{W\ cm^{-2}}$ with a photon energy of 91.8 eV (13.5 nm, without filter, top blue line) and $4 \times 10^{15}\,\mathrm{W\ cm^{-2}}$ with a photon energy of 1.6 eV (800 nm, using a 200 nm zirconium-filter, bottom red line). From [2].

line width for the optical laser generated plasma is $\Delta\lambda_{OL} = 0.13 \pm 0.03\,\mathrm{nm}$, broader due to the higher plasma temperature. Figure 3.15 shows the sharpness of various emission lines in terms of $\lambda/\Delta\lambda$ for the optical laser and FEL generated plasma spectra from figure 3.14. Furthermore, we observed no significant change in resolution when rotating the grating. The dependance of the angle between focal plane and CCD on the grating rotation seems to be overcompensated by the large depth of field of the imaging system. An indication for the large depth of field is also that we observe no resolution change when varying the spectrograph source distance within approximately $\pm 1\,\mathrm{cm}$ around the optimum position.

### Throughput

Optimizing the spectrograph design for efficiency requires to maximize a figure of merit which is composed of the acceptance angle and the efficiency of the components. Here, we use the throughput $t(\lambda)$, defined by the wavelength-dependent ratio of photons, delivered to the detector, to isotropically emitted source photons. It is composed as

$$t(\lambda) = \frac{\Omega}{4\pi} \times m(\lambda) \times g_{1st}(\lambda)$$

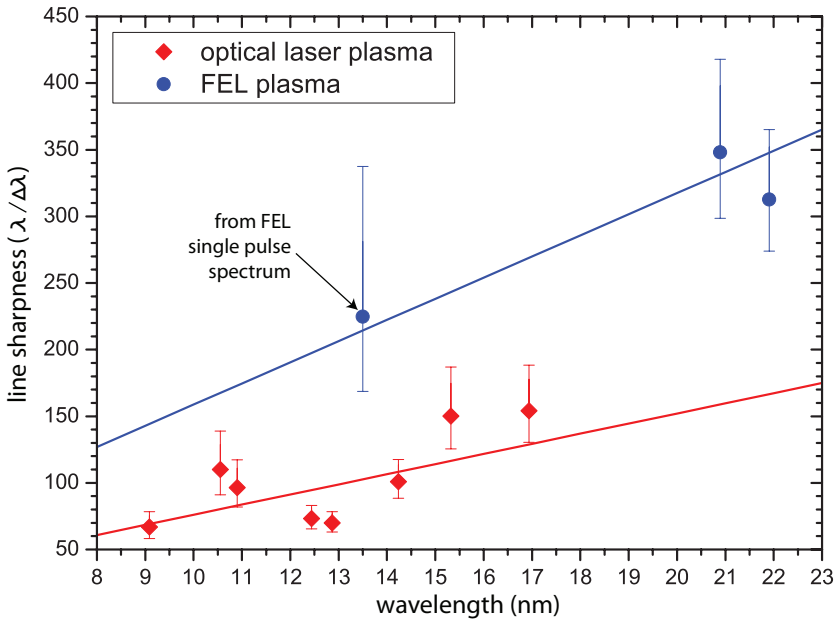


Figure 3.15: Sharpness $\lambda/\Delta\lambda$ of different optical laser (red diamonds) and FEL (blue circles) generated aluminium plasma lines. The wavelength dependent resolution of the spectrograph can be estimated from sharpness of the FEL generated plasma line emission.

with no filters used and where $\lambda$ is the wavelength, $\Omega$ the acceptance solid angle, $m(\lambda)$ the mirror reflectivity, and $g_{1\mathrm{st}}(\lambda)$ the gratings first order absolute efficiency. Table 3.1 compares this value for various types of spectrographs at $\lambda = 13.5\,\mathrm{nm}$.

| Various spectrographs | $\Omega$ (sr) | $t\,(13.5\,\mathrm{nm})$ |
|---|---|---|
| HiTRaX (imaging toroidal mirror and VLS reflection grating) | $1.9 \times 10^{-3}$ | $2.9 \times 10^{-5}$ |
| Non-imaging spherical grating ($40 \times 100\,\mathrm{mm}^2$, 5 m radius), 350 mm from source, Rowland geometry (similar [165, 166]) | $\sim 2 \times 10^{-3}$ | $\sim 2 \times 10^{-5}$ |
| Non-imaging 1200 lines/mm VLS reflection grating [160, 161] | $1.2 \times 10^{-3}$ | $9.6 \times 10^{-6}$ |
| Imaging toroidal mirror and transmission grating [147] | $4.1 \times 10^{-4}$ | $2.6 \times 10^{-6}$ |
| Pinhole ($100\,\mu$m) camera with 1500 lines/mm grating [167], image distance 20 cm, and no magnification (e.g. [168]) | $2.0 \times 10^{-7}$ | $1.6 \times 10^{-9}$ |

Table 3.1: Comparing different spectrographs for acceptance solid angle and throughput at 13.5 nm wavelength.

The wavelength-dependent efficiency of the spectrograph's components is shown in Figure 3.16. Each photon reaching the CCD generates $\sigma(\lambda)$ counts, where

$$\sigma(\lambda) = \frac{hc}{\varepsilon\lambda} \times QE(\lambda) \times ADC(\lambda),$$

with the quantum efficiency $QE(\lambda)$, the electron-hole-pair to count conversion $ADC(\lambda)$, Planck's constant $h$, and the speed of light $c$. The average energy to create an electron hole pair, $\varepsilon$, is 3.6 eV for a typical silicon detector at room temperature. The quantum efficiency and the resulting count-to-source photon ratio for different analog to digital converter (ADC) settings of the employed Princeton Instruments PIXIS-XO: 2KB$^{\mathrm{TM}}$ are also depicted in figure 3.16. ADC1, ADC2 and ADC3 correspond to ADC amplifications at the 2 MHz low noise output where on average 3.56, 1.84 and 0.99 electrons produce one count, respectively. The vendor measured this for our particular camera. Thus, $\eta(\lambda) = t(\lambda) \times \sigma(\lambda)$ is the ratio of counts on the detector to isotropically emitted photons. Using $\eta(\lambda)$ the expected or observed signal in terms of counts on the CCD can be converted into the absolute number of

 

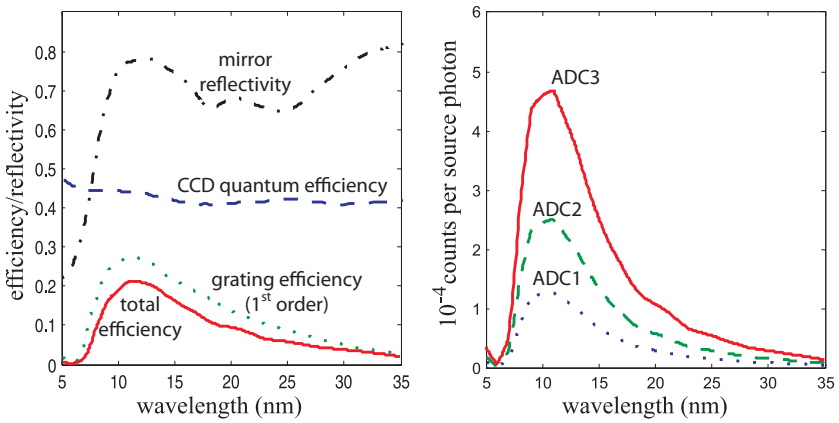


Figure 3.16: Efficiency or reflectivity of the spectrograph components according to the vendor specifications and the total efficiency of the optical elements (left), and the ratio of counts to isotropically emitted source photons (right) for different analog to digital converter (ADC) settings (see text).

isotropical source photons. A minimum amount of photons from the source is necessary to detect a signal. This detection threshold is determined by the signal-to-noise ratio ($S/N$) of counts on the CCD. The root mean square noise on the CCD without illumination is 4.5 counts measured in a box of $50 \times 200$ pixel in the center of the CCD cooled to $\sim$200 K and along its major axis. Thus, the detection threshold for an minimum desirable $S/N = 5$ is overcome with

$$\frac{5 \times 4.5\,\text{counts}}{9.2 \times 10^{-5}\,\text{counts/photons}} = 2.4 \times 10^{5}\,\text{photons}$$

emitted isotropically from a source smaller than the pixel size of the detector ($13.5 \times 13.5\,\mu\text{m}^2$). For larger source sizes and non-imaging spectrographs the number of pixels over which the photons are spread needs to be taken into account. After the experiment, Figure 3.16 can be applied to determine the number of photons emitted from the source into $4\pi$ solid angle and at a specific wavelength range. For example, this can be used to determine the free electron density in a plasma via the intensity of Bremsstrahlung emission [5].

### 3.4.4 Integration into FLASH experiments

The spectrograph was already successfully used in various experiments at FLASH [2, 4]. Due its small dimensions and weight we were able to attach it

to vacuum chambers of various geometries. We achieved ultra high vacuum down to $10^{-8}$ mbar, allowing the simultaneous operation with pressure sensitive instruments like multi channel plates. The vacuum is also sufficiently clean to run a liquid hydrogen jet [2]. Furthermore, the stability of the spectrograph made changing from horizontal to vertical orientation seamless as the dispersion calibration was maintained. The integration into a DN 100 CF manipulator made alignment to the source fast and saved valuable experimental time. The motorized positioning of grating and filter wheel has proven to work repeatable over many cycles. The plasma emission spectra (figure 3.14) with which we determined the resolution are examples of our experimental results.

### 3.4.5 Conclusion

In summary, the tests have shown that the High Throughput, High Resolution Spectrograph for Soft X-Ray Light (HiTRaX) fulfills and even surpasses the design goals for Thomson Scattering plasma diagnostics at FLASH. The dispersion was calibrated and a resolution of $\lambda/\Delta\lambda = 330$ measured at 21 nm. A very high efficiency of the instrument was achieved, so that only $2.5 \times 10^5$ isotropic source photons at 13.5 nm yield the desirable signal to noise ratio of 5. With this, the signal levels can be estimated before the experiment, and absolute photon numbers reconstructed from the experimental data.

In addition, low weight, the motorized grating and filter wheel rotation as well as the compact built within a DN 100 CF manipulator make the spectrograph a versatile instrument and interesting for applications beyond Thomson Scattering. It has been successfully used for various FLASH experiments where its ease of use and integration into different setups have been practically shown. Emission spectroscopy experiments on materials excited with high intensity soft x-ray [4] or particle beams [36, 44] are also being conducted and planned for the future.

## Acknowledgement

We thank the engineers L. Bittner and H. Lärz for their design effort and fruitful discussions as well as the mechanical workshops lead by J. Brehling, B. Klumbies and U. Mänz. We also thankfully acknowledge financial support by the Helmholtzgemeinschaft via the Virtual Institute VH-VI-104, the German Federal Ministry for Education and Research via Project No. FSP 301-FLASH. R.R.F. acknowledges DFG support under Grant No. GRK 1355.

## 3.5 Reference Spectrograph

The single shot FEL spectra in figure 3.4 (page 52) were recorded with a spectrograph based on a spherical variable line space grating (average density 1200 lines/mm) from Hitachi™ [160, 161], located ∼170 cm from the interaction region (figure 3.2) in a setup by Beiersdorfer et al. [146]. It records the light which passes by the liquid hydrogen target as the FEL focus (∼25 $\mu$m) is larger than the target (∼20 $\mu$m). The high intensity of the direct FEL beam makes the use of a 1 $\mu$m Mylar filter foil necessary. A slit further reduces intensity and acts as a differential pumping stage. Furthermore, the slit increases the spectrograph's resolution achieving $\lambda/\Delta\lambda \approx 200$, estimated from the single pulse spectral structures. However, longer integration times showed spectra with substantially lower resolution which is accounted to mechanical vibrations in support structure of this particular spectrograph. Therefore, the recorded spectra could not be used as a kernel to deconvolve the Thomson scattering signal.

## 3.6 Temporal Overlap via Plasma Critical Surface Imaging

First steps towards pump-probe experiments with optical pump and FEL probe radiation were made. To conduct such experiments one first needs to spatially and temporally overlap pump and probe beams with the target. Spatial overlap can be achieved by aligning the reduced intensity FEL and 800 nm spots on a cerium doped $Y_3Al_5O_{12}$ (Ce:YAG) crystal. The crystal is removed once spatial overlap has been established.

Temporal overlap with fs resolution is more difficult to obtain. In a first attempt we had successfully used the generation of side bands in an electron time of flight spectrograph when the soft x-ray and optical pulses overlap. We used a setup similar to [169]. However, the time of flight must be close to the interaction point, which can obstruct other instrumentation and the occupied flange is not available for vacuum pumping.

To overcome this, we transferred a shadowgraphy based technique used with optical lasers to the soft x-ray regime. We position a movable glass slide in the target region, attenuate the 800 nm laser with a neutral density filter of known thickness, and defocus the 800 nm beam by moving a lens already present in the beam path. With this, we backlight an FEL generated plasma on the glass surface. The defocused and attenuated optical laser does not further damage the target. If the FEL plasma is present when the optical laser pulse reaches the glass then the 800 nm laser is reflected by the plasma

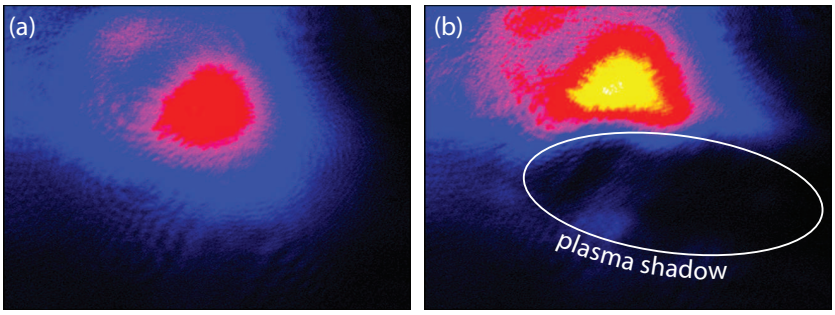


Figure 3.17: Image of the slightly defocused 800 nm spot transmitted through the glass target when it impacts the glass before (a) and after (b) the focused FEL beam. In the latter case (b), the shadow of the plasma critical surface can be seen.

critical surface. This effect can be observed in transmission and by imaging the glass surface onto a CCD (figure 3.17). If the optical laser pulse arrives at the same time or later than the FEL pulse the plasma critical surface shade will be visible in transmission. The delay of the 800 nm laser can be adjusted with a delay line. Iteratively scanning the delay while observing the transmitted signal for many pulses allows us to find the temporal overlap. Figure 3.18 illustrates this process.

Each pulse must hit a new spot on the glass slide as the FEL leaves permanent damage which distorts the transmitted light. Therefore, the glass target is mounted on a manipulator and shifted between pulses (figure 3.2). To facilitate the procedure, FEL and optical laser were operated with a fast shutter. When temporal overlap is found, the 800 nm focus is reestablished by returning the lens to its original position. The neutral density filter is removed and the optical laser delay has to be compensated for the filter thickness. The accuracy of this method is limited by the duration of the optical laser (150 fs in our case) and by the short time scale temporal jitter of the FEL which is ∼590 fs full width half maximum [152].

Once temporal overlap is found it needs to be maintained as variations in the FEL electron trajectory can lead to ps changes in the arrival time over the course of minutes. This is done using a streak camera which continuously compares the arrival time of optical laser light with bending magnet radiation. The long time scale changes in relative arrival time can then be compensated by the delay line of the optical laser. The fast arrival time jitter of ∼590 fs full width half maximum [152] cannot be compensated. However, the method is sufficiently accurate for future pump-probe experiments related to WDM TS.

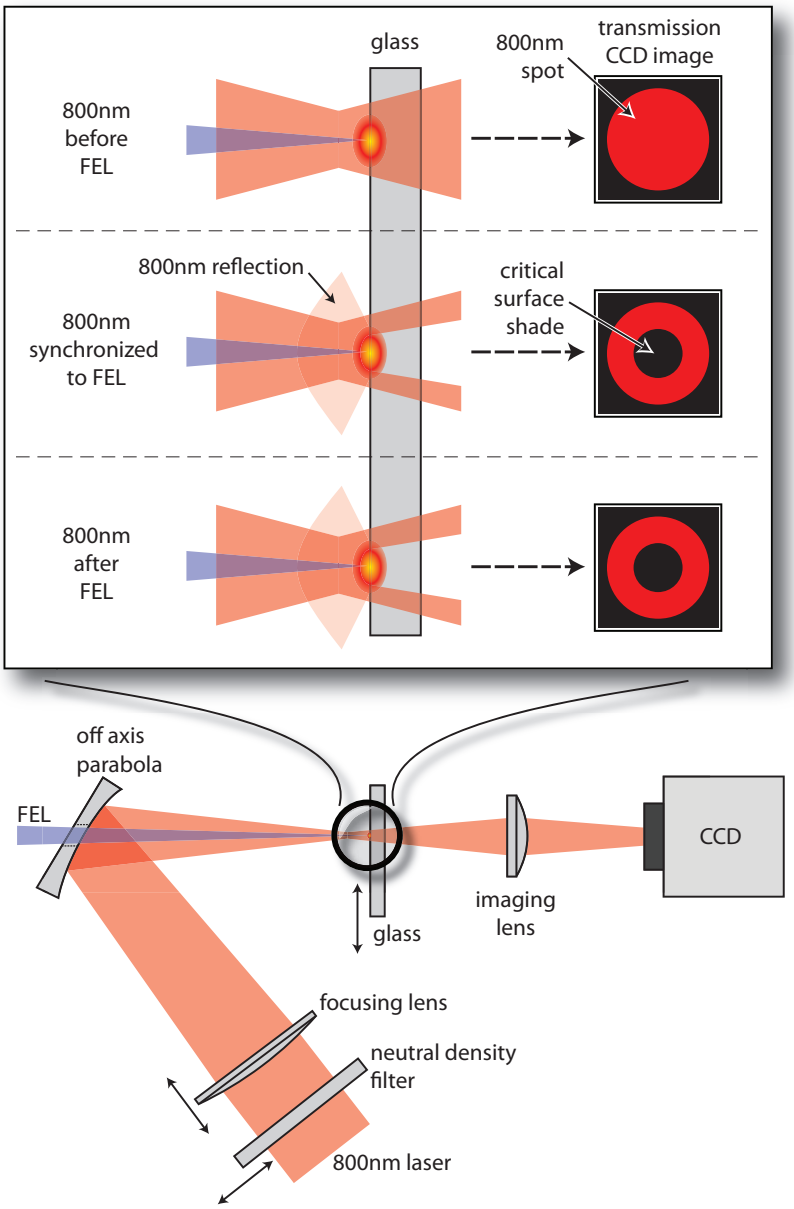


Figure 3.18: FEL irradiation generates a plasma on a glass target. The plasma critical surface can be imaged in transmission by backlighting with 800 nm, thus, finding temporal overlap of the two pulses.

## 3.7 Time of Flight and Classifying Target Irradiation

The FEL pointing was found to be relatively stable when monitoring it with a Ce:YAG fluorescence screen at the center of the chamber. However, the hydrogen jet (chapter 3.3) position fluctuates several 10 $\mu$m around the interaction point on the time scale of seconds, even in its stable operation mode. On top of that, the jet can drift several mm over the course of minutes.

At the current state of development these fluctuations cannot be avoided. Therefore, it is necessary to monitor them in order to sort or compensate the recorded data sets after the experiment. We measure how well the hydrogen sample was hit by the FEL utilizing a field free electron time of flight (TOF). Figure 3.19 shows a typical signal of the multichannel plate (MCP) at the end of the TOF. The Earth's magnetic field has to be compensated to allow for a ballistic electron trajectory in the TOF. This is done by a counter acting magnetic field produced by Helmholtz coils surrounding the experiment. The MCP records the arrival time of the electrons but is also sensitive to Rayleigh scattered light. The strong peak from scattered FEL light (figure 3.19) is followed by damped oscillations in the read out system due to an impedance mismatch. However, the integral light signal remains proportional to the amount of photons impinging the MCP and the detector is not saturated. On top of that, an electron signal is visible $\sim 2 \times 10^{-7}$ s after the light peak. The MCP is located approximately 70 cm from the interaction region, so that the electrons have a kinetic energy of $\sim$35 eV. The electron signal can be identified via the Helmholtz coils. It is only visible if the coils are switched on so that Earth's magnetic field is compensated.

For the analysis of the target irradiation we use the integral signal from the prompt light peak (figure 3.19). If the hydrogen jet was not hit there will be no TOF signal, neither from light nor from electrons. Light scattering by the chamber walls was negligible. If the target was fully hit a maximum signal $I_{max}(N^{pulse})$ will be recorded, which depends only on the actual number of photons $N^{pulse}$ in an FEL pulse, measured by the residual gas ionization detector (or gas monitor detector, GMD) [141]. Further, we assume that the recorded signal from Rayleigh scattering $I_i$ for the $i^{th}$ pulse is proportional to the number of photons that hit the target volume

$$N_i^{target} = \frac{I_i}{I_{max}\left(N_i^{pulse}\right)} N_i^{pulse}. \tag{3.4}$$

Now, the maximum signal $I_{max}(N^{pulse})$ has to be determined. Using the above assumptions

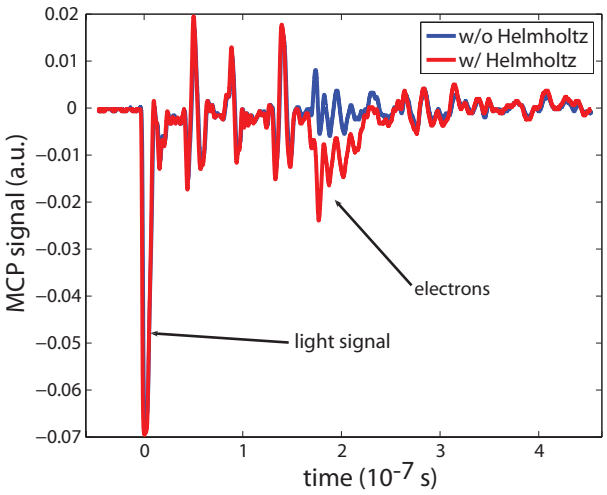


Figure 3.19: Typical TOF signal recorded via the MCP showing a light peak and an electron peak which can be identified through the Helmholtz coils that compensate for the Earth's magnetic field, see text.

$$I_{max}\left(N^{pulse}\right) = mN^{pulse}, \tag{3.5}$$

with the proportionality constant $m$. If $I_i$ over $N_i^{pulse}$ is recorded for many pulses then there will be several full target hits, i.e. data points for which $I_i = I_{max}(N_i^{pulse})$. Depicting $I_i$ over $N_i^{pulse}$ we can fit $m$ and $t$ to the points with maximum signal by eye (red lines, figure 3.20). Then, equation 3.4 determines the effective amount of photons interacting with the target volume. This was done for each data set. A relatively stable hydrogen jet allows for a hit ratio $N^{target}/N^{pulse} \approx 25\,\%$ with an estimated relative error of 15 %.

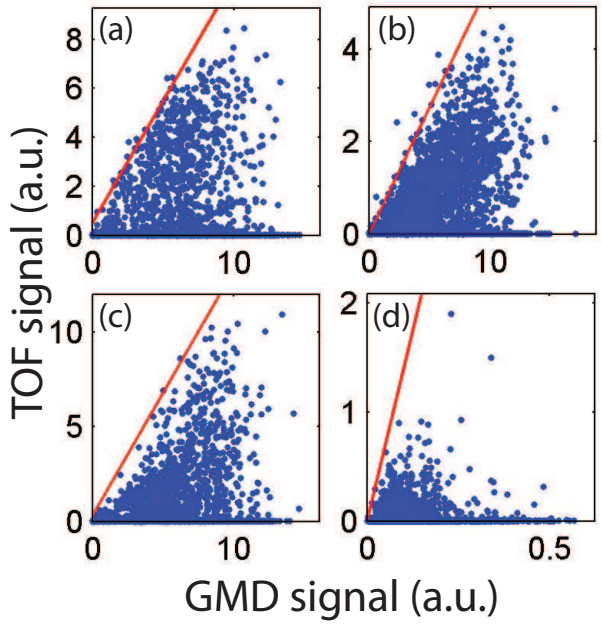


Figure 3.20: Integral TOF light peak signal over the GMD signal representing the FEL pulse energy, both in arbitrary units, for different pulses in a pulse train (a-d), many pulse repetitions (blue dots), and with fits for $I_{max}$ (red lines), see text.

# Chapter 4

# Data Analysis and Interpretation

The publications in this chapter comprise the current main scientific results of this work. They are based on the know-how and equipment described in the previous sections. The experiments range from transmission over emission spectroscopy to Thomson scattering measurements of WDM using FLASH soft x-ray radiation. The different methods allow us to access various time scales and processes during plasma generation and relaxation.

In the publication of chapter 4.1 [4] we observe effects on the time scale of the FEL pulse duration (∼40 fs). The transmission measurement of aluminium foils indicates a saturation of absorption on this time scale and shows a possible mechanism to generate very homogeneous WDM. These experiments have been carried out using the setup depicted in figure 3.3, page 47. Furthermore, radiative recombination radiation is recorded spectroscopically from the same sample element but using the setup of figure 3.2, page 46. From the radiative recombination spectral shape we can measure the sample temperature using, as described in section 2.1.3, page 17. The time scale of this measurement is also in the 40 fs range.

The publication of chapter 4.2 [5] uses plasma emission spectroscopy in conjunction with hydrodynamic simulations to measure the free electron temperature over different time scales. The spectral shape of bremsstrahlung emission allows a temperature measurement on the timescale of few ps (section 2.1.3, page 16). The ratio of emission lines also enables the temperature measurement, but on time scales of the hydrodynamic expansion which occurs over ps to ns (section 2.1.3, page 18). The experiments have been carried out with the setup of figure 3.2, page 46.

The third publication (chapter 4.3 [6]) utilizes the FEL radiation to generate a homogenous warm dense hydrogen plasma and to probe it using

Thomson scattering (chapter 2.3, page 26). This allows us to measure the free electron density and temperature on the time scale of the FEL pulse duration. The absence of elastic scattering indicates via the Debye-Waller factor (section 2.3.2, page 32) that the sample is in a non-equilibrium state where electron and ion temperature are significantly different. The scattering spectra were fit using various scattering codes (section 2.3.2, page 34) to determine the free electron density, temperature as well as an upper limit for the ion temperature. We compare the measurements with simulations using different models for impact ionization (section 2.1.2, page 14) and find that the classic model describes the WDM case more accurately. A video showing the time dependent electron energy distribution from the simulation can also be seen in the appendix (figure A.4).

Each publication focuses on the investigation of specific processes. Combining these pieces allows us to increase our overall understanding of the WDM puzzle.

# 4.1 Turning solid aluminium transparent by intense soft X-ray photoionization [1]

**Abstract**

Saturable absorption is a phenomenon readily seen in the optical and infrared wavelengths . It has never been observed in core electron transitions due to the short lifetime of the excited states involved and the high intensities of the soft x-rays needed. We report saturable absorption of an L-shell transitions in aluminium using record intensities over $10^{16}\,\mathrm{W/cm^2}$ at a photon energy of 92 eV. From a consideration of the relevant time-scales we infer that immediately after the x-rays have passed, the sample is in an exotic state where all the aluminium atoms have an L-shell hole, and the valence band has approximately a 9 eV temperature, while the atoms are still on their crystallographic positions. Subsequently, Auger decay heats the material to the Warm Dense Matter regime, at around 25 eV temperatures. The method is an ideal candidate to study homogeneous Warm Dense Matter, highly relevant to planetary science, astrophysics and inertial confinement fusion.

Saturable absorption, the decrease in the absorption of light with increasing intensity, is a well-known effect in the visible and near-visible region of the electromagnetic spectrum [170], and is a widely-exploited phenomenon in laser technology. Whilst there are many ways to induce this effect, in the simplest two-level system it will occur when the population of the lower, absorbing level is severely depleted, which requires light intensities sufficiently high to overcome relaxation from the upper-level. Here we report on the production of saturable absorption of a metal in the soft x-ray regime by the creation of highly uniform warm dense conditions, a regime that is of great interest in high pressure science [21, 171], the geophysics of large planets [25, 27], astrophysics [172], plasma production and inertial confinement fusion [33]. Further, the process by which the saturation of the absorption occurs will lead, after the x-ray pulse, to the storage of about 100 eV/atom which in turn evolves to a warm dense state. This manner of creation is unique as one requires intense, sub-picosecond, soft x-rays. As such, it has not hitherto been observed in this region of the spectrum, owing both to the lack of high intensity sources, and the rapid recombination times associated with such high photon energies. However, with the advent of new

[1] Peer reviewed paper. This section has been published as: B. Nagler, U. Zastrau, R.R. Fäustlin et al., Nature Physics [4] © 2009 Macmillan Publishers Limited

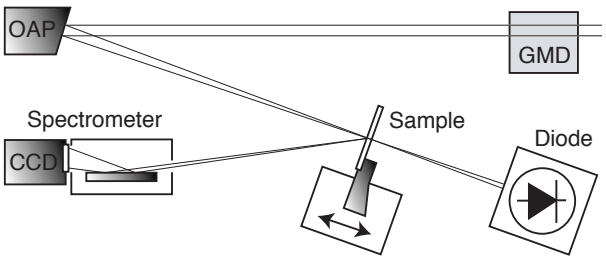


Figure 4.1: A schematic diagram of the experimental setup. The energy of the incoming beam is measured by the Gas Monitor Detector (GMD). The beam is focused with an Off-Axis multilayer coated Mo/Si Parabola (OAP) onto the sample. The transmitted energy is measured by a silicon photodiode.

4th-generation of x-ray light sources, including the Free-electron LASer in Hamburg (FLASH) [15], soft x-ray intensities that have previously remained the province of high power optical lasers can now be produced. Experiments at such high intensities using gas jets have already exhibited novel absorption phenomena [173], and the possibility of irradiating solid samples with intense soft and hard x-rays has aroused interest as a possible means of producing warm dense matter (WDM) at known atomic densities [174, 175].

We present the first measurements of the absorption coefficient of solid samples subject to sub-picosecond soft x-ray pulses with intensities up to and in excess of $10^{16}$ W cm$^{-2}$, two orders of magnitude higher than could previously be obtained. The experiment has two phases: the first occurs during the 15 fs FEL pulse while the second occurs after the pulse. During the first phase the sample absorbs predominantly via inner L-shell photoionization. As the pulse intensity is increased the rate of photoionization surpasses the recombination rate so that the inner-shell absorbers are severely depleted, leading to a saturation of the absorption, (i.e., the aluminium becomes highly transmissive). In the second phase the photoionized electrons decay by two paths, radiative and Auger (radiationless) decay. In principle the former provides spectral information on the temperature of the valence band while the latter transfers energy to the valence electrons that is effectively stored for times of order of several picoseconds (the electron-phonon coupling time). We observe the first phase by measuring the transmission of the pulse over a wide range of fluences. In separate experiments, covering only the lowest fluences used, we have observed the second phase by spectroscopy.

The experiment, shown in schematic form in Fig. 4.1, was performed using FLASH operating at a wavelength of 13.5 nm, i.e. a photon energy of

92 eV. The laser produced pulses of radiation containing between 10 and 50 $\mu$J per pulse in a pulse length of order 15 fs [15] at a repetition rate of 5 Hz. The highly-collimated beam of diameter 5 mm was focused onto solid samples using a Mo/Si multi-layer-coated off-axis parabola with a focal length of 269 mm, and reflectivity of 48%. Focal spot sizes were determined to be 1.5$\mu$m at best focus by using Nomarski optical microscopy and atomic force microscopy to look at damage craters induced by the radiation on poly(methyl methacrylate) (PMMA) [176]. The aluminium samples were placed at nine different positions from best focus, with the FWHM diameter of the laser spot varying from 1.5 $\mu$m at best focus, up to 45 $\mu$m. The energy within each pulse was measured with a gas-monitor detector (GMD) [141]. By variation of both the sample position and laser energies, three orders in magnitude of laser fluence were scanned. The transmission of 53 nm thick aluminium was recorded as a function of laser fluence using a silicon photodiode, which was calibrated with the GMD energies in the absence of a sample. The calibration shows a linear correlation of the GMD signal with respect to the photodiodes. However, this measurement shows a $\pm$10% shot-to-shot error, which limits the accuracy of the measured absorption to $\pm$10% on a shot-to-shot basis. Statistically larger variations between GMD and photodiode readings were found for the lowest beam energies ($\leq$10$\mu$J), and such unusually low energy shots are excluded from the analysis.

With an unexposed region of the Al sample in place the transmission is measured by comparing the energies recorded by the calibrated photodiode and GMD for every shot. Transmission as a function of fluence is shown in Fig. 4.2. Saturable absorption can readily be seen in the experimental data, with an increase in transmission from 15% at the lowest fluence of 0.3 J cm$^{-2}$, to 65% at a fluence of $2 \times 10^2$J cm$^{-2}$. Given a pulse length of 15 fs, these limits correspond to irradiances of $2 \times 10^{13}$ W cm$^{-2}$ and $1.5 \times 10^{16}$ W cm$^{-2}$ respectively.

A theoretical model that explains this increase in transmission with fluence can be constructed by considering the absorption mechanisms and relaxation timescales pertinent to these extreme conditions. At standard temperature and pressure, solid aluminium has a filled-shell ionic core ($1s^2 2s^2 2p^6$) with the three free electrons (coming from the $3s^2$ and 3p atomic electrons) in the valence band. As such, it has a relatively deep L-edge. The $L_{III}$ and $L_{II}$ edges lie below the photon energy, at 72.7 and 73.1 eV respectively, whereas the $L_I$ lies at 117.8 eV [72]. Experimental values for the absorption coefficient of cold aluminium are well known in this region [72]. The contribution due to free-free absorption (i.e. due to the valence electrons) in this region is very small compared to the photoionization, and we determine values for the photoionization absorption coefficient and the free-free coefficient as 27 $\mu$m$^{-1}$

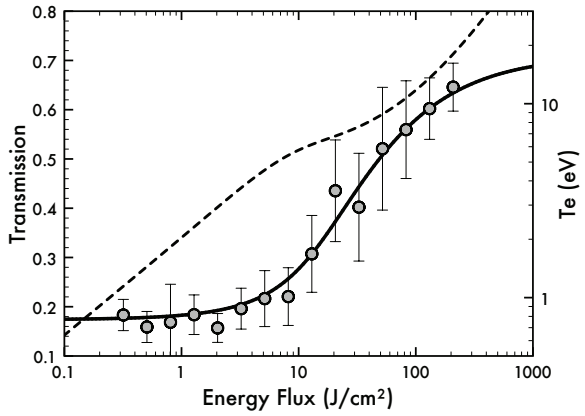


Figure 4.2: Al transmission as a function of fluence. The circles are the experimental data points with a $1\sigma$ error bar, the solid line is the theoretical prediction (see text). The dashed curve is the predicted electron temperature in eV (right Y-axis) in the valence band after the FEL pulse has passed, but before the L-shell holes are filled and the Auger recombination heats the band further.

and 0.2 $\mu$m$^{-1}$ respectively for cold Al [177]. Therefore, for photons of energy 92 eV, almost all of the absorption is due to photoionization of L-shell electrons. At high intensities the fraction of aluminium atoms with photoionized L-shell electrons is high, leading to depletion of L-shell absorption: after an electron is ejected from the L-shell of an atom, the L-edge of that particular atom will increase due to reduced screening. The energy needed to eject a second L-shell electron is calculated to be 93 eV [178], which is confirmed by measurements of Auger energies [178, 179]. Therefore, the FEL (at 92.5 eV) will not be able to create a second L-shell hole; the photoionization quenches and the absorption coefficient is heavily reduced to the value of the free-free absorption. Once an electron is ejected from the L-shell, the hole will be refilled via either radiative decay or the dominant Auger decay. However, the total lifetime of such an L-shell vacancy (which is much shorter than the radiative lifetime) is estimated to be around 40 fs [66], i.e. long compared with the FLASH pulse length, but still short compared with any electron-phonon coupling time, or hydrodynamic motion. Thus, the loss of L-shell electrons during the initial part of the FLASH pulse results in reduced absorption during the rest of the pulse – an effect that is negligible at previously accessible soft x-ray intensities.

We can calculate the absorption of the FEL pulse versus its intensity by keeping track of the densities of the unexcited and photo-excited aluminium cores as the pulse propagates through the foil, and scaling the bound-free and free-free contributions to the absorption accordingly. Thermal ionization of the L-shell does not occur, as it requires a temperature above 10 eV at

solid densities [180]. The resultant transmission as a function of fluence is plotted alongside the experimental data in Fig. 4.2. Since the surface of Al foils readily oxidizes, we assume a 10 nm layer of aluminium oxide formed on either side of the foil [181], which matches both our data at the lowest fluence and transmission measurements performed on the same sample at a synchrotron facility (ALS) with the tabulated cold absorption of aluminium [72]. The theoretical model shows excellent agreement with the experiment.

The photo-excited electrons have an energy of order 20 eV above the original Fermi energy. Measured inelastic scattering lengths for such electrons in aluminium are between 5-10 Å, [182] corresponding to time-scales of order 0.85 to 1.7 fs, in good agreement with calculations based on electron gas dielectric theory [183]. Thus the photo-excited electrons rapidly lose their energy and thermalize with the initial cold valence electrons on a time-scale considerably shorter than the FLASH pulse. Since this electron thermalisation time is short compared with the pulse length and Auger decay time, both the electron temperature and electron density immediately after the passage of the FLASH pulse can be calculated. The electron temperature is calculated by assuming that the excited electrons, which have a kinetic energy equal to the photon energy minus the energy of the bottom of the valence band, thermalize with the other valence electrons. This predicted electron temperature after the FLASH pulse has passed is plotted as a function of fluence in Fig. 4.2. We note that even at the highest fluences, where we expect to have 4 electrons per atom in the band, we estimate that the electron temperature at the end of the passage of the pulse is only of order 9 eV.

Subsequently, L-shell holes will be filled with valence band electrons. The dominant mechanism here will be Auger recombination (the radiative yield is only 0.2% [66]), which will heat the valence band electrons, as each Auger-electron will receive about 70 eV of energy. Therefore over the lifetime of the excited L-shell state, we calculate that the electron temperature will increase from about 1 eV to approximately 2 eV for the lower fluences in Fig. 4.2, and from 9 eV to 25 eV for the highest fluences.

Information about the electron distribution (and hence temperature) in the valence band can be inferred from soft X-ray emission spectra. We have measured such spectra in separate experiments corresponding to the lower end of the fluence regime shown in Fig. 4.2. In these experiments, performed with a different setup and a 29 $\mu$m focal spot [5], the integrated spectra of 1800 shots were measured (see Fig. 4.3). The radiative recombination of electrons from the valence band to the $L_{III}$ or $L_{II}$ levels results in emission that ranges in energy from approximately 62 eV (the energy difference between the L levels and the bottom of the valence band) to a thermally broadened

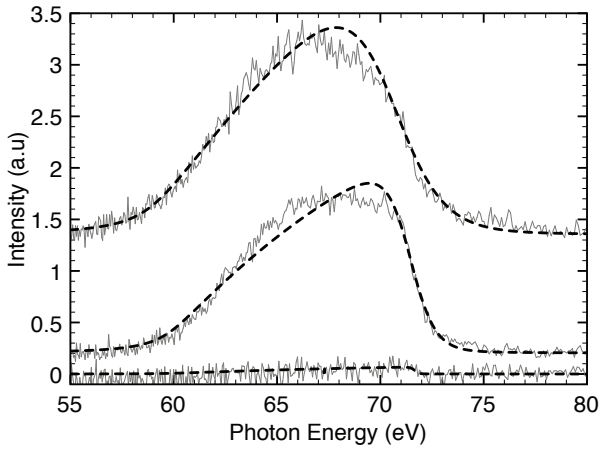


Figure 4.3: Experimental soft x-ray emission spectrum (solid lines) of solid Aluminium for fluences of $0.6\,\mathrm{J\,cm^{-2}}$, $0.3\,\mathrm{J\,cm^{-2}}$ and $0.04\,\mathrm{J\,cm^{-2}}$. Spectra are fitted (dashed lines) using (4.1) where we also include electron collision and Auger level broadening [17], resulting in temperatures of respectively 1.2 eV, 0.5 eV and 0.1 eV. Spectra are offset for clarity.

region at an energy corresponding to the difference between the Fermi energy and the L-shell – an energy of around the L-edge energy at 73 eV.

The lineshape of the emission can be written as [184]:

$$I(E) \sim \omega^3\, P(E)\, g(E)\, f_{T_e}(E), \tag{4.1}$$

with $\omega$ the emission frequency, $P(E)$ the square of the relevant transition matrix element, $g(E)$ the free-electron density of states (DOS) and $f_{T_e}(E)$ the Fermi function for electron temperature $T_e$. In Fig. 4.3. experimentally recorded spectra are compared with theory based on equation (4.1), where we also take Auger broadening and broadening due to electron collisions into account [17].

The soft X-ray emission is here seen to arise from the aluminium valence band from which we infer that the sample is still at solid density and the electrons at a temperature that can be estimated by the slope of the spectra on the high energy edge. In this way the electron temperature is inferred to be 1.2 eV, 0.5 eV, and 0.1 eV for fluences of respectively $0.6\ \mathrm{J\,cm^{-2}}$, $0.3\ \mathrm{J\,cm^{-2}}$, and $0.04\ \mathrm{J\,cm^{-2}}$ – temperatures which are broadly in agreement with those calculated for the lower end of the fluence regime shown in Fig. 4.2. In fact they are slightly lower than the calculated temperatures, which may be due to the fact that the temperature is not uniform as a function of depth within the sample in this unsaturated regime. Evidently the collection of XUV spectra at higher irradiances in future experiments affords the potential to learn directly about the electron temperature in this regime.

Returning to consider the response of the target at the highest fluences, we note that immediately after the passage of the FLASH pulse, where the high transmission indicates that almost every atom has an L-shell hole, we expect the aluminium ions to be close to their original lattice positions: the expected electron-phonon coupling time is over a picosecond [185] and even after receiving energy from the electrons, an aluminium ion with a temperature of a few eV takes more than 50 fs to traverse a lattice spacing. Thus, at the instant the pulse has passed, we can infer that the aluminium is in an exotic, highly-ionized, yet crystalline state, of which the physical properties (e.g. band structure, equation of state, phonon spectrum, etc.) are largely unknown. How this system will subsequently evolve into equilibriated WDM is still largely an open question, as this depends on electron-phonon coupling times and ion-ion interactions which have yet to be measured for these conditions. Measuring these crucial parameters is beyond the scope of the current work, and clearly one of the key experiments that must be performed with XUV FELs in the future.

The results presented here are of significant interest in the context of the creation of warm dense matter by the irradiation of solid samples by high intensity soft and hard x-ray radiation. Saturating an absorption edge allows for a very uniform heating of a sample: while the front part of the pulse is absorbed and heats the front of the sample, the back of the pulse will pass through this bleached region, heating the back of the sample to nearly the same temperature. For example, at $100\,\mathrm{J\,cm^{-2}}$, 50% of the FEL pulse will be absorbed (see Fig. 4.2), but the temperature difference between the front and the back of the sample is calculated to be only 5%. This compares favourably with experiment where thin samples are heated with high intensity optical lasers. While such experiments have yielded excellent results and increased our understanding of WDM significantly [46, 186], the sample thickness that can be uniformely heated in this way is ultimately limited by the electron ballistic depth of the hot electrons that the laser generates. For example in [46], this ballistic depth is around 110 nm, which would mean that the back of 52 nm Al targets is exposed to only 60% of the energy compared to the front of the target, which will never allow for uniform heating within 5% as in our current experiments. By saturating the absorption edge we have efficiently created uniformly heated warm dense aluminium.

In summary, we have presented the first demonstration of saturable absorption induced by record soft x-ray intensities. These results are consistent with the ejection of an L-electrons from almost all atoms in the sample on femtosecond time-scales. Although each atom receives around 100 eV from the photons, a consideration of the relative timescales of electron-electron inelastic scattering and Auger decay implies that the electrons in the valence

band remain relatively cool before filling the L-shell holes via Auger decay. Soft x-ray emission data obtained at the lower end of the fluence regime shows that in the future more detailed measurements of the electron temperature may be possible. By bleaching the L-edge transition in this way within 15 fs (on a much shorter timescale than the picoseconds calculated to be necessary for electron-ion equilibriation), we infer that we have created a very transient exotic state of highly ionized crystalline matter.

## Acknowledgements

The authors want to acknowledge K. Budil of LLNL for assistance in support in funding. BN is supported by the EU Marie-Curie RTN 'FLASH', SMV by EPSRC/STFC, WM acknowledges support from AWE,KS is indebted to the Slovak Grant Agency for Science for financial support (Grant No. 2/7196/27), LJ, JC, JCh, and VH thank the Czech Ministry of Education (grants LC510, LC528, and LA08024) and Academy of Sciences of the Czech Republic (Z10100523, IAA400100701, and KAN 300100702) for financial support. Technical assistance by A. Aquila, J. Meyer-Illse and E. M. Gullikson (LBNL) during the ALS beamtime is greatly appreciated. Operation of the Advanced Light Source was supported by the Director, Office of Science, Office of Basic Energy Sciences, of the U.S. Department of Energy under Contract No. DE-AC03-76SF00098. The authors from Universität Rostock are supported by the Deutsche Forschungsgemeinschaft within SFB 652. We thankfully acknowledge financial support by the German Federal Ministry for Education and Research via project FSP 301-FLASH, and from MSHE of Poland.The authors gratefully acknowledge support for access to FLASH by DESY and the European Community under contract RII3-CT-2004-506008 (IA-SFS).This work was in part performed under the auspices of the U.S. Department of Energy by Lawrence Livermore National Laboratory under Contract DE-AC52-07NA27344, and in part by supported by grants 08-ERI-002 and 08-LW-004."

# 4.2 Bremsstrahlung and Line Spectroscopy of Warm Dense Aluminum Plasma heated by XUV Free-Electron Laser Radiation [2]

**Abstract**

We report the novel creation of solid density aluminum plasma using free-electron laser (FEL) radiation at 13.5 nm wavelength. Ultrashort pulses were focused on bulk Al target, yielding an intensity of $2 \times 10^{14}\,\mathrm{W/cm^2}$. The radiation emitted from the plasma was measured using an XUV spectrometer. Bremsstrahlung and line intensity ratios yield consistent electron temperatures of about 38 eV, supported by radiation hydrodynamics simulations. This shows that XUV FELs heat up plasmas volumetrically and homogeneously at warm dense matter conditions, which are accurately characterized by XUV spectroscopy.

## Introduction

The physics of warm dense matter (WDM) [121] gains increasing interest because of its location in the transition region from cold condensed materials to hot dense plasmas. WDM states are of paramount importance to model astrophysical objects such as giant planets [27] or brown dwarfs [23]. Furthermore, WDM occurs as a transient state in novel experiments to generate high energy densities in materials, most notably the realization of inertial confinement fusion [33, 187]. First experimental investigations of WDM have been performed, e.g., with shock wave experiments [40] and with laser excited plasmas [41, 42, 45–47].

WDM describes materials at temperatures of several eV at solid-like densities. Its creation and investigation under controlled conditions in the laboratory is a difficult task. Using common optical short-pulse lasers, nonlinear absorption leads to rapid temporal variations, steep spatial gradients, and a broad spectrum of plasma physical processes. Pioneering techniques such as laser-driven shock heating, x-ray heating, ion heating techniques [38, 40, 43, 44, 188] and x-ray Thomson scattering [50] have been developed in order to improve the plasma heating mechanism.

In WDM the electron temperature is comparable to the Fermi energy, i.e., the degeneracy parameter $\theta = k_\mathrm{B}T_\mathrm{e}/E_\mathrm{F}$ is close to unity. Furthermore, the

[2] Peer reviewed paper. This section has been published as: U. Zastrau, C. Fortmann, R.R. Fäustlin et al., Physical Review E [5] © 2008 The American Physical Society

ion coupling parameter $\Gamma = Z^2/4\pi\epsilon_0 k_B T_i \,(4\pi n_i/3)^{1/3}$ is greater than or equal to unity, i.e. the interparticle Coulomb correlation energy is equal or exceeds the thermal energy; $Z$ is the ion charge and $n_i$ is the ion density. Thus, electrons as well as ions exhibit strong temporal and spatial correlations which depend strongly on the plasma parameters, temperature and density.

A proper description of WDM is also a tremendous challenge to many-particle physics. Both the theory for ideal plasmas and condensed matter fail in this regime. Classical plasma theory based on expansions of the correlation contributions in powers of the coupling parameter breaks down since $\Gamma \geq 1$, and strong coupling effects among the various species have to be taken into account. On the other hand, the plasma is too hot to be considered as condensed matter, i.e., expansions in terms of the degeneracy parameter $\theta$ also fail. Thus, the precise knowledge of physical properties as function of the plasma parameters temperature and density is of primary importance.

In this article, we demonstrate that XUV free-electron lasers (FELs) open a new and promising possibility to heat matter volumetrically and homogeneously. Furthermore, we show that XUV bremsstrahlung and line spectroscopy allow the determination of the plasma temperature and free electron density.

## Experimental setup

### Free-electron laser characteristics

The fourth generation light source FLASH (Free-electron LASer in Hamburg) uses the self-amplified spontaneous emission (SASE) principle to generate brilliant XUV pulses [15, 189]. In the experiment, pulses of 91.8 eV photon energy (wavelength $\lambda = 13.5\,\mathrm{nm}$), $(15 \pm 5)\,\mathrm{fs}$ duration were focused to a 30 $\mu$m spot by a carbon-coated ellipsoidal mirror with gracing incidence angle of 3°° and 2 m focal length, as shown in Fig 4.4.

Since the FEL process starts from spontaneous radiation, it shows an intrinsic shot-to-shot pulse energy spread. The relevant distribution of pulse energies for this experiment is shown in Fig. 4.5. The total number of pulses in our measurement was 81 000, including 3% of zero-energy events and a significant fraction of high-energy pulses up to $130\,\mu\mathrm{J}$. The mean value is $48\,\mu\mathrm{J}$, measured at the end of the undulators. Since the beamline transmission is known to be T = 0.68, the average pulse energy at the experiment is $33\,\mu\mathrm{J}$.

 

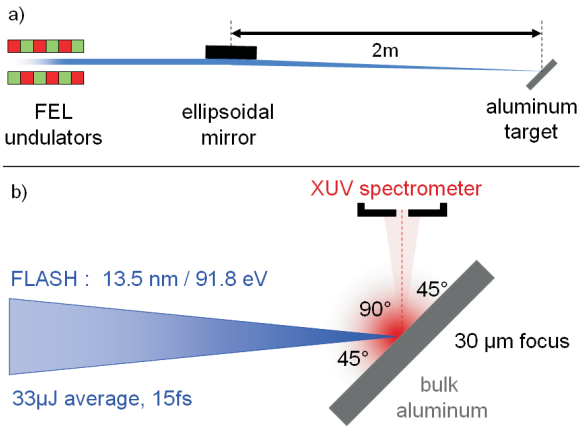


Figure 4.4: Experimental setup. a) The XUV pulses from the FEL undulators are focused by an elliptical beamline mirror on the bulk aluminum target, creating a 30 $\mu$m focus. b) The target is hit under 45° and plasma is created. A high-resolution XUV spectrometer observes the plasma emission under 45° to the surface normal.

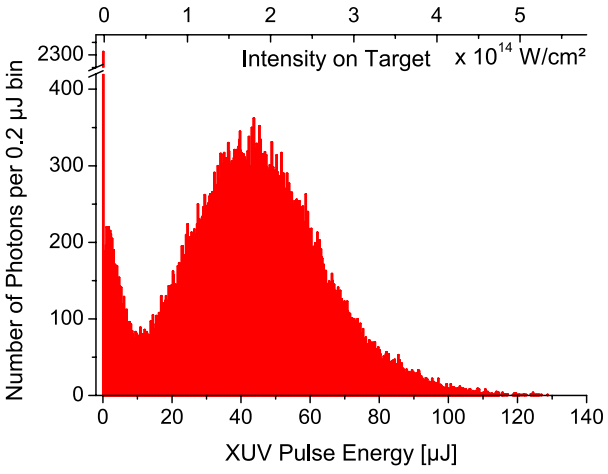


Figure 4.5: Histogram of the energy spread of 13.5 nm XUV pulses generated by Self-Amplified Spontaneous Emission (SASE). Only pulses contributing to the measured spectrum of the performed experiment are shown. The top ordinate shows the corresponding irradiation intensities on target.

### XUV Plasma Spectroscopy

Each pulse irradiates a bulk aluminum target under 45° incident angle, resulting in an average intensity of $2 \times 10^{14}\,\mathrm{W/cm^2}$, see Fig. 4.4. The polarization is linear in the horizontal plane. At the chosen wavelength, the critical density for penetration into the bulk $n_{\mathrm{crit}} = (2\pi c)^2 \epsilon_0 m_{\mathrm{e}}/e^2\lambda^2 = 6.1 \times 10^{24}\,\mathrm{cm^{-3}}$ is about 40 times higher than the valence electron density in cold solid aluminum, $n_{\mathrm{e}} = 1.6 \times 10^{23}\,\mathrm{cm^{-3}}$, therefore the initial absorption length is 40 nm [72]. The pulse energy is deposited in a target volume of $\pi \times (15\,\mu\mathrm{m})^2 \times 40\,\mathrm{nm}$, generating WDM. The number of $10^{12}$ atoms in this volume is in the same order of magnitude as the incident photon number.

At fixed target position, the emission spectrum of about $10^4$ exposures was recorded before moving to a fresh site. Since the very first FEL pulse ablates a few-nanometer thin surface layer, further surface cleaning technique was not necessary. The target was at ambient temperature, and vacuum was kept constant at $10^{-7}$ mbar.

The FEL was run in multibunch operation mode at 5 Hz repetition rate, with 20 bunches per train giving 100 FEL pulses per second. Five separate measurements of different durations adding up to a total interaction time of 13.5 min were performed. Since the individual spectra look identical we assume that plasma formation and emission processes vary very slowly during the measurement.

XUV emission spectra in the region of $6 - 18\,\mathrm{nm}$ were measured with a high throughput spectrometer, featuring a toroidal Ni-coated focusing mirror and a free-standing transmission grating. The spectrometer is described in detail in reference [147]. The spectral resolution was limited to 0.2 nm due to a slightly fluctuating plasma position. A back-thinned XUV CCD camera with $13 \times 13\,\mu\mathrm{m}^2$ pixel size and a quantum efficiency of $\eta = 0.45$ served as detector. From the measured spectra, absolute photon numbers per wavelength interval and solid angle are calculated using the tabulated efficiency of all components.

## Data analysis

Figure 4.6 shows the sum of all spectra in logarithmic scale after correction for the spectrometer throughput and detection efficiency. The error-bars arise essentially from statistical signal-to-noise ratios beside uncertainties of the spectrometer components. The main peak at 13.5 nm stems from Rayleigh scattering of FEL photons by bound aluminum electrons. It is broadened symmetrically by $\pm 0.4$ nm due to artifacts originating from the support grid of the transmission grating. Spectral lines from Al IV and Al V

 

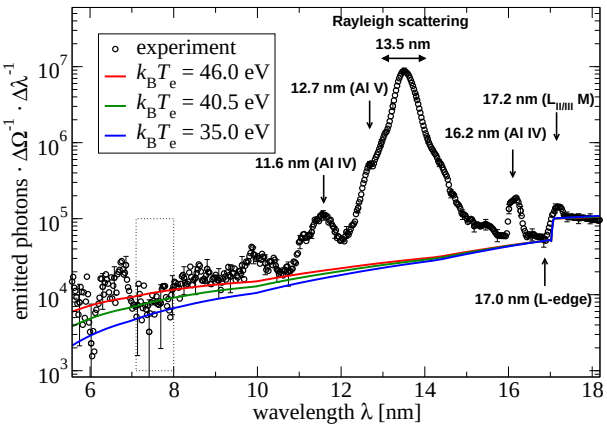


Figure 4.6: Experimental XUV photon spectrum per solid angle $\Delta\Omega$=4 × $10^{-4}$sr and wavelength interval $\Delta\lambda$=0.025 nm (symbols with error bars) and bremsstrahlung calculations for different electron temperatures. The spectrum is corrected for the spectrometer throughput and the detection efficiency.

Table 4.1: List of the spectral lines emitted from the plasma, identified with the NIST database [190, 192].

| Experimental data [nm] | Reference data [nm] | Relative intensity (NIST) | Oscillator strength $f$ (NIST) | Transition |
|---|---|---|---|---|
| $11.6 \pm 0.2$ | 11.646 | 250 | 0.332 | Al IV: $2s^2 2p^6$ -$2s^2 2p^5 (^2p^0_{1/2}) 4d$ |
| $12.7 \pm 0.2$ | 12.607 | 800 | – | Al V: $2s^2 2p^5$ -$2s^2 2p^4 (^1D) 3s$ |
| $16.2 \pm 0.2$ | 16.169 | 700 | 0.247 | Al IV: $2s^2 2p^6$ -$2s^2 2p^5 (^2p^0_{1/2}) 3s$ |
| $17.2 \pm 0.2$ | 17.14 | - | – | $L_{II/III}M$ |

are identified using the NIST tables [190] as listed in Tab. 4.1. The continuum emission is formed by free-free transition radiation (bremsstrahlung) and free-bound recombination radiation. Since the target is heated volumetrically, the continuum emission is partly reabsorbed and we observe a step-like feature at 17.0 nm that is consistent with the absorption $L_{II/III}$-edge [72]. This indicates deep deposition of energy into the target, as expected for XUV photon-matter interaction. The corresponding absorption L-edge at a similar excitation flux was also analyzed in laser excited silicon [191]. Finally, the $L_{II/III}M$-fluorescence line [192] is observed at 17.2 nm.

### Bremsstrahlung

The experimental spectra allow the determination of the plasma parameters using fundamental relations [193]. The electron temperature and density are inferred from the continuum background radiation due to bremsstrahlung. We compare the experimental data to Kramers' law [70]

$$j_{\mathrm{ff}}(\lambda) = \left(\frac{e^2}{4\pi\epsilon_0}\right)^3 n_{\mathrm{e}}^2 \frac{16\pi Z \mathrm{e}^{-2\pi\hbar c/\lambda k_{\mathrm{B}} T_{\mathrm{e}}}}{3 m_{\mathrm{e}} c^2 \lambda^2 \sqrt{6\pi k_{\mathrm{B}} T_{\mathrm{e}} m_{\mathrm{e}}}}\, g_T(\lambda) \qquad (4.2)$$

for the free-free emissivity $j_{\mathrm{ff}}(\lambda)$. Here, $m_{\mathrm{e}}$ is the electron mass and $g_{\mathrm{T}}(\lambda)$ is the wavelength dependent Gaunt factor [194], accounting for medium and quantum effects. It is calculated in Sommerfeld approximation [195]. We assume an average ion charge of $Z = 4$, which is supported by calculations of the relative ion abundances using the code COMPTRA04 [196], see below. In the wavelength range from 7.1 nm to 8.0 nm (marked by the dotted box in Fig. 4.6), we expect no essential contributions from bound-bound and bound-free transitions. Statistical analysis of the data in this range yields 40.5 eV for the temperature with an rms error of ±5.5 eV. Bremsstrahlung spectra for 35 eV, 40.5 eV, and 46 eV are shown in Fig. 4.6. Reabsorption was considered using tabulated opacity data [72], in this way the L-edge at 17.0 nm is reproduced. The height of the L-edge corresponds to a transmission through 40 nm of cold aluminum.

Kramers' law (Eqn. 4.2) depends on the square of $n_e$. From the absolute photon number at $\lambda = 17.0\,\mathrm{nm}$, $N_{\mathrm{photon}} = 51424 \Delta\Omega^{-1}\,\Delta\lambda^{-1}$, we calculate the free electron density using Eq. 4.2 as $n_{\mathrm{e}} = 4.0 \times 10^{22}\,\mathrm{cm}^{-3}$, taking the inferred plasma temperature of 40.5 eV. This value is consistent with radiation hydrodynamics simulations, see below.

### Transition Line Ratio

Independently, the electron temperature can be obtained from the ratio of integrated line intensities $I_\nu$ for the identified transition lines from the Boltzmann distribution [74] as follows

$$\frac{I_1}{I_2} = \frac{\omega_1^3}{\omega_2^3}\frac{f_1}{f_2}\mathrm{e}^{-\hbar(\omega_1-\omega_2)/k_{\mathrm{B}}T_{\mathrm{e}}}\,, \qquad (4.3)$$

with the corresponding photon frequencies $\omega_\nu$ and oscillator strengths $f_\nu$, having in mind that the plasma is optically thin. Here, the Al IV lines (doublets) at $\lambda_1$=16.169 nm and $\lambda_2$ =11.646 nm, with oscillator strengths given in Tab. 4.1, are used. Integration was performed from 15.9 nm to 16.3

 

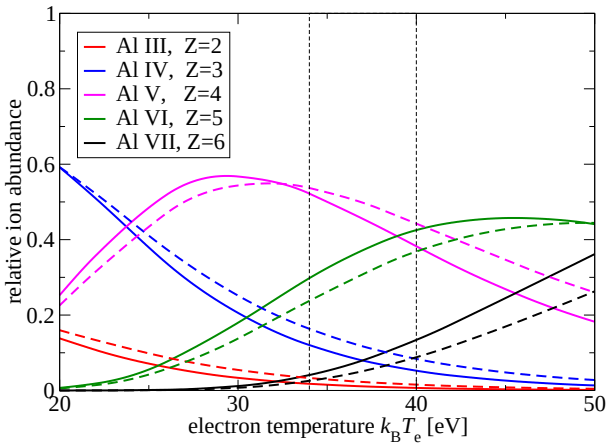


Figure 4.7: Calculation of the relative Al ion species abundance from COMPTRA04 as a function of the electron temperature. Solid line is for Al density $\rho_{\mathrm{sol}} = 2.7\,\mathrm{g/cm^3}$, dashed line $0.5\,\rho_{\mathrm{sol}} = 1.35\,\mathrm{g/cm^3}$.

nm and from 10.8 nm to 11.9 nm after subtraction of the bremsstrahlung continuum, respectively. The resulting temperature is (34±6) eV. Within the error bounds, this is consistent with the temperature inferred by analysis of the bremsstrahlung continuum, so that we can state the plasma temperature with about 38 eV.

A full compliance of line and continuum temperature cannot be expected, since the plasma dynamics affects both emission processes in different ways. At early times after the laser-target interaction, the system is still very dense and the excited levels of the transitions under consideration are possibly dissolved into the continuum. Only after expansion, the excited levels are well defined and radiative transitions take place. Bremsstrahlung, on the other hand, is most relevant at early times due to the $n_e^2$-dependance of its emissivity, see Eq. 4.2. Thus, in the bremsstrahlung emission we expect a higher temperature than in the line spectrum.

### Relative Ion Abundance

The relative abundance of aluminum ions was calculated with the code COMPTRA04 [196]. Results for electron temperatures from 10 eV to 50 eV are shown in Fig. 4.7, assuming solid density $\rho_{\mathrm{sol}} = 2.7\,\mathrm{g/cm^3}$ and $0.5\,\rho_{\mathrm{sol}}$, i.e. slightly expanded. The concentration of ion species for the relevant temperatures between 34 and 40 eV complies with the observed line emission spectrum. At an averaged temperature of 38 eV, the ion fractions of Al IV, Al V, and Al VI take the values of about 7%, 45%, and 46%, respectively. Amounts of Al I-III as well as Al VII and higher are negligible.

All expected spectral lines from Al IV in the observed spectral range are either observed (at 16.2 nm) or covered by the strong FEL signal (at

12.9 nm). For transition details see Tab. 4.1. Weak lines from Al V between 11.9–13.2 nm overlap with the Rayleigh peak and only the 12.607 nm line can be identified. Transition lines from Al VI, which are located between 8.6–10.9 nm, are not significantly present compared to the detector noise. This indicates, that the corresponding high-lying excited levels are dissolved and do not contribute.

Emission lines from Al VII (and higher) are expected to play a significant role only at temperatures exceeding 40 eV, as shown in Fig. 4.7. These lines have also not been found, but have previously been observed in optical laser-matter interaction experiments [197]. This contrast is well understood by scrutinizing the different mechanisms of absorption and ionization in the case of optical light as opposed to the case of XUV photons.

## Discussion

### Different Photon Absorption Mechanisms

In optical laser-matter interaction, dominant absorption mechanisms are multi-photon ionization, nonlinear processes, inverse bremsstrahlung, and resonance absorption [62]. When the critical free electron density of the optical laser is exceeded, most light is reflected and absorption is limited to the skin layer, leaving behind a plasma with steep density and temperature gradients.

For XUV photons, nonlinear absorption is negligible at the considered intensity and resonance absorption is not important since the plasma is undercritical. Thus, "hot" electron production in the keV to MeV range is unlikely. Photo-excitation and inverse bremsstrahlung are the only possible mechanisms. Since there are no prepulses in the FEL case, the deposition of photons starts in a cold target and the energy is distributed volumetrically and homogeneously throughout the interaction zone.

A change in the polarization of the FEL (e.g. using circularly polarized light) could lead to less heating and certainly to a reduction in the scattered intensity (Rayleigh peak). For atomic systems, a systematic decrease in the photo-ionization yield has been reported upon changing the laser's polarization [198], while such studies for solid state targets at XUV conditions remain to be done.

The novel plasma production mechanism presented here, takes advantage of photons exceeding the $2p$ level binding energy of 72.8 eV. In particular, a $2p$ bound electron is photoionized with a cross section of $\sigma_{\mathrm{PI}} = 7\,\mathrm{Mbarn}$ [72]. This electron is transferred into the conduction band, leaving behind a hole in the $2p$-shell. For the partially ionized aluminum the photoabsorption cross-

 

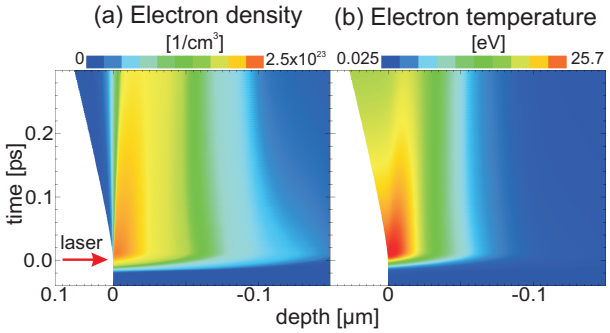


Figure 4.8: HELIOS simulation results for the electron density (left) and electron temperature (right) as a function of time and radius.

section increases below the $L_{\mathrm{II/III}}$-edge slightly with temperature [142]. Due to their high excess energy of about 20 eV, further electrons at lower energies are excited via impact ionization and Auger processes [121]. The electrons equilibrate at a temperature of several eV within hundred femtoseconds [53, 199], forming typical WDM. During this time, electrons can also recombine with the $2p$-holes by emitting fluorescence radiation at 17.2 nm wavelength. This state of matter cools down on a picosecond timescale by energy transfer to the lattice via electron-phonon scattering [193].

## Hydrodynamics Simulation

To illustrate the hydrodynamic processes and to estimate the electron temperature, 1D radiation hydrodynamics simulations using HELIOS [78] have been performed. HELIOS features a Lagrangian reference frame, i.e., grid moves with fluid, separate ion and electron temperatures, and flux-limited Spitzer thermal conductivity. It allows the deposition of laser energy via inverse bremsstrahlung as well as bound-bound and bound-free transitions, using a SESAME-like equation of state. Per atom, 2.6 conduction band electrons were assumed to contribute to the laser absorption [200]. The results are shown in Fig. 4.8. On the timescale of the FEL pulse, both electron density and temperature rise up to values of $n_\mathrm{e} \simeq 10^{23}\,\mathrm{cm}^{-3}$ and $k_\mathrm{B}T_\mathrm{e} \simeq 26\,\mathrm{eV}$, respectively, without any steep gradient. These values are in good qualitative agreement with the results for $n_\mathrm{e}$ and $T_\mathrm{e}$ obtained by the spectral analysis.

This hydrodynamics simulation uses the average pulse energy of 33 $\mu$J on target as an input parameter. As discussed above, Fig. 4.5 illustrates that a significant fraction of pulses have much higher pulse energies up to 130 $\mu$J. Since the free-free emissivity (Eqn. 4.2) depends strongly non-linear both on electron temperature and density, we expect the observed radiation to be rather dominated by the high-energy fraction of the XUV pulses than by its average value. This finally explains the slight underestimation of the electron

temperature in the hydrodynamics simulation compared to the experimental results.

Additionally, the simulation shows that these WDM conditions exist for about 200 fs, at almost constant plasma density and temperature, and hydrodynamic motion is negligible [201]. Plasma expansion as well as electron diffusion to the cold matter of the bulk target and heat conduction becomes important during the first several picoseconds [202], while the density decreases about a factor of two, influencing the relative abundance of ion species only slightly, as demonstrated in Fig. 4.7.

## Summary and concluding Remarks

The capability of XUV FEL radiation to create WDM by interaction with a solid aluminum target was demonstrated for the first time. The analysis of the XUV line and continuum emission spectra yield an electron temperature of $(34 \pm 6)$ eV and $(40.5 \pm 5.5)$ eV, respectively. The observed line spectrum is compatible with predicted ion abundances. Together with radiation hydrodynamics modeling, we get a sound picture of complex XUV laser–plasma interaction dynamics. The simulations confirm the volumetric heating of the target without strong gradients. Our results provide new complementary information to results that were reported for optical laser-matter interaction [197].

Further and detailed studies of WDM will include spatially and temporally resolved experiments to determine electron temperature and density. For this regime, novel diagnostic techniques such as x-ray interferometry [39, 203] and x-ray Thomson scattering [13, 51, 53] have been developed. In combination with these techniques, the XUV FEL will be a unique platform for WDM investigations. This will be important for shock wave physics, applied material studies, planetary physics, and inertial confinement fusion, and other forms of high energy density matter generation.

We thankfully acknowledge financial support by the German Helmholtzgemeinschaft via the Virtual Institute VH-VI-104, the German Federal Ministry for Education and Research via project FSP 301-FLASH, and the Deutsche Forschungsgemeinschaft DFG via the Sonderforschungsbereich SFB 652. TL acknowledges financial support from the DFG under Grant No. LA 1431/2-1, RRF received DFG funds via GRK 1355. The work of SHG was performed under the auspices of the U.S. Department of Energy by Lawrence Livermore National Laboratory under Contract DE-AC52-07NA27344. SHG was also supported by LDRDs 08-ERI-002, 08-LW-004, and the Alexander-von-Humboldt foundation. The work of GG was partially supported by the Science and Technology Facilities Council of the United Kingdom. Finally, the

authors are greatly indebted to the machine operators, run coordinators, scientific and technical teams of the FLASH facility for enabling an outstanding performance.

## 4.3 Observation of ultrafast non-equilibrium collective dynamics in warm dense hydrogen[3]

**Abstract**

We investigate ultrafast (fs) electron dynamics in a liquid hydrogen sample, isochorically and volumetrically heated to a moderately coupled plasma state. Thomson scattering measurements using 91.8 eV photons from the free electron laser in Hamburg (FLASH) show that the hydrogen plasma has been driven to a non-thermal state with an electron temperature of 13 eV and an ion temperature below 0.1 eV, while the free electron density is $2.8 \times 10^{20}\,\mathrm{cm}^{-3}$. For dense plasmas, our experimental data strongly support a non-equilibrium kinetics model that uses impact ionization cross sections based on classical free electron collisions.

The investigation of Warm Dense Matter (WDM) is one of the grand challenges of contemporary physics [21]. WDM is a plasma state characterized by moderate-to-strong inter-particle coupling which takes place at free electron temperatures of several eV and free electron densities around solid density [21]. It is present in many physical environments, such as planetary interiors [25, 27], gravitationally collapsing protostellar disks, laser matter interaction and particularly during the implosion of an inertial confinement fusion capsule [33]. While in the astrophysical context WDM exists under stable conditions, in the laboratory it is achieved only as a transient state bridging condensed matter and hot plasma regimes. Here, we report on the first investigation of the non-equilibrium transition of hydrogen from a liquid to a moderately coupled plasma on the fs time scale, induced by highly intense soft x-ray irradiation. This is an important step towards the investigation of strongly coupled plasmas which are within reach of current light sources such as LCLS. Our measurement enables unprecedented direct tests of non-equilibrium statistical models beyond mean field theories in a regime where collision and relaxation processes are dominant [22, 47, 49].

The use of x-ray scattering for the investigation of dense, strongly-coupled plasmas was successfully demonstrated in the past decade [22, 34, 49–52]. This technique is the x-ray analog of optical Thomson scattering (TS) [48] and enables the experimental determination of plasma parameters in dense

[3]Peer reviewed paper. This section has been published as: R.R. Fäustlin, Th. Bornath et al., Phys. Rev. Lett. accepted [6] © 2010 American Physical Society

systems where optical light cannot penetrate. While previous experiments were carried out using high-energy laser facilities, the advent of soft and hard x-ray free-electron lasers (FELs) makes ultrashort high brightness beams available for this type of research [13, 53]. This letter reports on ultrafast heating of liquid hydrogen and TS measurement of dense plasma parameters using soft x-ray FEL radiation. For the first time, non-equilibrium distributions are observed and the underlying relaxation dynamics are compared with kinetic models showing electron relaxation times in the order of 20 fs, thus, shorter than the pulse duration.

The scattering taking place is collective TS, which is characterized by a spectrally blue and red shifted response due to collective electron motion, plasmons, and nearly elastic scattering due to ion acoustic fluctuations [22, 204]. The frequency shift $\omega$ of the plasmons with respect to incident radiation is described by the dispersion relation $\omega^2 \approx \omega_p^2 + 3T_e k^2/m_e$, their intensity ratio by the detailed balance relation $S_{\mathrm{blue}}/S_{\mathrm{red}} = e^{-\hbar\omega/T_e}$, where $\omega_p = \sqrt{n_e e^2/m_e\varepsilon_0}$ is the plasma frequency, $k$ the photon wave vector change, $m_e$, $n_e$, $T_e$ electron rest mass, density and temperature (in eV), $e$ the electron charge, and $\varepsilon_0$ the vacuum permittivity. Therefore, from the measured asymmetry and frequency position of the plasmons we can determine the electron temperature via detailed balance and density via the above dispersion relation.

Our experiments have been performed at DESY using the Free Electron Laser in Hamburg (FLASH) [15, 140] at a photon energy of 91.8 eV. FEL radiation with 5 Hz pulse repetition rate, average pulse energy on target of 15 $\mu$J and duration of $\sim$40 fs is focused to a 25 $\mu m$ spot using an elliptical mirror, yielding intensities of $\sim 8 \times 10^{13}\,\mathrm{Wcm^{-2}}$. The energy of each pulse is measured using a residual gas ionization detector [141] and fluctuates less than 10 %. Figure 4.9 shows a schematic of the experiment. The FEL pulses hit the liquid hydrogen jet which has a diameter of 20 $\mu m$, an atomic density of $4.2 \times 10^{22}\,\mathrm{cm^{-3}}$, and a temperature of 2 meV, prepared in a liquid helium cooled cryostat [2]. With $60\,\mathrm{m\,s^{-1}}$ flow velocity of the hydrogen jet each pulse scatters from an unperturbed region of the sample. During hydrogen injection the chamber was at a pressure of $\sim 10^{-5}$ mbar. Scattering from the hydrogen jet is collected at 90 ° relative to the incident FEL radiation and in the vertical plane since the FEL radiation is horizontally polarized. We use a variable line space grating spectrograph [3] with a resolution of $\lambda/\Delta\lambda = 180$. A toroidal mirror 25.5 cm from the jet provides a collection solid angle of $1.9 \times 10^{-3}$ sr. Reference measurements of the FEL spectrum (Fig. 4.9) were performed using a second spectrograph, introduced into the FEL beam during tuning and setup, or a third spectrograph [146] which

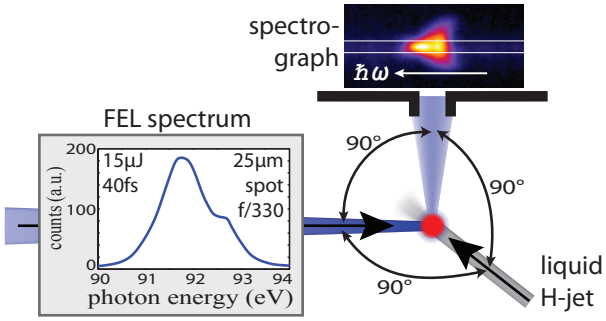


Figure 4.9: Experimental setup showing the liquid hydrogen jet in the focus of the FEL beam with typical time averaged spectrum, and the spectrograph at 90 ° scattering angle with the lineout region of the CCD, corresponding to the focussed part of the source image, marked by white bars.

simultaneously records radiation passing by the liquid jet target.

For these experiments we have chosen 91.8 eV soft x-ray radiation to be in a regime where the photon energy is well above the plasma frequency for liquid density hydrogen ($\hbar\omega_p = 7.6\,\mathrm{eV}$) and to match the large penetration depth of 9.4 $\mu$m [72] to the target radius (10 $\mu$m). While at this photon energy attenuation via photo-absorption has the highest cross section, a small fraction of the incident radiation is Thomson scattered. The ratio between these two cross sections is $3.8 \times 10^4$ at 91.8 eV [72]. Thus, the FEL pulses deposit energy in the liquid hydrogen while simultaneously probing the system. Due to the ultrashort pulse duration and the high penetration depth, the liquid hydrogen is heated isochorically and volumetrically by the pulse [1].

A scattering spectrum for 15 min integration time (4500 pulses) is shown in Fig. 4.10. It is composed of asymmetric peaks (plasmons) equally blue and red shifted from the incident photon energy by 0.65 eV. The measured spectrum is mainly broadened by the incident FEL bandwidth (1.1 eV full width at half maximum, mainly Gaussian, Fig. 4.9). Further source broadening effects (0.2 eV corresponding to the 20 $\mu$m source diameter) are minimal due to the geometry of the setup and the FEL pointing stability.

The total spectrum is described by the dynamic structure factor $S(\omega)$ [103, 110]:

$$S(\omega) = Z_f S_{ee}(\omega) + Z^2(1 - e^{-2W})S_{ii}(\omega). \tag{4.4}$$

Here, $Z$ is the nuclear charge and $Z_f$ the average number of free electrons per atom. The first term in Eq. (4.4) describes the high frequency free electron fluctuations which includes collective plasmon scattering. The second term describes the ionic, nearly elastic response with the ion-ion structure factor $S_{ii}$ modulated by the Debye-Waller factor $1-e^{-2W} \simeq 2W \propto T_i^2/T_D^2$ [106, 108],

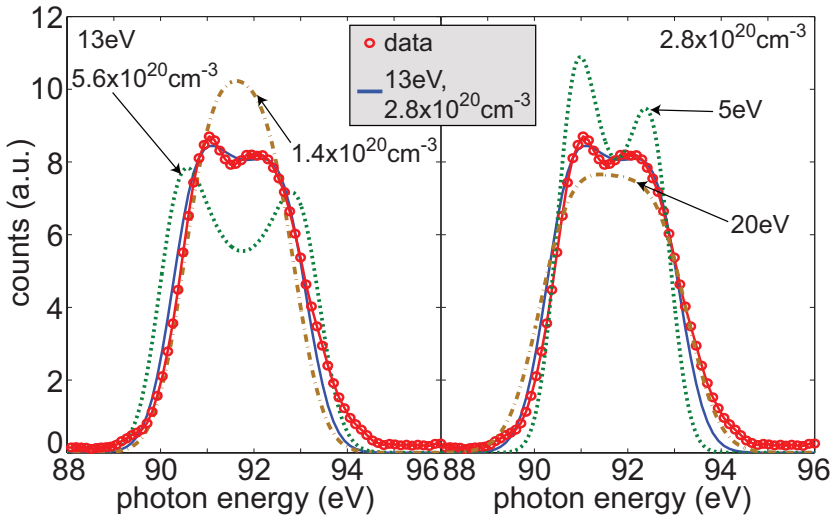


Figure 4.10: Experimental spectrum (red circles) and the best fit of a calculated spectrum with $n_e = 2.8 \times 10^{20}\,\mathrm{cm}^{-3}$ and $T_e = 13\,\mathrm{eV}$ (solid blue line). Comparison to fits with variation in density (left graph), $5.6 \times 10^{20}\,\mathrm{cm}^{-3}$ (dashed green) and $1.4 \times 10^{20}\,\mathrm{cm}^{-3}$ (dash-dotted brown), and in temperature (right graph), 20 eV (dash-dotted brown) and 5 eV (dashed green), are shown.

which accounts for low frequency ion acoustic fluctuations coupling with ionic thermal vibrations, where $T_i$ is the ion and $T_D$ the Debye temperature. In this experiment $T_i$ is sufficiently small against $T_D$ ($T_i \sim 2\,\mathrm{meV}$, and $T_D \sim 10\,\mathrm{meV}$ estimated using the Bohm-Staver relation [109]) so that elastic scattering is strongly suppressed. This effect was previously observed in laser based non-equilibrium experiments [107].

Collective TS spectra are calculated in Born-Mermin approximation [118] and convolved with the experimental resolution. A synthesized spectrum fits the measurement best using an electron temperature and density of 13 eV and $2.8 \times 10^{20}\,\mathrm{cm}^{-3}$, respectively (Fig. 4.10). Spectra obtained by varying these parameters by a factor of two deviate considerably from the observed spectra. Sensitivity analysis shows that the error in the fitting procedure is 25% and 7% in electron temperature and density, respectively. Furthermore, elastic scattering is practically absent in the experimental spectra and comparing with synthesized spectra we obtain an upper limit for $T_i < 0.1\,\mathrm{eV}$, where $S_{ii}$ has been estimated using the screened one component plasma model [112]. Consequently, the liquid hydrogen is excited to a non-equilibrium plasma state with different electron and ion temperatures at a very low degree of ionization ($\sim$0.7 %) but high atomic density ($4.2 \times 10^{22}\,\mathrm{cm}^{-3}$).

The degree of ionization remains low despite the high electron temperature, due to the short time scale of the interaction. The electron-atom, electron-ion, and electron-electron energy transfer time scales for 13 eV electrons are >13 ps, $\sim$16 ps, and $\sim$25 fs, respectively [58]. Impact ionization takes $0.4 - 1$ fs [12, 205], being the fastest process for electrons between 20 eV and 400 eV. This suggests that the electronic sub-system is thermalized within the duration of the FEL pulse (Fig. 4.11 (b)), but no equilibration has been reached between the other components explaining the combination of low degree of ionization and high electron temperature.

We have simulated the evolution of the electron kinetic energy distribution during and after the FEL irradiation (Fig. 4.11), using a model [18, 19, 206] based on kinetic equations. Due to the almost uniform target conditions (target radius matches penetration depth) [1] we can simulate a smaller target, a cluster of only $\sim 10^5$ hydrogen atoms. The simulation includes the following predominant interactions: photo- and collisional ionization, three-body recombination, elastic electron-ion and electron-atom scattering, and screened electron-electron interactions. Our model follows the full dynamics of an irradiated sample, from the non-equilibrium up to the thermal equilibrium phase for electrons. The electron temperature from the simulation $T_e' = 2/3\,\langle E_{\mathrm{kin}}^e \rangle$ is 12 eV, averaged over the FEL pulse duration, and the degree of ionization is 0.5 %, where $\langle E_{\mathrm{kin}}^e \rangle$ is the instantaneous ensemble average of the free electron kinetic energy. These results compare well

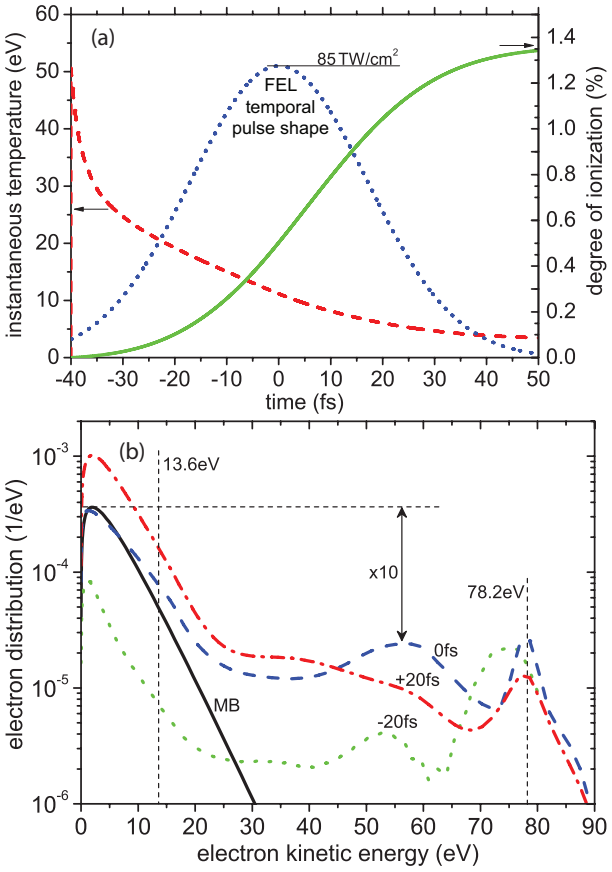


Figure 4.11: Cluster simulation (a) with the FEL temporal profile (dotted blue) and the evolution of the ionization degree (solid green) as well as the electron temperature $T_e'$ (dashed red) using the Lieberman and Lichtenberg impact ionization. The electron kinetic energy distribution (b) 20 fs before (dotted green), at (dashed blue), and 20 fs after (dash-dotted red) the FEL pulse peak. A Maxwell-Boltzmann distribution fit at 0 fs (solid black) and the photoelectron (78.2 eV) and ionization (13.6 eV) energies are shown for comparison.

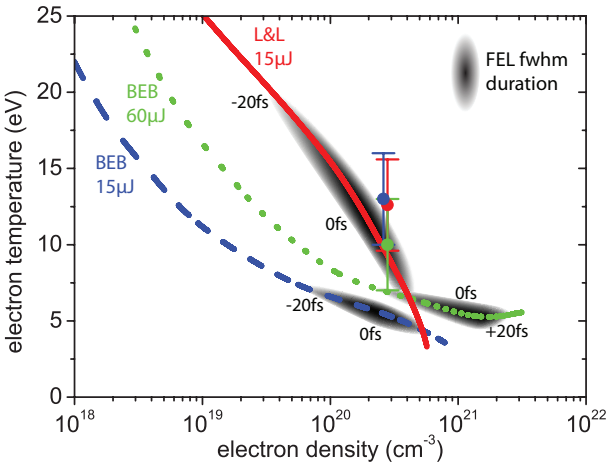


Figure 4.12: Measurements (colored circles) compared to the simulated evolution of the target's free electron density and temperature using different impact ionization cross sections and FEL pulse energies: Lieberman and Lichtenberg (solid red, 15 $\mu$J) and the BEB model (15 $\mu$J dashed blue, 60 $\mu$J dotted green). The FEL full width half maximum duration is indicated in gray scale.

to the TS measurement. Furthermore, the electron energy distribution approaches Maxwell-Boltzmann (MB) ∼20 fs before the peak of the FEL pulse (Fig. 4.11 (b)). This assures that detailed balance is indeed applicable to evaluate the experimental spectrum.

Simulating the target interaction we can study the influence of different cross sections for impact ionization in dense plasmas by comparing with our measurement. We used the National Institute of Standards and Technology (NIST) database for molecular hydrogen [205] as well as an expression from Lieberman and Lichtenberg [12]. The latter approximates the ionization via the low angle scattering of two free electrons and was employed in Fig. 4.11. NIST uses the binary encounter Bethe (BEB) model taking atomic and molecular structure into account. The models deviate up to a factor of four in the relevant electron energy range. Simulations with the classical model [12] yield an electron density and temperature at the FEL peak (0 fs) which matches our measurement significantly better than BEB (Fig. 4.12). Even assuming a four times higher FEL incident flux can not explain the observed values. A possible interpretation is that the atomic structure (as treated in BEB) does not play a significant role in the context of dense plasmas where, due to screening and correlation effects, high lying atomic states are removed and the electron interaction is more properly described with a classical ionic background.

In conclusion, we were able to obtain Thomson scattering spectra with an unprecedented signal to noise ratio due to the high repetition rate of

the FEL and compared to single laser pulse driven x-ray sources [50–52]. The ultrashort high intensity soft x-ray pulses allow us to heat liquid hydrogen isochorically and volumetrically to the observed moderately coupled non-equilibrium state. Our results compare well to non-equilibrium kinetic simulations using classical impact ionization models which show an electron relaxation time scale of $\sim$20 fs. Already available pump-probe techniques [207] will allow the measurement of time scales for the subsequent relaxation channels via electron-ion equilibration. This is a pioneering step towards the investigation of non-equilibrium and strongly coupled plasmas with implications from astro- to energy physics [21].

We thankfully acknowledge financial support by the Helmholtz Gemeinschaft via the Virtual Institute VH-VI-104, the German Federal Ministry for Education and Research via Project No. FSP 301-FLASH, and the Deutsche Forschungsgemeinschaft (DFG) via the Sonderforschungsbereich SFB 652. T.L. acknowledges DFG support under Grant No. LA 1431/2-1, R.R.F. under Grant No. GRK 1355. The work of S.H.G. and T.D. was performed under the auspices of the U.S. Department of Energy by Lawrence Livermore National Laboratory under Contract No. DE-AC52-07NA27344 and was supported by LDRDs 08-ERI-002, 08-LW-004. S.H.G. and C.F. were supported by the Alexander von Humboldt foundation, G.G. partially by the Engineering and Physical Sciences Research Council (Grant No. EP/G007187/1) and the Science and Technology Facilities Council of the UK. Finally, the authors are greatly indebted to the FLASH team for enabling an outstanding performance.

# Chapter 5

# Conclusion

In conclusion, pioneering warm dense matter (WDM) research was performed using the soft x-ray free electron laser (FEL) in Hamburg (FLASH). For this purpose, a versatile high throughput and high resolution spectrograph was constructed and integrated into various experimental setups [3] (chapter 3.4). Radiative hydrodynamic and Thomson Scattering (TS) simulations were conducted to prepare the experiments and analyze the gathered data [1, 5, 6] (chapters 4.2, 2.4 and 4.3). The conducted experiments measure the transmission [4] (chapter 4.1), emission [5] (chapter 4.2) and scattering [6] (chapter 4.3) of soft x-rays by WDM. In the course of these experiments a sound understanding of basic soft x-ray matter interaction relating to WDM was established.

In more detail, the interaction of the FLASH pulses with various targets was simulated permitting an interpretation of time integrated spectroscopy measurements and their time resolved composition [5] (chapter 4.2). The radiative hydrodynamics simulations also enabled us to estimate target inhomogeneities in free electron temperature and density after FLASH irradiation. From the resulting target profiles we could analyze the effect of the inhomogeneities on the TS spectrum. These more realistic scattering spectra are evidence that TS is a viable plasma diagnostic even for samples which are inhomogeneous to some extent, e.g. soft x-ray FEL irradiated hydrogen [1] (chapter 2.4).

Most insight into WDM and its interaction with soft x-rays was gained through experiments. In particular, the absorption of aluminium was measured intensity dependent. The observed saturable absorption was found to be a feasible method of generating larger quantities of homogenous WDM using soft x-ray FEL radiation [4] (chapter 4.1). Radiative recombination spectra were recorded with the newly built spectrograph. The spectra are an image of available and occupied states in the plasma approximately $40-60\,\mathrm{fs}$

after soft x-ray irradiation (chapter 2.1.3, page 17). Thus, they are a direct and ultrafast measurement of the free electron temperature [4] (chapter 4.1).

In addition, temporally integrated spectroscopic measurements of the plasma bremsstrahlung and line emission in conjunction with simulations enabled the distinct measurement of the plasma free electron temperature on different time scales. The temperature measured by bremsstrahlung emission was attributed to the first *ps* of radiative cooling (chapter 2.1.3, page 16). The temperature measured by line ratios in the radiative recombination occurs in the ps to ns hydrodynamic expansion phase (chapter 2.1.3, page 18). Therefore, even time integrated emission spectroscopy allowed us to distinctly probe various phases in the plasma evolution spanning several orders of magnitude [5] (chapter 4.2).

Furthermore, the method of self-TS was developed, where the sample is heated and probed within a single light pulse. This enabled the measurement of free electron temperature and density on the sub 40 fs timescale. By comparing the experimental results with simulations based on Boltzmann equations it was possible to distinguish different models for electron impact ionization, which is one of the main equilibration mechanisms for x-ray irradiated matter. The data strongly supports an impact ionization model based on classic electron-electron collisions [6] (chapter 4.3). Generally, TS spectra with unprecedented signal to noise ratio were recorded which allow high precision measurements of the plasma parameters and their comparison with models.

Altogether, this work constitutes a leap forward in WDM research. It utilizes for the first time soft x-ray FEL radiation to investigate WDM. The results yield a comprehensive picture of ultrafast soft x-ray matter interaction on the fs and particle to ns and macroscopic scale. The relevant relaxation mechanisms and particle interactions studied form the macroscopic behavior described by the equation of state. Thus, the findings are of relevance for various fields ranging from astrophysics over laser-matter interaction and inertial confinement fusion to industry applications.

# Chapter 6

# Outlook

The experiments in this work are among the first to utilize ultrashort and high brilliance soft x-ray FEL radiation to investigate WDM. They constitute a first step for this type of research and consequently concentrate on the exclusive use of FEL radiation and ultrafast timescales. A logical step for the subsequent investigation is to extend to a larger time domain via pump-probe experiments, while building on the knowledge acquired here. First techniques necessary for setups using optical pump and FEL probe radiation were already developed in this work (chapter 3.6, page 76). Furthermore, upgrades to the FLASH facility which are in progress at this time will deliver five to ten times more FEL pulse energy ($\sim$500 $\mu$J) to the experiments. This is sufficient to split the FEL pulse itself into a pump and probe portion using an already available split and delay device [207].

In particular, the experiments on saturable absorption [4] (chapter 4.1) and TS [6] (chapter 4.3) can profit from the additional time information. Through the conducted transmission measurement it is not clear for how long the aluminium target stays transparent for soft x-rays, i.e. how long the life time of the L-shell hole is. This time is determined mainly by the Auger recombination rate which might not be reliably predicted by theory for the WDM environment. The lifetime is also of interest because it limits the time window in which radiative recombination can occur, and through which the sample temperature is measured spectroscopically. An extension of the current setup to an FEL pump, FEL probe experiment will be capable of measuring the time dependent sample transmission to answer these open questions.

Thomson Scattering pump probe experiments will extend the measurement of free electron temperature and density from the ultrafast fs timescale, that was probed in this work, to the ps and ns timescale where electron-ion equilibration and plasma expansion occur (chapter 2.1). As the ions are

heated by the electrons over ps the elastic scattering signal will increase and enable a spectral measurement of the ion temperature via the Debye-Waller factor (chapter 2.3.2). Thus, the pump-probe technique can measure the electron ion equilibration time in a WDM sample. This was not possible before as the optical high power lasers that can be used to indirectly drive TS have ns pulse durations [22]. A topic of current investigation is if fs optical pump lasers will be capable to generate WDM sufficiently homogenous for TS experiments. Should this not be the case, FEL pump and FEL probe setups will have to be used. Furthermore, the accuracy of the TS measurement can be increased by deconvolving the scattered spectra with incident spectrum. Up to now, this was not possible as the reference spectrograph had insufficient resolution (chapter 3.5). After the 2009/2010 shutdown of FLASH, an online spectrograph integrated into the FEL beamline will be able to provide reference spectra with higher resolution for each FEL pulse. Then, the deconvolution of the scattering spectra can increase accuracy of the TS measurement.

Another topic of investigation are impact ionization models in WDM. In particular, why the self-TS measurements [6] (chapter 4.3) are better described by a model based on classic electron-electron collisions than by the binary encounter Bethe (BEB) model [205]. The BEB model takes the atomic structure into account and is in good agreement with previous experiments that use electron guns and low free electron densities in a dilute sample [64, 208]. However, in dense plasmas small angle Coulomb collisions predominate and are the basis of the classical description, which is possibly the reason why it matches our dense plasma data better. Other mechanisms that could influence the interaction include continuum lowering, collisions, and the laser electric field. Yet, these effects are small for the experimental conditions of this work and further investigation is necessary.

In greater perspective, the FEL sources have opened new possibilities for WDM research, which has only just begun to utilize these light sources. They enable unparalleled accuracy in the determination of plasma parameters and, thus, allow for vital comparisons to statistical models of correlated multi-particle systems. The new accuracy is possible due to the high brilliance of the FEL, it's comparatively high repetition rate and the ability to accumulate over many events. These attributes also describe present and future x-ray FELs such as the LCLS, the European XFEL and SPring-8. Therefore, much of the knowledge acquired through this work will be easily transferable to the new radiation sources. They will, for example, allow the generation of larger quantities of homogenous WDM from heavier elements. TS with these light sources will even be able to resolve ion acoustic modes to directly determine the ion temperature [54].

# Appendix A

# Interactive Content

This document is optimized for on screen viewing using Adobe Reader 9. All references within the document are hyperlinks. Use the alt + left arrow keys to return to the hyperlink origin. Where available, the bibliography entries also contain external hyperlinks to the publications. You can also use the bookmarks to navigate between the sections.

The figures A.1 and A.2 show the computer aided designs of the Thomson scattering experimental chamber (section 3.1) and the HiTRaX spectrograph (section 3.4), respectively. In the electronic version of this document, viewed using Adobe Reader 9, these drawings can be manipulated interactively. Left click the drawing with the mouse to activate interactivity. Predefined views and sections can be selected from the model tree. The following table shows the most useful manipulations:

| | |
|---|---|
| left mouse drag | rotate object |
| ctrl/alt + left drag | shift object |
| right mouse drag | zoom |
| mouse wheel | zoom |
| ctrl/alt + right drag | zoom to selection |

Furthermore, videos of the hydrogen jet (figure A.3) and the electron kinetic energy distribution in the hydrogen during FEL irradiation (figure A.4) can be played and paused by clicking on them. If you encounter problems playing the videos try upgrading to the latest Adobe Reader or installing the Cinepak codec.

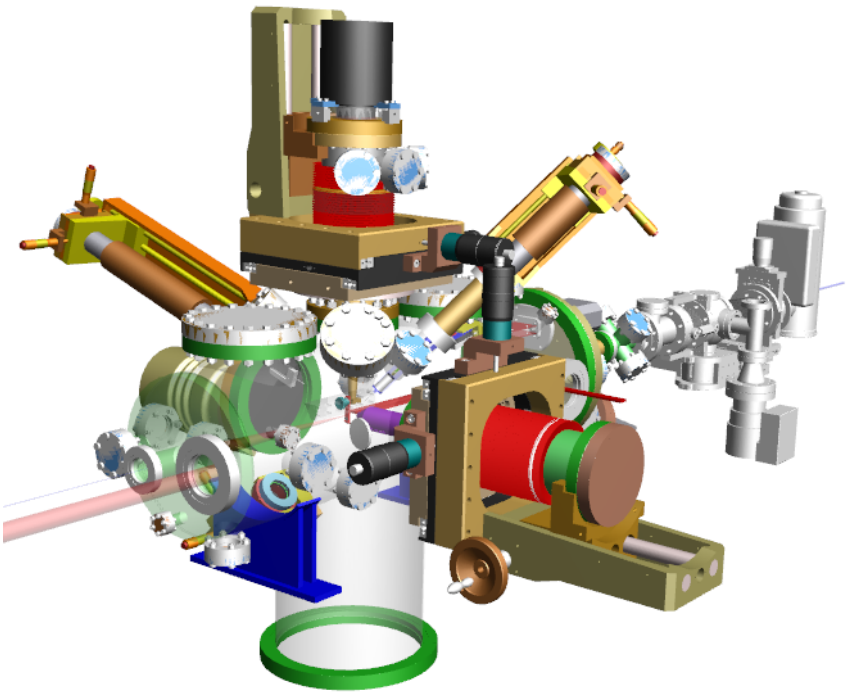

Figure A.1: Interactive CAD drawing of the experimental chamber used for Thomson scattering and bulk solid target irradiation. See also chapter 3.1. Cycle through different views by clicking here.

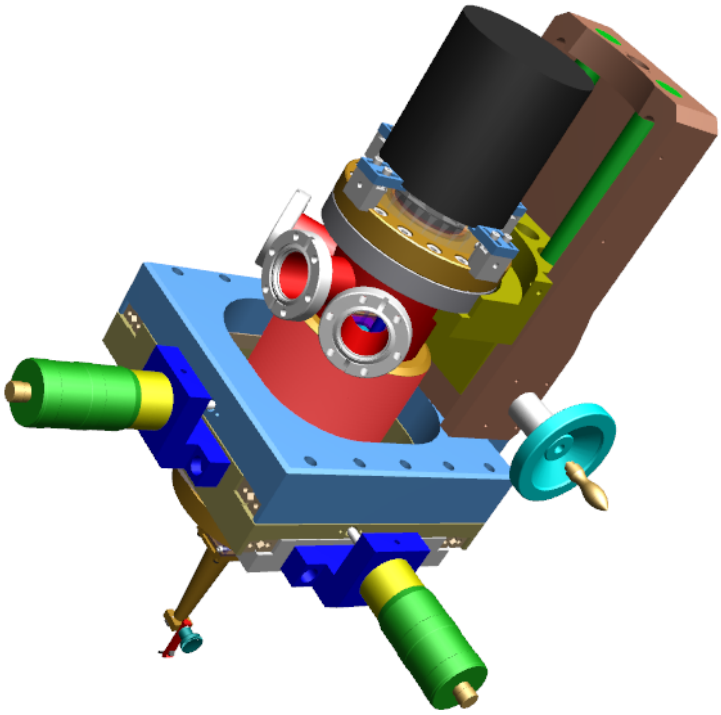

Figure A.2: Interactive CAD drawing of the HiTRaX spectrograph. See chapter 3.4 for a detailed description. Cycle through different views by clicking here.

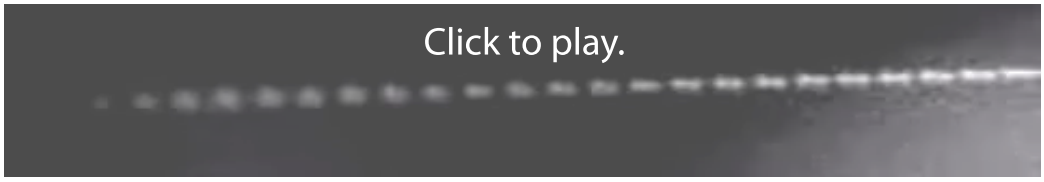


Figure A.3: The increasing amplitude of the piezo actuator oscillation induces a controlled Rayleigh breakup of the hydrogen jet into droplets. The video is stroboscopically illuminated to observe the fast (∼60 m/s) droplets. Droplets bouncing off the vacuum chamber walls can be seen as streaks since they are much slower than the kHz illumination. See also section 3.3

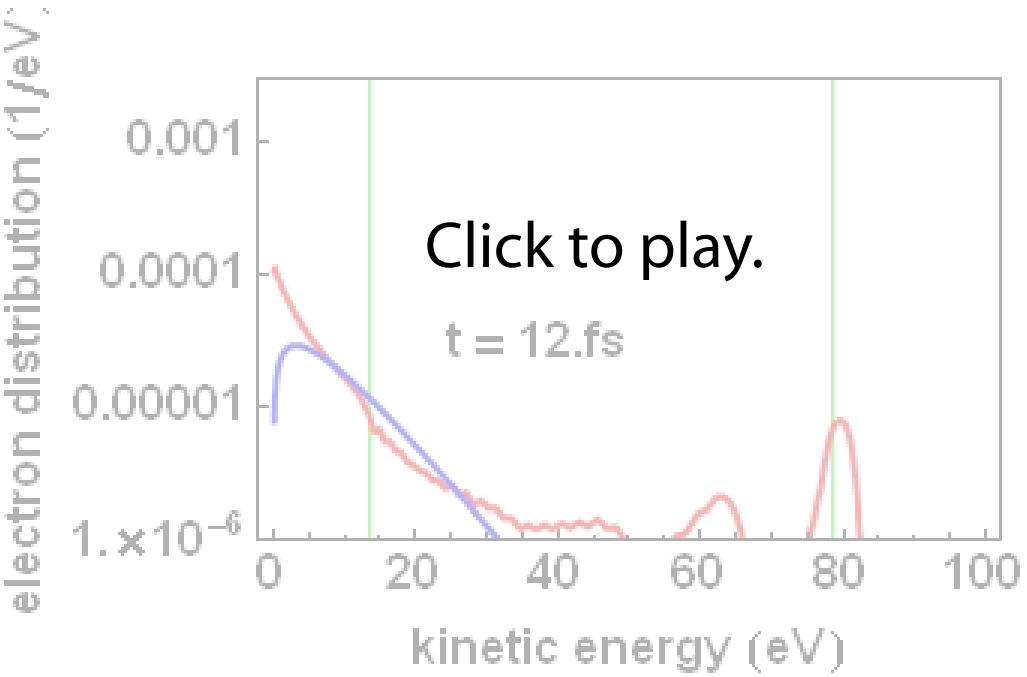


Figure A.4: The electron kinetic energy distribution (red) assumes a Maxwell-Boltzmann distribution with the same average electron energy (blue) before the FEL pulse peaks. The simulation uses a Boltzmann solver [18, 19] to obtain the electron kinetic energy distribution during FEL irradiation of a hydrogen cluster with $10^5$ atoms. The FEL pulse has a Gaussian pulse shape with a full width half max duration of 40 fs, peaking at 40 fs simulation time, and an intensity of 85 TW cm$^{-2}$ (15 $\mu$J on target) at 13.5 nm. The BEB impact ionization cross sections are used here. See also chapters 2.1, 4.3, and figure 4.11.

# Comment on my Contribution

This thesis represents the majority of warm dense matter related research during the last three years at the free electron laser in Hamburg (FLASH). The experiments were performed within large international collaborations. I took the offered opportunity to play a central role in the joint efforts and actively participated in all experimental work at FLASH itself, but also in preparative measurements at the University of Jena. Also, I designed a spectrograph which formed the main diagnostics in most of the presented experiments. I collaborated strongly with the University of Rostock and Oxford on Thomson scattering theory and concentrated in particular on the analysis of the related experiments.

I have contributed essentially to the papers included here, in the experimental work, analysis, interpretation and writing. This is also reflected by the rank of my name in the respective author lists.

# Acknowledgements

This thesis would not be possible without the help of many people. I am grateful to all and would like to thank some in particular.

Starting with the roots, I am blessed with loving parents, Uta and Rainer, die mich immer und bedingungslos ermutigen und unterstützen. I am also grateful for the necessary distractions by my girlfriend Catalina and by my friends, many of whom I found among my colleagues, which made for nice shifts, office pastimes, happy after hours and awesome holidays.

Being part of the great Thomson scattering and Microfocussing teams, I profited from a large combined know how. I also benefited from the BMBF, the graduate fellowship 1355, and the DESY infrastructure. The design and implementation of HiTRaX was only possible due to the collaboration with Ulf, Ingo, Hartmut Lärz and the Uni Jena and DESY machine shops. The enormous frustration tolerance of Josef, Sebastian, Andreas, Tim, and Sven allowed us to use the hydrogen jet which made the Thomson scattering experiment possible. I am thankful for discussions with Carsten, Robert, Beata, Ronald, Siegfried and Gianluca. They taught me Thomson scattering, warm dense matter, to interpret the data, and publishing.

Thanks to Professor Wurth for discussions opening new scientific perspectives and encouraging words. I am very glad to work with the master of experiments and equipment, Sven Toleikis. Without his profound know-how and calm approach none of the experiments would have been possible. Sven always kept his door open for a chat - scientific or otherwise. He showed me Hamburg beyond the gates of DESY and we spent some fun holidays. Last but surely not least, I am greatly indebted to Thomas Tschentscher. Despite his busy schedule, Thomas always had time for discussions, to correct my writing, to give me scientific advice, and to encourage me. He pointed me in the right directions and to the people I needed, while giving me plenty of freedom in the pursuit of our goals.

The last three years I joined some remarkable individuals on an interesting scientific quest and I'm looking forward to seeing people evolve and nature respond to our asking.

# Roland Rainer F ä u s t l i n

## Personal Information

| | |
|---|---|
| Name | Roland Rainer **F ä u s t l i n** |
| Birthday | July $15^{th}$ 1980 |
| Birthplace | Augsburg, Germany |
| Citizenship | German |

## Experience

| | |
|---|---|
| since Nov. 2006 | Employee at DESY (German Electron Synchrotron), working at FLASH (Free Electron Laser Hamburg) |
| since Nov. 2006 | Member of the Peak-Brightness Collaboration at FLASH (Hamburg) |
| Nov. 2006 - Dec. 2007 | Member of the Helmholtz Association Virtual Institute 104: "Plasma Physics Research Using Free Electron Lasers" |
| Jun. 2006 - Aug. 2006 | Research Assistant at The University of Texas at Austin, Texas Center for High Intensity Laser Science |
| Aug. 2001 - Jun. 2002 | Civil Service at boarding school in Augsburg, Germany |

## Education

| | |
|---|---|
| since Nov. 2006 | PhD student at University of Hamburg |
| Aug. 2005 - Aug. 2006 | Master in Physics on "Tailoring Blast Waves Pertaining to Supernova Remnants", Supervisor: Prof. T. Ditmire University of Texas at Austin, USA |
| Sept. 2004 | Physics Vordiplom |
| Oct. 2002 - Jul. 2005 | Physics, minors: Chemistry, Computer Science at Julius-Maximilians-University Würzburg, Germany |
| June 2001 | Abitur at J.v.Liebig Gymnasium, Augsburg, Germany |

## Awards

| | |
|---|---|
| since Nov. 2006 | German Research Foundation (DFG) graduate fellowship 1355: "Physics with new advanced coherent radiation sources" |
| since March 2008 | Member of the e-fellows network (www.e-fellows.net) |
| February 2008 | Poster award of the High Energy Density Physics Workshop (Hirschegg, Austria) |
| Aug. 2005 - Jun. 2006 | DAAD (German Academic Exchange Service) full scholarship |
| May 2006 | C. Paul Boner Graduate Fellowship in physics |
| June 2001 | DPG (German physical society) award for outstanding performance in the subject physics |

## Languages

| | |
|---|---|
| German | mother tongue |
| English | fluent |
| Spanish | fluent |
| French | basic |

See also the list of publications related to this thesis on page ix.

# Bibliography


[1] C. Fortmann, R. Thiele, R. R. Fäustlin et al., *Thomson scattering in dense plasmas with density and temperature gradients*, High Energy Density Physics **5**(3), p. 208-211 (2009), internet link.

[2] S. Toleikis, R. R. Fäustlin, L. Cao et al., *Soft x-ray scattering using fel radiation for probing near-solid density plasmas at few electron volt temperatures*, High Energy Density Physics **6**(1), p. 15-20 (2010), internet link.

[3] R. Fäustlin, U. Zastrau, S. Toleikis et al., *A compact soft x-ray spectrograph combining high efficiency and resolution*, Journal of Instrumentation **5**(02), p. P02004 (2010), internet link.

[4] B. Nagler, U. Zastrau, R. R. Fäustlin et al., *Turning solid aluminium transparent by intense soft x-ray photoionization*, Nature Physics **5**(9), p. 693-696 (2009), internet link.

[5] U. Zastrau, C. Fortmann, R. R. Fäustlin et al., *Bremsstrahlung and line spectroscopy of warm dense aluminum plasma heated by xuv free-electron-laser radiation*, Physical Review E **78**(6), p. 066406 (2008), internet link.

[6] R. Fäustlin, T. Bornath, T. Döppner et al., *Observation of ultrafast non-equilibrium collective dynamics in warm dense hydrogen plasma*, Physical Review Letters, accepted (2010).

[7] R. Redmer, *Physical properties of dense, low-temperature plasmas*, Physics Reports **282**(2-3), p. 35-157 (1997), internet link.

[8] R. Thiele, PhD thesis: *Thomsonstreuung in warmer und dichter materie*, Uni Rostock, 2007.

[9] N. Carron, *An introduction to the passage of energetic particles through matter*, Taylor and Franci Group, New York - London, 2007, internet link.

[10] Y.-K. Kim and M. E. Rudd, *Binary-encounter-dipole model for electron-impact ionization*, Physical Review A **50**, p. 3954 (1994), internet link.

[11] B. M. Smirnov, *Ionization processes in low-energy atomic-collisions*, Uspekhi Fizicheskikh Nauk **133**(4), p. 569-616 (1981), internet link.

[12] M. Lieberman and A. Lichtenberg, *Principles of plasma discharges and materials processing*, John Wiley & Sons, Hoboken, New Jersey, 1994, internet link.

[13] A. Höll, T. Bornath, L. Cao et al., *Thomson scattering from near-solid density plasmas using soft x-ray free electron lasers*, High Energy Density Physics **3**(1-2), p. 120-130 (2007), internet link.

[14] T. Scopigno, G. Ruocco and F. Sette, *Microscopic dynamics in liquid metals: The experimental point of view*, Reviews of Modern Physics **77**(3), p. 881-933 (2005), internet link.

[15] W. Ackermann, G. Asova, V. Ayvazyan et al., *Operation of a free-electron laser from the extreme ultraviolet to the water window*, Nature Photonics **1**(6), p. 336-342 (2007), internet link.

[16] *LCLS parameter database*, , `http://www-ssrl.slac.stanford.edu/htbin/rdbweb/LCLS_params_DB_public/`.

[17] J. Pirenne and P. Longe, *Contribution of the double electron transitions to the soft x-ray emission bands of metals*, Physica **30**(2), p. 277-292 (1964), internet link.

[18] B. Ziaja, T. Laarmann, H. Wabnitz et al., *Emission of electrons from rare gas clusters after irradiation with intense vuv pulses of wavelength 100 nm and 32 nm*, New Journal of Physics **11**(10), p. 103012 (2009), internet link.

[19] B. Ziaja, H. Wabnitz, F. Wang et al., *Energetics, ionization, and expansion dynamics of atomic clusters irradiated with short intense vacuum-ultraviolet pulses*, Physical Review Letters **102**(20), p. 205002 (2009), internet link.

[20] R. W. Lee, H. A. Baldis, R. C. Cauble et al., *Plasma-based studies with intense x-ray and particle beam sources*, 14th International Heavy Ion Inertial Fusion Symposium **20**, p. 527-536 (2002), internet link.

[21] *National research council: Frontiers in high energy density physics: The x-games of contemporary science*, National Academies Press, 2003, internet link.

[22] S. H. Glenzer and R. Redmer, *X-ray thomson scattering in high energy density plasmas*, Review of Modern Physics **81**(4), p. 1625-1663 (2009), internet link.

[23] D. Saumon, G. Chabrier, D. J. Wagner et al., *Modeling pressure-ionization of hydrogen in the context of astrophysics*, High Pressure Research **16**(5-6), p. 331-343 (2000), internet link.

[24] G. Magni and I. Mazzitelli, *Thermodynamic properties and equations of state for hydrogen and helium in stellar conditions*, Astronomy & Astrophysics **72**, p. 134-147 (1979), internet link.

[25] T. Guillot, *Interiors of giant planets inside and outside the solar system*, Science **286**(5437), p. 72-77 (1999), internet link.

[26] L. Vocadlo, D. Alfe, M. J. Gillan et al., *Possible thermal and chemical stabilization of body-centred-cubic iron in the earth's core*, Nature **424**(6948), p. 536-539 (2003), internet link.

[27] N. Nettelmann, B. Holst, A. Kietzmann et al., *Ab initio equation of state data for hydrogen, helium, and water and the internal structure of jupiter*, The Astrophysical Journal **683**(2), p. 1217 (2008), internet link.

[28] R. Launhardt and T. Henning, *Vom Dunkel zum Licht. Sternentstehung*, Physik in unserer Zeit **40**(1), p. 12-18 (2009), internet link.

[29] M. Morales, J. L. Ocaña, C. Molpeceres et al., *Model based optimization criteria for the generation of deep compressive residual stress fields in high elastic limit metallic alloys by ns-laser shock processing*, Surface and Coatings Technology **202**(11), p. 2257-2262 (2008), internet link.

[30] F. Ghadhfan, A. Al-Rajhi and M. D. Wagoner, *Laser in situ keratomileusis versus surface ablation: Visual outcomes and complications*, Journal of Cataract and Refractive Surgery **33**(12), p. 2041-2048 (2007), internet link.

[31] J. Lindl, *Development of the indirect-drive approach to inertial confinement fusion and the target physics basis for ignition and gain*, Physics of Plasmas **2**(11), p. 3933-4024 (1995), internet link.

[32] T. R. Dittrich, S. W. Haan, M. M. Marinak et al., *Review of indirect-drive ignition design options for the national ignition facility*, 40th Annual Meeting of the Division of Plasma Physics of the American-Physical-Society **6**, p. 2164-2170 (1998), internet link.

[33] J. D. Lindl, P. Amendt, R. L. Berger et al., *The physics basis for ignition using indirect-drive targets on the national ignition facility*, Physics of Plasmas **11**(2), p. 339-491 (2004), internet link.

[34] E. Garcia Saiz, G. Gregori, D. O. Gericke et al., *Probing warm dense lithium by inelastic x-ray scattering*, Nature Physics **4**(12), p. 940-944 (2008), internet link.

[35] N. A. Tahir, C. Deutsch, V. E. Fortov et al., *Proposal for the study of thermophysical properties of high-energy-density matter using current and future heavy-ion accelerator facilities at gsi darmstadt*, Physical Review Letters **95**, p. 035001 (2005), internet link.

[36] D. Hoffmann, A. Blazevic, P. Ni et al., *Present and future perspectives for high energy density physics with intense heavy ion and laser beams*, Laser and Particle Beams **23**(01), p. 47-53 (2005), internet link.

[37] A. R. Piriz, N. A. Tahir, J. J. López Cela et al., *Analytical models for the design of the laplas experiment*, Contributions to Plasma Physics **47**(4-5), p. 213-222 (2007), internet link.

[38] S. Sakabe, R. Sigel, G. D. Tsakiris et al., *X-ray generation in a cavity heated by 1.3um or 0.44um laser-light. 1. time-integrated measurements*, Physical Review A **38**(11), p. 5756-5768 (1988), internet link.

[39] L. B. Dasilva, T. W. Barbee, R. Cauble et al., *Electron-density measurements of high-density plasmas using soft-x-ray laser interferometry*, Physical Review Letters **74**(20), p. 3991-3994 (1995), internet link.

[40] L. B. DaSilva, P. Celliers, G. W. Collins et al., *Absolute equation of state measurements on shocked liquid deuterium up to 200 gpa (2 mbar)*, Physical Review Letters **78**(3), p. 483-486 (1997), internet link.

[41] A. Saemann, K. Eidmann, I. E. Golovkin et al., *Isochoric heating of solid aluminum by ultrashort laser pulses focused on a tamped target*, Physical Review Letters **82**(24), p. 4843-4846 (1999), internet link.

[42] G. W. Collins, P. M. Celliers, L. B. Da Silva et al., *Temperature measurements of shock compressed liquid deuterium up to 230 gpa*, Physical Review Letters **87**(16), p. 165504 (2001), internet link.

[43] J. J. MacFarlane, J. E. Bailey, G. A. Chandler et al., *X-ray absorption spectroscopy measurements of thin foil heating by z-pinch radiation*, Physical Review E **66**(4) (2002), internet link.

[44] P. K. Patel, A. J. Mackinnon, M. H. Key et al., *Isochoric heating of solid-density matter with an ultrafast proton beam*, Physical Review Letters **91**, p. 125004 (2003), internet link.

[45] K. Widmann, T. Ao, M. E. Foord et al., *Single-state measurement of electrical conductivity of warm dense gold*, Physical Review Letters **92**(12) (2004), internet link.

[46] Y. Ping, D. Hanson, I. Koslow et al., *Broadband dielectric function of nonequilibrium warm dense gold*, Physical Review Letters **96**(25), p. 255003 (2006), internet link.

[47] T. Ao, Y. Ping, K. Widmann et al., *Optical properties in nonequilibrium phase transitions*, Physical Review Letters **96**(5) (2006), internet link.

[48] D. E. Evans and J. Katzenstein, *Laser light scattering in laboratory plasmas*, Reports on Progress in Physics **32**(1), p. 207 (1969), internet link.

[49] D. Riley, N. C. Woolsey, D. McSherry et al., *X-ray diffraction from a dense plasma*, Physical Review Letters **84**, p. 1704 (2000), internet link.

[50] S. H. Glenzer, G. Gregori, R. W. Lee et al., *Demonstration of spectrally resolved x-ray scattering in dense plasmas*, Physical Review Letters **90**(17), p. 175002 (2003), internet link.

[51] S. H. Glenzer, O. L. Landen, P. Neumayer et al., *Observations of plasmons in warm dense matter*, Physical Review Letters **98**(6), p. 065002 (2007), internet link.

[52] A. L. Kritcher, P. Neumayer, J. Castor et al., *Ultrafast x-ray thomson scattering of shock-compressed matter*, Science **322**(5898), p. 69-71 (2008), internet link.

[53] T. Tschentscher and S. Toleikis, *Investigations of ultrafast phenomena in high-energy density physics using x-ray fel radiation*, European Physical Journal D **36**(2), p. 193-197 (2005), internet link.

[54] G. Gregori and D. O. Gericke, *Low frequency structural dynamics of warm dense matter*, Physics of Plasmas **16**(5), p. 056306 (2009), internet link.

[55] R. P. Drake, *High-energy-density physics*, Springer-Verlag Berlin Heidelberg, 2006, internet link.

[56] C. Fortmann, T. Bornath, R. Redmer et al., *X-ray thomson scattering cross-section in strongly correlated plasmas*, Laser and Particle Beams **27**(02), p. 311-319 (2009), internet link.

[57] W. L. Kruer, *The physics of laser plasma interactions*, Addison-Wesley Publishing Company, Inc., 1988, internet link.

[58] J. Huba, *NRL plasma formulary*, Naval Research Laboratory, Washington, DC 20375, 2009, internet link.

[59] J. H. Hubbell, H. A. Gimm and I. Overbo, *Pair, triplet, and total atomic cross sections (and mass attenuation coefficients) for 1 mev-100 gev photons in elements z=1 to 100*, Journal of Physical and Chemical Reference Data **9**(4), p. 1023-1148 (1980), internet link.

[60] A. C. Thompson, D. T. Attwood, E. M. Gullikson et al., *X-ray data booklet*, Berkeley, California 94720, 2001, internet link.

[61] S. Eliezer and K. Mima, *Applications of laser-plasma interactions*, CRC Press, Taylor & Francis Group, Boca Raton, Florida, 2009, internet link.

[62] P. Gibbon and E. Forster, *Short-pulse laser - plasma interactions*, Plasma Physics and Controlled Fusion **38**(6), p. 769 (1996), internet link.

[63] J. J. Thomson, *Xlii. ionization by moving electrified particles*, Philosophical Magazine Series 6 **23**(136), p. 449 - 457 (1912), internet link.

[64] *National institute of standards and technology*, November 2009, `http://www.nist.gov/index.html`.

[65] M. B. Shah, D. S. Elliott and H. B. Gilbody, *Pulsed crossed-beam study of the ionisation of atomic hydrogen by electron impact*, Journal of Physics B **20**(14), p. 3501 (1987), internet link.

[66] C. O. Almbladh, A. L. Morales and G. Grossmann, *Theory of auger core-valence-valence processes in simple metals. i. total yields and core-level lifetime widths*, Physical Review B **39**, p. 3489 (1989), internet link.

[67] N. Medvedev and B. Rethfeld, *BMBF FLASH project meeting, Rostock: Transient dynamic of electrons in metal irradiated with an ultrashort laser pulse*, (2009).

[68] Y. Hahn, *Electron - ion recombination processes - an overview*, Reports on Progress in Physics **60**(7), p. 691 (1997), internet link.

[69] H. K. Chung, M. H. Chen, W. L. Morgan et al., *Flychk: Generalized population kinetics and spectral model for rapid spectroscopic analysis for all elements*, High Energy Density Physics **1**(1), p. 3-12 (2005), internet link.

[70] H. A. Kramers, *Xciii. on the theory of x-ray absorption and of the continuous x-ray spectrum*, Philosophical Magazine Series 6 **46**(275), p. 836 - 871 (1923), internet link.

[71] S. Vinko, *Peak brightness collaboration meeting: Electronic structure of aluminium and gold excited by high-intensity xuv fel radiation* (2010).

[72] B. L. Henke, E. M. Gullikson and J. C. Davis, *X-ray interactions: photoabsorption, scattering, transmission, and reflection at E = 50-30,000 eV, Z = 1-92*, Atomic Data and Nuclear Data Tables **54**(2), p. 181-342 (1993), internet link.

[73] N. W. Ashcroft and D. N. Mermin, *Festkörperphysik*, Oldenbourg Wissenschaftsverlag GmbH, München, 2007, internet link.

[74] W. Lochte-Holtgreven, *Plasma diagnostics*, AIP, New York, 1995.

[75] P. A. Loboda and A. Y. Faenov, *SpectrW3*, January 2010, `http://spectr-w3.snz.ru/index.phtml`.

[76] D. Lide, *CRC handbook of chemistry and physics*, CRC Press LLC, Boca Raton, Florida, 2007, internet link.

[77] C. Gutt, S. Streit-Nierobisch, L.-M. Stadler et al., *Single pulse resonant magnetic scattering using a soft x-ray free-electron laser*, Physical Review B, accepted (2009).

[78] J. J. MacFarlane, I. E. Golovkin and P. R. Woodruff, *Helios-cr - a 1-d radiation-magnetohydrodynamics code with inline atomic kinetics modeling*, Journal of Quantitative Spectroscopy and Radiative Transfer **99**(1-3), p. 381-397 (2006), internet link.

[79] E. Gullikson, *X-ray interactions with matter*, November 2009, http://henke.lbl.gov/optical_constants/.

[80] S. Lyon and J. Johnson, technical report *Sesame: The los alamos national laboratory equation of state. database technical report, la-ur-92-3407.*, 1992.

[81] L. Spitzer and R. Härm, *Transport phenomena in a completely ionized gas*, Physical Review **89**, p. 977 (1953), internet link.

[82] D. Gray and J. Kilkenny, *The measurement of ion acoustic turbulence and reduced thermal conductivity caused by a large temperature gradient in a laser heated plasma*, Plasma Physics **22**(2), p. 81 (1980), internet link.

[83] A. Hauer, W. C. Mead, O. Willi et al., *Measurement and analysis of near-classical thermal transport in one-micron laser-irradiated spherical plasmas*, Physical Review Letters **53**, p. 2563 (1984), internet link.

[84] Y. Zel'dovich and Y. Raizer, *Physics of shock waves and high-temperature hydrodynamic phenomena*, Dover Publications, Inc., Mineola, N.Y., 2002, internet link.

[85] A. Pukhov and J. Vehn, *Laser hole boring into overdense plasma and relativistic electron currents for fast ignition of icf targets*, Physical Review Letters **79**, p. 2686 (1997), internet link.

[86] M. H. Key, M. D. Cable, T. E. Cowan et al., *Hot electron production and heating by hot electrons in fast ignitor research*, The 39th annual meeting of division of plasma physics of APS **5**(5), p. 1966-1972 (1998), internet link.

[87] H. E. Huxley, A. R. Faruqi, J. Bordas et al., *Use of synchrotron radiation in time-resolved x-ray-diffraction studies of myosin layer line reflections during muscle-contraction*, Nature **284**(5752), p. 140-143 (1980), internet link.

[88] J. A. Pitney, I. K. Robinson, I. A. Vartaniants et al., *Streaked speckle in Cu3Au coherent x-ray diffraction*, Physical Review B **62**, p. 13084 (2000), internet link.

[89] L. Peyser-Capadona, J. Zheng, J. I. González et al., *Nanoparticle-free single molecule anti-stokes raman spectroscopy*, Physical Review Letters **94**, p. 058301 (2005), internet link.

[90] H. N. Chapman, A. Barty, M. J. Bogan et al., *Femtosecond diffractive imaging with a soft-x-ray free-electron laser*, Nature Physics **2**(12), p. 839-843 (2006), internet link.

[91] K. J. Gaffney and H. N. Chapman, *Imaging atomic structure and dynamics with ultrafast x-ray scattering*, Science **316**(5830), p. 1444-1448 (2007), internet link.

[92] *Nobel Foundation, J.J. Thomson - Biography*, November 2009, http://nobelprize.org/nobel_prizes/physics/laureates/1906/thomson-bio.html.

[93] K. L. Bowles, *Radio wave scattering in the ionosphere*, Advances in Electronics and Electron Physics **19**, p. 55-176 (1964), internet link.

[94] E. Fünfer, B. Kronast and H. J. Kunze, *Experimental results on light scattering by a [theta]-pinch plasma using a ruby laser*, Physics Letters **5**(2), p. 125-127 (1963), internet link.

[95] H. J. Kunze, E. Fünfer, B. Kronast et al., *Measurement of the spectral distribution of light scattered by a [theta]-pinch plasma*, Physics Letters **11**(1), p. 42-43 (1964), internet link.

[96] E. Nardi, Z. Zinamon, D. Riley et al., *X-ray scattering as a dense plasma diagnostic*, Physical Review E **57**(4), p. 4693-4697 (1998), internet link.

[97] E. E. Salpeter, *Electron density fluctuations in a plasma*, Physical Review **120**(5), p. 1528-1535 (1960), internet link.

[98] D. Bohm and E. P. Gross, *Theory of plasma oscillations. a. origin of medium-like behavior*, Physical Review **75**, p. 1851 (1949), internet link.

[99] D. Bohm and E. P. Gross, *Theory of plasma oscillations. b. excitation and damping of oscillations*, Physical Review **75**, p. 1864 (1949), internet link.

[100] R. J. Goldston and P. H. Rutherford, *Introduction to plasma physics*, Taylor & Francis Group, New York, NY, 1995, internet link.

[101] R. Kubo, *Fluctuation-dissipation theorem*, Reports on Progress in Physics **29**, p. 255 (1966), internet link.

[102] J. Chihara, *Difference in x-ray scattering between metallic and non-metallic liquids due to conduction electrons*, Journal of Physics F: Metal Physics **17**(2), p. 295-304 (1987), internet link.

[103] J. Chihara, *Interaction of photons with plasmas and liquid metals-photoabsorption and scattering*, Journal of Physics-Condensed Matter **12**(3), p. 231-247 (2000), internet link.

[104] R. Thiele, *personal communication*, Rostock, 2009.

[105] W. Demtröder, *Experimentalphysik 3*, Springer-Verlag Berlin Heidelberg New York, 2004, internet link.

[106] G. Gregori, S. H. Glenzer and O. L. Landen, *Generalized x-ray scattering cross section from nonequilibrium plasmas*, Physical Review E **74**(2), p. 026402 (2006), internet link.

[107] A. Ravasio, G. Gregori, A. Benuzzi-Mounaix et al., *Direct observation of strong ion coupling in laser-driven shock-compressed targets*, Physical Review Letters **99**(13) (2007), internet link.

[108] B. E. Warren, *X-ray diffraction*, Courier Dover Publications, Mineola, New York, 1990, internet link.

[109] D. Bohm and T. Staver, *Application of collective treatment of electron and ion vibrations to theories of conductivity and superconductivity*, Physical Review **84**(4), p. 836-837 (1951), internet link.

[110] G. Gregori, S. H. Glenzer, W. Rozmus et al., *Theoretical model of x-ray scattering as a dense matter probe*, Physical Review E **67**(2) (2003), internet link.

[111] G. Gregori, S. H. Glenzer, H. K. Chung et al., *Measurement of carbon ionization balance in high-temperature plasma mixtures by temporally resolved x-ray scattering*, Journal of Quantitative Spectroscopy and Radiative Transfer **99**(1-3), p. 225-237 (2005), internet link.

[112] G. Gregori, A. Ravasio, A. Höll et al., *Derivation of the static structure factor in strongly coupled non-equilibrium plasmas for x-ray scattering studies*, High Energy Density Physics **3**(1-2), p. 99-108 (2007), internet link.

[113] T. Hughes, *Plasma and laser light*, John Wiley & Sons, N.Y., 1975.

[114] J. Sheffield, *Plasma scattering of electromagnetic radiation*, Academic Press, N.Y., 1975.

[115] G. Bekefi, *Radiation processes in plasmas*, John Wiley, New York, 1994.

[116] V. Schwarz, B. Holst, T. Bornath et al., *Static ion structure factor for dense plasmas: Semi-classical and ab initio calculations*, High Energy Density Physics, in press, uncorrected proof , internet link.

[117] A. Höll, R. Redmer, G. Röpke et al., *X-ray thomson scattering in warm dense matter*, European Physical Journal D **29**(2), p. 159-162 (2004), internet link.

[118] R. Redmer, H. Reinholz, G. Röpke et al., *Theory of x-ray thomson scattering in dense plasmas*, IEEE Transactions on Plasma Science **33**(1), p. 77-84 (2005), internet link.

[119] T. Scopigno, U. Balucani, G. Ruocco et al., *Density fluctuations in molten lithium: inelastic x-ray scattering study*, Journal of Physics: Condensed Matter **12**(37), p. 8009 (2000), internet link.

[120] S. H. Glenzer, W. Rozmus, B. J. MacGowan et al., *Thomson scattering from high- z laser-produced plasmas*, Physical Review Letters **82**, p. 97 (1999), internet link.

[121] R. W. Lee, H. A. Baldis, R. C. Cauble et al., *Plasma-based studies with intense x-ray and particle beam sources*, Laser and Particle Beams **20**(03), p. 527-536 (2002), internet link.

[122] R. W. Lee, S. J. Moon, H.-K. Chung et al., *Finite temperature dense matter studies on next-generation light sources*, Journal of the Optical Society of America B **20**(4), p. 770-778 (2003), internet link.

[123] S. H. Glenzer, P. Neumayer, T. Doppner et al., *Compton scattering measurements from dense plasmas*, Journal of Physics: Conference Series **112**(3), p. 032071 (2008), internet link.

[124] H. J. Lee, P. Neumayer, J. Castor et al., *X-ray thomson-scattering measurements of density and temperature in shock-compressed beryllium*, Physical Review Letters **102**, p. 115001 (2009), internet link.

[125] H. A. Baldis, J. Dunn, M. E. Foord et al., *Thomson scattering diagnostic of solid density plasmas using x-ray lasers*, Review of Scientific Instruments **73**(12), p. 4223-4228 (2002), internet link.

[126] S. Sahoo, G. F. Gribakin, G. Shabbir Naz et al., *Compton scatter profiles for warm dense matter*, Physical Review E **77**, p. 046402 (2008), internet link.

[127] R. Thiele, R. Redmer, H. Reinholz et al., *Using the gould-dewitt scheme to approximate the dynamic collision frequency in a dense electron gas*, Journal of Physics A: Mathematical and General **39**(17), p. 4365 (2006), internet link.

[128] B. Holst, R. Redmer and M. P. Desjarlais, *Thermophysical properties of warm dense hydrogen using quantum molecular dynamics simulations*, Physical Review B **77**, p. 184201 (2008), internet link.

[129] L. Cao, I. Uschmann, F. Zamponi et al., *Space-time characterization of laser plasma interactions in the warm dense matter regime*, Laser and Particle Beams **25**(02), p. 239-244 (2007), internet link.

[130] A. Barty, S. Boutet, M. J. Bogan et al., *Ultrafast single-shot diffraction imaging of nanoscale dynamics*, Nature Photonics **2**(7), p. 415-419 (2008), internet link.

[131] H. Wabnitz, L. Bittner, A. R. B. Castro et al., *Multiple ionization of atom clusters by intense soft x-rays from a free-electron laser*, Nature **420**(6915), p. 482-485 (2002), internet link.

[132] C. Bostedt, H. Thomas, M. Hoener et al., *Multistep ionization of argon clusters in intense femtosecond extreme ultraviolet pulses*, Physical Review Letters **100**(13), p. 133401 (2008), internet link.

[133] S. W. Epp, J. R. C. Lopez-Urrutia, G. Brenner et al., *Soft x-ray laser spectroscopy on trapped highly charged ions at FLASH*, Physical Review Letters **98**(18), p. 183001 (2007), internet link.

[134] R. Moshammer, Y. H. Jiang, L. Foucar et al., *Few-photon multiple ionization of ne and ar by strong free-electron-laser pulses*, Physical Review Letters **98**(20), p. 203001 (2007), internet link.

[135] A. Rudenko, L. Foucar, M. Kurka et al., *Recoil-ion momentum distributions for two-photon double ionization of He and Ne by 44 eV free-electron laser radiation*, Physical Review Letters **101**(7), p. 073003 (2008), internet link.

[136] E. Saldin, E. Schneidmiller and M. Yurkov, *The physics of free electron lasers*, Springer-Verlag Berlin Heidelberg New York, 1999.

[137] G. Materlik and T. Tschentscher, *Tesla technical design report part v: The x-ray free electron laser*, 2001, internet link.

[138] S. Khan, *Free-electron lasers*, Journal of Modern Optics **55**(21), p. 3469 - 3512 (2008), internet link.

[139] A. Singer, I. A. Vartanyants, M. Kuhlmann et al., *Transverse-coherence properties of the free-electron-laser FLASH at DESY*, Physical Review Letters **101**(25), p. 254801 (2008), internet link.

[140] K. Tiedtke, A. Azima, N. Bargen et al., *The soft x-ray free-electron laser FLASH at DESY: beamlines, diagnostics and end-stations*, New Journal of Physics **11**, p. 023029 (2009), internet link.

[141] K. Tiedtke, J. Feldhaus, U. Hahn et al., *Gas detectors for x-ray lasers*, Journal of Applied Physics **103**(9), p. 094511 (2008), internet link.

[142] M. Fajardo, P. Zeitoun and J.-C. Gauthier, *Hydrodynamic simulation of xuv laser-produced plasmas*, The European Physical Journal D **29**(1), p. 69-76 (2004), internet link.

[143] J. J. Angulo Gareta and D. Riley, *Prospects for the diagnosis of electron-ion temperature equilibration rates of warm dense matter by ultra-short pulse hard x-ray diffraction with an x-ray free electron laser*, High Energy Density Physics **2**(3-4), p. 83-89 (2006), internet link.

[144] O. L. Landen, S. H. Glenzer, M. J. Edwards et al., *Dense matter characterization by x-ray thomson scattering*, Journal of Quantitative Spectroscopy and Radiative Transfer **71**(2-6), p. 465-478 (2001), internet link.

[145] V. Ayvazyan, N. Baboi, J. Bähr et al., *First operation of a free-electron laser generating gw power radiation at 32 nm wavelength*, The European Physical Journal D **37**(2), p. 297-303 (2006), internet link.

[146] P. Beiersdorfer, J. R. C. Lopez-Urrutia, P. Springer et al., *Spectroscopy in the extreme ultraviolet on an electron beam ion trap*, Review of Scientific Instruments **70**(1), p. 276-279 (1999), internet link.

[147] J. Jasny, U. Teubner, W. Theobald et al., *A single-shot spectrograph for the soft x-ray region*, Review of Scientific Instruments **65**(5), p. 1631-1635 (1994), internet link.

[148] A. Prystawik, T. Laarmann, J. Tiggesbäumker et al., in preparation (2010).

[149] E. Lemmon, M. McLinden and D. Friend, *Thermophysical properties of fluid systems*, March 2009, http://webbook.nist.gov.

[150] H. Redlin, A. Azima, N. Stojanovic et al., *The FLASH pump-probe laser system*, Review of Scientific Instruments, submitted (2009).

[151] P. Radcliffe, S. Düsterer, A. Azima et al., *An experiment for two-color photoionization using high intensity extreme-uv free electron and near-ir laser pulses*, Nuclear Instruments and Methods in Physics Research Section A: Accelerators, Spectrometers, Detectors and Associated Equipment **583**(2-3), p. 516-525 (2007), internet link.

[152] A. Azima, S. Dusterer, P. Radcliffe et al., *Time-resolved pump-probe experiments beyond the jitter limitations at FLASH*, Applied Physics Letters **94**(14) (2009), internet link.

[153] S. Toleikis, R. Fäustlin, T. Tschentscher et al., in preparation (2010).

[154] A. Przystawik, PhD thesis: *Dynamik von metallclustern in suprafluidem helium*, Uni Rostock, 2010.

[155] S. Toleikis, T. Döppner, R. R. Fäustlin et al., *Soft x-ray thomson scattering at flash*, Journal of Physics B: Atomic and Molecular Physics, in preparation (2010).

[156] J. Nordgren, G. Bray, S. Cramm et al., *Soft x-ray emission spectroscopy using monochromatized synchrotron radiation (invited)*, **60**, p. 1690-1696 (1989), internet link.

[157] T. Ito and S. Okazaki, *Pushing the limits of lithography*, Nature **406**(6799), p. 1027-1031 (2000), internet link.

[158] R. Giacconi, W. P. Reidy, G. S. Vaiana et al., *Grazing-incidence telescopes for x-ray astronomy*, Space Science Reviews **9**(1), p. 3-57 (1969), internet link.

[159] A. C. Brinkman, C. J. T. Gunsing, J. S. Kaastra et al., *First light measurements of capella with the low-energy transmission grating spectrometer aboard the chandra x-ray observatory*, The Astrophysical Journal Letters **530**(2), p. L111 (2000), internet link.

[160] T. Kita, T. Harada, N. Nakano et al., *Mechanically ruled aberration-corrected concave gratings for a flat-field grazing-incidence spectrograph*, Applied Optics **22**(4), p. 512-513 (1983), internet link.

[161] N. Nakano, H. Kuroda, T. Kita et al., *Development of a flat-field grazing-incidence xuv spectrometer and its application in picosecond xuv spectroscopy*, Applied Optics **23**(14), p. 2386-2392 (1984), internet link.

[162] A. d. Castro and R. Reininger, *Optimization of undulators for a sx-700 instrument: Finite element coupled to ray tracing*, **63**, p. 1317-1320 (1992), internet link.

[163] C. U. S. Larsson, A. Beutler, O. Björneholm et al., *First results from the high resolution xuv undulator beamline bw3 at hasylab*, Nuclear Instruments and Methods in Physics Research Section A: Accelerators, Spectrometers, Detectors and Associated Equipment **337**(2-3), p. 603-608 (1994), internet link.

[164] R. Reininger and V. Saile, *A soft x-ray grating monochromator for undulator radiation*, Nuclear Instruments and Methods in Physics Research Section A: Accelerators, Spectrometers, Detectors and Associated Equipment **288**(2-3), p. 343-348 (1990), internet link.

[165] J. Nordgren and R. Nyholm, *Design of a portable large spectral range grazing incidence instrument*, Nuclear Instruments and Methods in Physics Research Section A: Accelerators, Spectrometers, Detectors and Associated Equipment **246**(1-3), p. 242-245 (1986), internet link.

[166] S. Shin, A. Agui, M. Fujisawa et al., *Soft x-ray emission spectrometer for undulator radiation*, **66**, p. 1584-1586 (1995), internet link.

[167] H. W. Schnopper, L. P. Van Speybroeck, J. P. Delvaille et al., *Diffraction grating transmission efficiencies for xuv and soft x rays*, Applied Optics **16**(4), p. 1088-1091 (1977), internet link.

[168] S. Sailaja, V. Arora, S. R. Kumbhare et al., *A simple xuv transmission grating spectrograph with sub-angström resolution for laser-plasma interaction studies*, Measurement Science and Technology **9**(9), p. 1462 (1998), internet link.

[169] M. Meyer, D. Cubaynes, P. O'Keeffe et al., *Two-color photoionization in xuv free-electron and visible laser fields*, Physical Review A **74**(1) (2006), internet link.

[170] G. N. Lewis, D. Lipkin and T. T. Magel, *Reversible photochemical processes in rigid media. a study of the phosphorescent state*, Journal of the American Chemical Society **63**(11), p. 3005-3018 (1941), internet link.

[171] *National task force on high energy density physics: Frontiers for discovery in high energy density physics*, Office of Science and Technology Policy, National Science and Technology Council, Interagency Working Group on the Physics of the Universe, 2004, internet link.

[172] Committee on the Physics of the Universe, Board on Physics and Astronomy, Division on Engineering and Physical Sciences, *Connecting quarks with the cosmos: Eleven science questions for the new century*, National Academies Press, 2003, internet link.

[173] A. A. Sorokin, S. V. Bobashev, T. Feigl et al., *Photoelectric effect at ultrahigh intensities*, Physical Review Letters **99**(21), p. 213002 (2007), internet link.

[174] G. M. Dyer, A. C. Bernstein, B. I. Cho et al., *Equation-of-state measurement of dense plasmas heated with fast protons*, Physical Review Letters **101**(1), p. 015002 (2008), internet link.

[175] *Hiper project: Warm dense matter*, 2009, `http://www.hiper-laser.org/science/extrememateriallsscience/warmdensematter.asp`.

[176] J. Chalupský, L. Juha, J. Kuba et al., *Characteristics of focused soft x-ray free-electron laser beam determined by ablation of organic molecular solids*, Optics Express **15**(10), p. 6036-6043 (2007), internet link.

[177] S. M. Vinko, G. Gregori, M. P. Desjarlais et al., *Free-free opacity in warm dense aluminum*, High Energy Density Physics **5**(3), p. 124-131 (2009), internet link.

[178] G. Dufour, J.-M. Mariot, P.-E. Nilsson-Jatko et al., *K-LL Auger spectrum of aluminium*, Physica Scripta **13**(6), p. 370 (1976), internet link.

[179] P. H. Hannah and P. Weightman, *The spectrum of Al KL2,3-L22,3V satellite Auger transitions*, Journal of Physics C: Solid State Physics **18**(9), p. L239 (1985), internet link.

[180] D.-K. Kim and I. Kim, *Calculation of ionization balance and electrical conductivity in nonideal aluminum plasma*, Physical Review E **68**, p. 056410 (2003), internet link.

[181] K. Wefers, *Properties and characterization of surface oxides on aluminum alloys*, Aluminum **57**, p. 722-726 (1981).

[182] M. P. Seah and W. A. Dench, *Quantitative electron spectroscopy of surfaces: A standard data base for electron inelastic mean free paths in solids*, Surface and Interface Analysis **1**(1), p. 2-11 (1979), internet link.

[183] J. C. Ashley, C. J. Tung and R. H. Ritchie, *Electron inelastic mean free paths and energy losses in solids: I. aluminum metal*, Surface Science **81**(2), p. 409-426 (1979), internet link.

[184] D. J. Fabian, L. M. Watson and C. A. W. Marshall, *Soft x ray spectroscopy and the electronic structure of solids*, Reports on Progress in Physics **34**(2), p. 601 (1971), internet link.

[185] B. J. Siwick, J. R. Dwyer, R. E. Jordan et al., *An atomic-level view of melting using femtosecond electron diffraction*, Science **302**(5649), p. 1382-1385 (2003), internet link.

[186] R. Ernstorfer, M. Harb, C. T. Hebeisen et al., *The formation of warm dense matter: Experimental evidence for electronic bond hardening in gold*, Science **323**(5917), p. 1033-1037 (2009), internet link.

[187] T. R. Dittrich, S. W. Haan, M. M. Marinak et al., *Review of indirect-drive ignition design options for the national ignition facility*, Physics of Plasmas **6**, p. 2164-2170 (1999), internet link.

[188] T. S. Perry, P. T. Springer, D. F. Fields et al., *Absorption experiments on x-ray-heated mid-z constrained samples*, Physical Review E **54**(5), p. 5617-5631 (1996), internet link.

[189] V. Ayvazyan, N. Baboi, I. Bohnet et al., *Generation of gw radiation pulses from a vuv free-electron laser operating in the femtosecond regime*, Physical Review Letters **88**(10) (2002), internet link.

[190] V. Kaufman and W. C. Martin, *Wavelengths and energy-level classifications for the spectra of aluminum (al-i through al-xiii)*, Journal of Physical and Chemical Reference Data **20**(5), p. 775-858 (1991), internet link.

[191] K. Oguri, Y. Okano, T. Nishikawa et al., *Transient observation of extended x-ray absorption fine structure in laser-melted si by using femtosecond laser-produced-plasma soft x ray*, Applied Physics Letters **87**(1) (2005), internet link.

[192] J. A. Bearden, *X-ray wavelengths*, Reviews of Modern Physics **39**(1), p. 78 (1967), internet link.

[193] H. R. Griem, *Principles of plasma spectroscopy*, Cambridge University Press, 1997.

[194] J. A. Gaunt, *Continuous absorption*, Proceedings of the Royal Society of London. Series A, Containing Papers of a Mathematical and Physical Character **126**(803), p. 654-660 (1930), internet link.

[195] C. Fortmann, R. Redmer, H. Reinholz et al., *Bremsstrahlung vs. thomson scattering in vuv-fel plasma experiments*, High Energy Density Physics **2**(3-4), p. 57-69 (2006), internet link.

[196] S. Kuhlbrodt, B. Holst and R. Redmer, *Comptra04 - a program package to calculate composition and transport coefficients in dense plasmas*, Contributions to Plasma Physics **45**(2), p. 73-88 (2005), internet link.

[197] U. Teubner, G. Kuhnle and F. P. Schafer, *Soft-x-ray spectra produced by subpicosecond laser-double-pulses*, Applied Physics Letters **59**(21), p. 2672-2674 (1991), internet link.

[198] K. J. Lagattuta, *Multiphoton ionization rates for atomic-hydrogen - linear and circular-polarization compared*, Physical Review A **43**(9), p. 5157-5160 (1991), internet link.

[199] A. L. Dobryakov, V. M. Farztdinov, Y. E. Lozovik et al., *Laser-induced nonequilibrium electron distribution in metals on a femtosecond time scale*, Physica Scripta **60**(6), p. 572-578 (1999), internet link.

[200] R. Lavilla and H. Mendlowitz, *Optical constants of aluminum in vacuum ultraviolet*, Physical Review Letters **9**(4), p. 149 (1962), internet link.

[201] M. M. Murnane, H. C. Kapteyn, M. D. Rosen et al., *Ultrafast x-ray pulses from laser-produced plasmas*, Science **251**(4993), p. 531-536 (1991), internet link.

[202] A. Krenz and J. Vehn, *Vuv-heating of plasma layers and their use as ultrafast switches*, European Physical Journal D **36**(2), p. 199-202 (2005), internet link.

[203] J. Filevich, J. J. Rocca, M. C. Marconi et al., *Picosecond-resolution soft-x-ray laser plasma interferometry*, Applied Optics **43**(19), p. 3938-3946 (2004), internet link.

[204] D. Pines and P. Nozières, *The theory of quantum liquids*, W.A. Benjamin, New York, 1966.

[205] W. Hwang, Y.-K. Kim and M. E. Rudd, *New model for electron-impact ionization cross sections of molecules*, The Journal of Chemical Physics **104**(8), p. 2956-2966 (1996), internet link.

[206] B. Ziaja, A. d. Castro, E. Weckert et al., *Modelling dynamics of samples exposed to free-electron-laser radiation with boltzmann equations*, European Physical Journal D **40**(3), p. 465-480 (2006), internet link.

[207] R. Mitzner, B. Siemer, M. Neeb et al., *Spatio-temporal coherence of free electron laser pulses in the soft x-ray regime*, Optics Express **16**(24), p. 19909-19919 (2008), internet link.

[208] E. Krishnakumar and S. K. Srivastava, *Electron correlation effects in the dissociative ionization of H2*, Journal of Physics B **27**(11), p. L251 (1994), internet link.

# Index

absorption
    inverse bremsstrahlung, 12
    photoionization, 10
Auger decay, 15

binary encounter Bethe model, 15
Bohm-Gross dispersion, 29
Bohm-Staver relation, 33
bremsstrahlung emission, 16

collision frequency, 14
Compton scattering, 10
Coulomb potential, 6
coupling parameter $\Gamma$, 6
critical density, 8
cross section
    Thomson, 30
cryostat, 62

Debye length, 7
Debye temperature, 33
Debye-Waller factor, 32
degeneracy parameter $\Theta$, 6
density fluctuation, 30
density of states, 18
detailed balance, 28
dielectric coefficient, 31
dispersion, *see* Bohm-Gross dispersion
Doppler broadening, 30
droplets, 63
dynamic form factor, *see* structure factor
dynamic structure factor, *see* structure factor

Fermi energy, 6
FLASH, 44
flux limiter, 23
frozen core approximation, 32

gas monitor detector (GMD), 44

heat transport, 22
HiTRaX, 65
hydrodynamic limit, 34
hydrogen jet, 62

impact ionization, 14
inverse bremsstrahlung, *see* absorption

kinetic regime, 35

Lagrangian hydrodynamics, 21
line emission, 18

over-dense plasma, 8

particle collisions, 14
peak brilliance, 44
photoionization, *see* absorption
plasma frequency, 8
plasmon, 31
power spectrum, 30

radiative recombination, 17

random phase approximation, *see* structure factor
Rayleigh instability, 63

scattering parameter, 27
screening lenght, *see* Debye length
shadowgraphy, 76
skin depth, 8
spatial jitter, 79
structure factor, 29
    basic electromagnetics, 29
    calculation, 34
    decomposition, 31
    random phase approximation, 34
    simulation, 34

temporal jitter, 77
temporal overlap, 76
thermal energy, 6
Thomson scattering, 26
three-body recombination, 16
time of flight (TOF), 79

under-dense plasma, 8

Wigner-Seitz-radius, 6